Univerzita Palackého v Olomouci
Přírodovědecká fakulta
Společná laboratoř optiky

DISERTAČNÍ PRÁCE

Vývoj detektoru času průletu vysokoenergetických částic

Vypracoval	**Tomáš Komárek**
Studijní program	Fyzika
Studijní obor	Aplikovaná fyzika
Forma studia	Prezenční
Vedoucí diplomové práce	Mgr. Libor Nožka, Ph.D.
Termín odevzdání práce	Prosinec 2023

Palacký University Olomouc
Faculty of Science
Joint Laboratory of Optics

DISSERTATION

Development of high energy particle time-of-flight detector

Author	**Tomáš Komárek**
Study programme	Physics
Field of study	Applied Physics
Study form	Full time
Supervisor	Mgr. Libor Nožka, Ph.D.
Submission date	December 2023

Bibliografická identifikace

Autor	Tomáš Komárek
Název práce	Vývoj detektoru času průletu vysokoenergetických částic
Typ práce	Disertační
Pracoviště	Společná laboratoř optiky
Vedoucí práce	Mgr. Libor Nožka, Ph.D.
Rok obhajoby práce	2023
Abstrakt	Tato disertační práce se věnuje vývoji systému AFP-ToF, což je rychlý časovací detektor patřící pod projekt ATLAS na urychlovači LHC. Úkolem tohoto systému je párování protonů zachycených dráhovými detektory AFP stanic k srážkám (vertexům) v ATLASu, ze kterých pochází. Bez této informace by data z AFP byla zatížena nadměrným pozadím kvůli značnému pile-upu při standardní luminozitě na LHC. Nejprve je tento ToF systém charakterizován ve své původní podobě. Poté jsou popsány četné úpravy a vylepšení, uvedena jejich motivace a je proveden rozbor jejich dopadu. Dále je vyhodnoceno časové rozlišení kompletního systému. Závěrem se práce věnuje procesu instalace a uvedení do provozu, po nichž je možné zahájit standardní provoz systému ToF na LHC.
Anotace	Cílem této disertace byl vývoj detektoru času letu pro projekt AFP a jeho nasazení v Run 3 urychlovače LHC. Disertace má osm kapitol. Nejprve uvede čtenáři systém AFP a Čerenkovovo záření, které je využíváno detektorem času letu. Dále je popsán a charakterizován původní detektor času letu, je popsán jeho vývoj a experimenty, které tento proces provázely. Následně je vyhodnocen jeho výkon. Závěrem je popsán proces instalace a uvedení do provozu na urychlovači LHC.
Klíčová slova	Částicová fyzika, dopředný detektor, detektor času letu, CERN, LHC, ATLAS, AFP
Počet stran	150
Počet příloh	2
Jazyk	Anglický

Bibliographical identification

Author	Tomáš Komárek
Title	Development of high energy particle time-of-flight detector
Type of thesis	Dissertation
Department	Joint Laboratory of Optics
Supervisor	Mgr. Libor Nožka, Ph.D.
The year of presentation	2023
Abstract	This dissertation covers the development of AFP-ToF, a fast timing detector system intended for use as a part of the ATLAS project at the LHC accelerator. The purpose of this system is to match the protons detected by the AFP silicon tracker detectors to the appropriate collision vertex in ATLAS. Without this, the AFP would be burdened with excessive background in data collected at the standard LHC luminosity with significant pile-up. The ToF system is first characterized in its original form, then the numerous modifications and upgrades are described, their motivation explained and their impact evaluated. The performance of the system as a whole is presented. Finally, the installation and commissioning phases are discussed, the last necessary steps before the updated ToF system can enter standard operation at the LHC.
Annotation	The goal of this dissertation was to develop the time-of-flight system for the AFP project for deployment in LHC Run 3. The dissertation has eight chapters. The text first introduces the reader to the AFP system and the Cherenkov radiation the time-of-flight part uses. Then the original time-of-flight design is described and characterized, followed by description of the development process and the experiments that guided it. The performance of the time-of-flight system is then evaluated. Finally, the process of installation and commissioning at the LHC accelerator is discussed.
Keywords	Particle physics, forward detector, Time-of-Flight detector, CERN, LHC, ATLAS, AFP
Number of pages	150
Number of appendices	2
Language	English

Prohlášení

Prohlašuji, že jsem předloženou disertační práci vypracoval samostatně pod vedením Mgr. Libora Nožky, Ph.D. a že jsem použil zdrojů, které cituji a uvádím v seznamu použitých pramenů.

V Olomouci dne 11. prosince 2023

. . . .

Tomáš Komárek

Poděkování

Chtěl bych tímto poděkovat všem lidem, kteří mě podporovali v průběhu mého dlouhého studia i následného vypracovávání této disertační práce. Především mým rodičům, mému bratrovi, kolegům z částicové skupiny na SLO UP Olomouc a mému trpělivému vedoucímu Mgr. Liboru Nožkovi, Ph.D.

Dále bych rád poděkoval za morální podporu také mým kolegům ze studentského spolku UP Crowd a svým četným přátelům, kteří mě dlouhodobě povzbuzovali či mi poskytli útočiště pro nerušené psaní této práce.

Contents

Preamble

The AFP-ToF (ATLAS Forward Proton – Time of Flight) is a particle detector subsystem focused on providing a precise particle arrival timing at the order of few tens of ps, corresponding to a travel of only a few millimetres of the highly relativistic particles near the speed of light at the LHC (Large Hadron Collider). This timing information is meant to complement the particle tracks reconstructed by the silicon tracker layers employed in the AFP forward detector. The motivation for this precise timing will be discussed later in this work.

This dissertation describes the development of the AFP-ToF detector system in the years $2016-2023$, where the dissertation author made an important contribution. The author's work first focused on characterization of the initial 2016 AFP-ToF version. Based on the findings, further work directly related towards further development of the system.

The author's contribution revolved mostly around the optical and signal processing parts of the detector. Major contributions were made in the areas of the Cherenkov optical bars development, PMT (photomultiplier) characterization and evaluation for the intended purpose and conditions (including direct communication with the manufacturer), PMT high voltage power supply scheme optimization, preamplifier testing and tuning, CFD (Constant Fraction Discriminator) characterization and calibration and also the evaluation of the time-to-digital converter contribution to the timing resolution. Significant contributions were made by the author towards preparation and testing of the high voltage line insulation for the low grade vacuum together with high voltage vacuum feed-through preparation and vacuum tightness tests of the entire system. A minor contribution was also made towards the trigger module testing once it was introduced to the signal processing chain.

These development-oriented tests and measurements are based mostly on two data sources. The first was the testing of the PMT and relevant electronics in an optics laboratory using laser systems with exceptionally short pulses (femtosecond Ti-Sapphire laser, later a picosecond diode laser). This allowed for a perfect control of the experimental conditions, especially the part of the active area of the PMT put to test, the amount of light (average number of photons) in the laser pulses and the repetition rate of the pulses. The second source of experimental data were beam tests, where the ToF system was subject to tests using a particle beam emulating the realistic use conditions at the LHC. The author participated at numerous such beam tests (total of 14) and worked on the experimental setup preparation, operation and tuning as well as the immediate on-site data analysis. Subsequent more detailed data analyses of the obtained data followed after each beam test.

Since March 2019, the author also took up the responsibility as a Beam Test Coordinator for the AFP project. This meant a leading role in the planning, organisation and execution of one of the most crucial activities in the development cycle of the

AFP-ToF system – the testing, tuning and integration phases using a real particle beam.

Finally, the preparation and execution of the installation efforts of the AFP-ToF system on the LHC at CERN in 2017 and 2021, where the author played an important role, are also discussed. This involved prior detailed testing of all parts of the signal chain, installation and precise mechanical alignment of the optical bars, execution of the installation and the subsequent testing of all the channels of the ToF system up to the CFD and trigger module output. A necessary followup was then the detector commissioning and tuning, eventually allowing inclusion in the ATLAS combined runs for data taking as designed.

List of publications relevant to the topic with author's participation

The author of this work participated on numerous papers directly related to AFP-ToF development. The author's master's thesis [1] was also already on this topic. Furthermore, the author has also fulfilled qualification criteria and has been included on the author list of the ATLAS Collaboration since August 2019. The ATLAS Collaboration publications are not included in this list as there are hundreds of them and they are mostly not relevant to the topic of this work. The full list of author's publications can be found at ORCID: `https://orcid.org/0000-0002-3047-3146`.
The author of this work participated on the following publications relevant to the topic:

- T. Komárek. Simulation of optical part of high-energy particle time-of-flight detector and comparison with data. Master's thesis, Palacký University in Olomouc, Faculty of Science, Olomouc, 2016.

- L. Nozka, L. Adamczyk, G. Avoni, A. Brandt, P. Buglewicz, E. Cavallaro, G. Chiodini, L. Chytka, K. Ciesla, P.M. Davis, M. Dyndal, S. Grinstein, P. Hamal, M. Hrabovsky, K. Janas, K. Jirakova, M. Kocian, T. Komarek, K. Korcyl, J. Lange, D. Mandat, V. Michalek, I. Lopez Paz, D. Northacker, M. Rijssenbeek, L. Seabra, P. Schovanek, R. Staszewski, P. Swierska, and T. Sykora. Construction of the optical part of a time-of-flight detector prototype for the AFP detector. *Opt. Express*, 24(24):27951–27960, Nov 2016.

- J. Lange, M. Carulla, E. Cavallaro, L. Chytka, P.M. Davis, D. Flores, F. Förster, S. Grinstein, S. Hidalgo, T. Komarek, G. Kramberger, I. Mandić, A. Merlos, L. Nozka, G. Pellegrini, D. Quirion, and T. Sykora. Gain and time resolution of 45 μm thin Low Gain Avalanche Detectors before and after irradiation up to a fluence of 1015 neq/cm2. *Journal of Instrumentation*, 12(05):P05003, May 2017.

- L. Chytka, G. Avoni, A. Brandt, E. Cavallaro, P. M. Davis, F. Förster, M. Hrabovsky, Y. Huang, K. Jirakova, M. Kocian, T. Komarek, K. Korcyl, J. Lange, V. Michalek, L. Nozka, I. Lopez Paz, M. Rijssenbeek, P. Schovanek, T. Sykora, and V. Urbasek. Timing resolution studies of the optical part of the AFP time-of-flight detector. *Opt. Express*, 26(7):8028–8039, Apr 2018.

- T. Komárek, L. Nožka, L. Chytka, and M. Hrabovský. Vývoj detektoru času letu relativistických částic pro projekt AFP. *Jemná mechanika a optika*, 63:167 – 170, 2018.

- Ladislav Chytka, Miroslav Hrabovský, Tomáš Komárek, Václav Michálek, Libor Nožka, Tomáš Sýkora, and Vladimír Urbášek. Time resolution of the SiPM-NUV3S. *Nuclear Instruments and Methods in Physics Research Section A: Accelerators, Spectrometers, Detectors and Associated Equipment*, 935:51–55, 2019.

- Yu. Melikyan, T. Sýkora, T. Komárek, L. Nožka, D. Serebryakov, and V. Urbášek. Load capacity and recovery behaviour of ALD-coated MCP-PMTs. *Nuclear Instruments and Methods in Physics Research Section A: Accelerators, Spectrometers, Detectors and Associated Equipment*, 949:162854, 2020.

- Libor Nozka, Andrew Brandt, Karel Cerny, Miroslav Hrabovsky, Tomas Komarek, Filip Krizek, Dusan Mandat, Marko Milovanovic, Michael Rijssenbeek, Petr Schovanek, Tomas Sykora, Vladimir Urbasek, and Jaromir Zatloukal. Performance studies of new optics for the time-of-flight detector of the AFP project. *Opt. Express*, 28(13):19783–19796, Jun 2020.

- T. Komárek, V. Urbášek, A. Brandt, V.A. Chirayath, L. Chytka, M. Hrabovský, L. Nožka, M. Rijssenbeek, and T. Sýkora. Timing resolution and rate capability of Photonis miniPlanacon XPM85212/A1-S MCP-PMT. *Nuclear Instruments and Methods in Physics Research Section A: Accelerators, Spectrometers, Detectors and Associated Equipment*, 985:164705, 2021.

- T. Komárek, V. Urbášek, A. Brandt, K. Černý, V.A. Chirayath, J. DeFazio, V. Georgiev, S. Hail, M. Hrabovský, Z. Kubík, L. Nožka, D. Orlov, S. Duarte Pinto, M. Rijssenbeek, T. Sýkora, F. Yang, and J. Zich. Characterization of the miniPlanacon XPM85112-S-R2D2 MCP-PMT with custom modified backend electronics. *Nuclear Instruments and Methods in Physics Research Section A: Accelerators, Spectrometers, Detectors and Associated Equipment*, 1041:167330, 2022.

- Libor Nozka, Giulio Avoni, Elzbieta Banas, Andrew Brandt, Karel Cerny, Paul M. Davis, Serge Duarte Pinto, Vjaceslav Georgiev, Miroslav Hrabovsky, Tomas Komarek, Krzysztof Korcyl, Ivan Lopez-Paz, Marko Milovanovic, Goran Mladenovic, Dmitry A. Orlov, Michael Rijssenbeek, Petr Schovanek, Tomas Sykora, Maciej Trzebinski, Vladimir Urbasek, and Jan Zich. Upgraded cherenkov time-of-flight detector for the AFP project. *Opt. Express*, 31(3):3998–4014, Jan 2023.

Chapter 1

Introduction

1.1 Proton-proton interactions at high energy particle accelerators

Proton – proton interactions at high energies can be categorized into multiple general scenarios:

- elastic – both protons survive intact with no further products, thus keeping their original energy as they simply deflect by a small angle (typically at the order of microradians) – for example the ALFA detector in the forward region of ATLAS on the LHC is specialized on this, using the optical theorem to measure the total cross section [2],
- single diffractive – only one of the protons survives while losing some energy in the interaction, the other becomes an excited system that will produce multiple hadrons,
- double diffractive – both protons become excited and eventually break up, but can still be recognized as separate objects,
- central diffractive – both protons survive, but their energy loss creates a central system – a special case of these is the exclusive production of particle pairs, such as pion pair production studied in [3],
- non-elastic non-diffractive – neither proton survives, both forming a common system that cannot be easily divided into distinct subsystems, unlike the diffractive interactions.

The scenarios described above can be visualized as in Figure 1.1, where the vertical axis represents the rapidity span between the colliding protons A and B and the red systems X are the excited systems destined for a breakup.

Traditionally, diffractive events were recognised by the presence of a "rapidity gap", meaning there was a gap with no collision products at high pseudorapidity η (closer along the beam direction). This gap signifies that the proton undergoing interaction survived without breaking up in the process, which would otherwise occupy the high rapidity region.

In high pileup situations at higher beam energies, the rapidity gap is very narrow and often occupied by the products of the pileup events. This is where forward detectors for tagging the surviving protons become very useful for diffraction events identification.

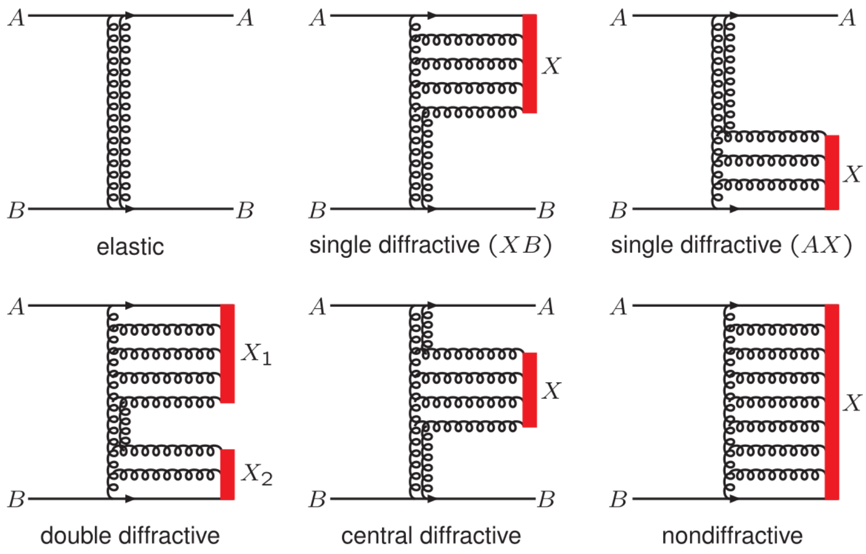

Figure 1.1: High energy proton – proton interaction types, depicted as Feynman-style schematic diagrams. The vertical axis is a rough representation of the rapidity gaps between individual objects taking part in the interaction. Image source: [4].

Additionally, with a favourable setup of the beamline magnets, these detectors can act as spectrometers, estimating the energy loss of the leading protons.

1.2 The ATLAS Forward Proton detector

The AFP (ATLAS Forward Proton) detector system is a part of the ATLAS (A Toroidal LHC Apparatus) experiment at the LHC (Large Hadron Collider) in CERN (European Organization for Nuclear Research), the particle physics laboratory located at the outskirts of Geneva across the border of Switzerland and France. The LHC is currently the largest and most powerful man-made particle accelerator in the world with its 27 km circumference and design 14 TeV center-of-mass collision energy of protons.

ATLAS surrounds IP1, one of the four active interaction points at the LHC. The AFP system is designed to detect diffractive events from IP1, where one or both leading protons survive the collision while losing some of their original energy, by tagging these protons. This sets the requirement on a location of the system far in the forward region. The tags can be a "single tag" or a "double tag", depending on whether surviving protons are caught in AFP stations on one or both outcoming sides. This corresponds to the single diffraction and central diffraction events as described in section 1.1. These tags are a much more reliable sign of diffraction as compared to the traditional rapidity gap approach, especially considering the high energies and pile-ups achieved at the LHC. Details about the AFP physics programme and the studied processes can be found in [5].

There are a total of 4 AFP stations, with a pair mounted on each of the downstream beamlines w.r.t. IP1, $\sim$ 210 m away in each direction. Scheme of the AFP stations placement is in Figure 1.2. The AFP stations closer to ATLAS and IP1 ale referred to as the "near" stations, while those further downstream as "far" stations.

Before reaching AFP, the colliding protons pass through numerous magnets controlling the proton beams. While quadrupoles shape the beams, acting as magnetic lenses,

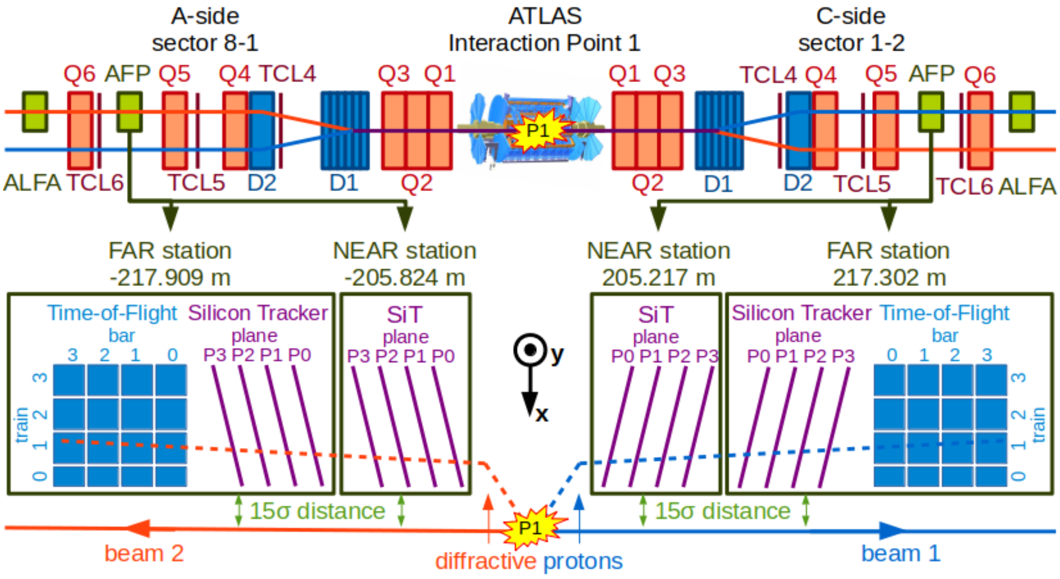

Figure 1.2: Location of the AFP stations at the LHC. The stations are mounted on the straight sections of the outgoing beampipes w.r.t. IP1 at around 210 m. The ToF system is present only in the far station (further downstream) on each side. Q1-Q6 are quadrupoles handling focusing and shaping of the beam, D1 and D2 are dipoles responsible for setting up the beam crossing and guiding the beams back to their beamlines. TCL are collimators, adjustable jaws scraping off particles far from the beam core that could otherwise endanger the LHC systems. In the centre, the ATLAS coordinate system is marked, z axis points in the direction of beam 2, towards A-side. A and C sides are the Anti-clockwise and Clockwise directions along the LHC.

dipoles bend their paths to cross and separate the two counter-circulating beams and keep them on the proper circular orbit around the LHC [6]. As the AFP is installed on the straight sections of the LHC that occupy few hundred meters around the interaction point before the arc begins, only a few dipoles handling the beam crossing and separation are relevant. Crucially for AFP, these dipoles help separate the protons of interest from the beam as their energy loss means they have a lower relativistic mass [7] compared to those of the beam and are thus influenced more by the magnetic field. Still, AFP stations need to get very close to the LHC beam, only a few millimetres apart, to achieve a good acceptance of the events of interest. This close proximity to the beam imposes severe radiation hardness requirements on the entire system, especially on the components that interact with the diffractive protons. At the same time, a safe distance from the beam needs to be kept to avoid disrupting the beam, damaging the detector or generating excessive showers that may damage the equipment downstream or overwhelm other detectors with background events.

The AFP detector utilizes two distinct subsystems. First is the the SiT (Silicon tracker), providing a precise position information for reconstruction of tracks of the passing particles. The second is the ToF (Time-of-Flight), with only a rough position sensitivity (four distinct areas), but extremely accurate timing resolution reaching into low tens of picoseconds.

The detector assembly occupies a Roman Pot (RP) container capable of horizontal movement towards and away from the beam. The detector packaging needs to be very compact due to the limited volume available – a cylinder with a diameter of 130 mm and 135 mm tall. The AFP RP can be seen in Figure 1.3.

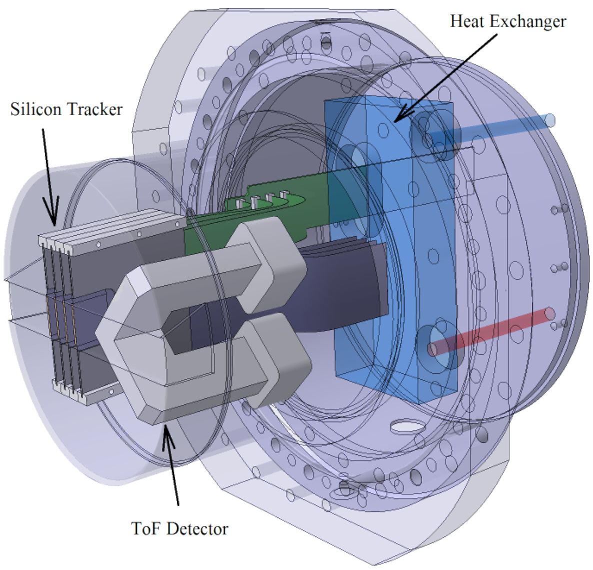

Figure 1.3: The AFP Roman pot with ToF as originally described in the AFP TDR [5]. The current system is a significant evolution of this original proposal, details of this process will be described in the following chapters.

As there are two AFP stations on each side of ATLAS, the ToF system is placed only in the far station on each side. This is mainly due to the fact that ToF presents a significant amount of material close to the beam and operation of the far station would be hindered by frequent secondaries and showers originating in the near station if the bulky ToF Cherenkov radiators were present there.

1.2.1 Silicon tracker

The silicon tracker (SiT) for AFP [5] utilizes 3D silicon sensors with FEI4 readout chip, which has been proven to handle high hit rates and radiation loads. The sensor covers a $20 \times 20\,\text{mm}^2$ area with $50 \times 250\,\mu\text{m}^2$ pixels and is edgeless. The edgeless design allows us to get the active area very close to the Roman Pot bottom, thus recording hits as close to the beam as possible within the permissible Roman Pot position range. The smaller pixel size is oriented for a better resolution of the hit distance from the beam (x axis), which is of the most interest as it carries the information about the energy of the detected protons.

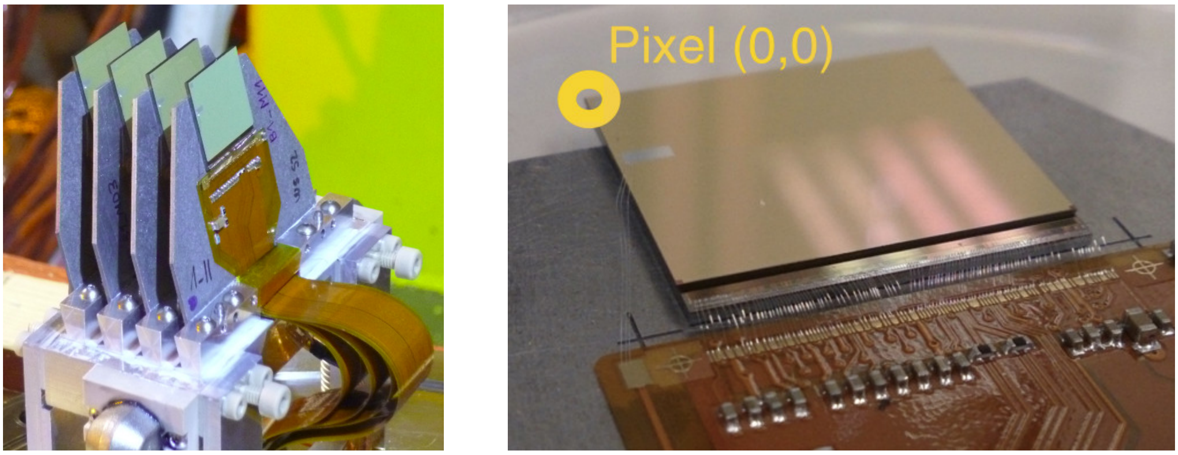

Figure 1.4: The four planes of the AFP silicon tracker mounted on its holder with heat exchanger (left) and a detail of a single tracker plane with its delicate wire bonds visible (right).

The SiT 3D silicon planes are angled 13° as can be seen in Figure 1.4, which allows for exploitation of several advantages over planar silicon detectors. The angle helps to boost the efficiency as particles pass a longer path through the material and dead areas between the pixels are eliminated in the x axis. Having the SiT angled forward also allows for a slightly more space for placement of the ToF system. The four individual planes are mounted on a holder using precision pins in a staggered fashion in both x and y, which improves the spatial and angular resolution of the reconstructed particle tracks. The tilt of the planes also allows for a further improvement of the positional resolution in the x axis via sub-pixel position sensitivity[1].

1.2.2 Time-of-Flight system

The AFP Time-of-Flight system is a Cherenkov-based fast timing detector complementing the AFP silicon tracker. As can be seen in Figure 1.5, it is mounted behind the SiT as it introduces a lot of material into the particle path, being prone to generate secondaries or even showers. This is also the reason why it is not present at all AFP stations, but only at the station downstream (far station) on each side. A more detailed view of the AFP tracker planes and ToF bars is in Figure 1.6.

The AFP-ToF system uses fused silica bars to produce Cherenkov radiation and guide it via internal reflection to an appropriate light sensor. A microchannel plate

[1] As the particle often passes through the volume of two neighbouring pixels due to the angle, the ratio of charge deposition in them can be used for sub-pixel position sensitivity.

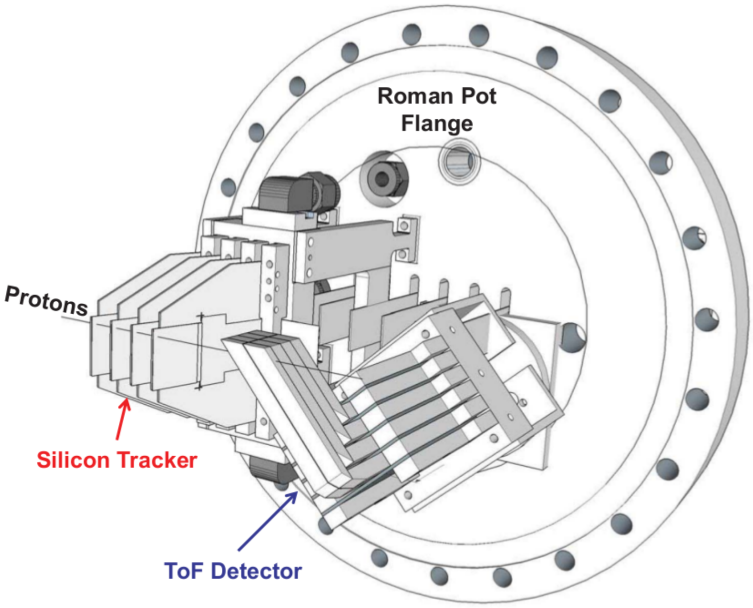

Figure 1.5: A sketch of the AFP detector package mounted on its flange. The proton to be detected passes through four tracker planes, followed by the ToF Cherenkov bars. The ToF subdetector is present only in the far stations on each side and typically contains a 4×4 matrix of bars, unlike the 2×4 depicted here. The LHC beam passes a few millimetres to the left from the detector edge, parallel to the example proton track.

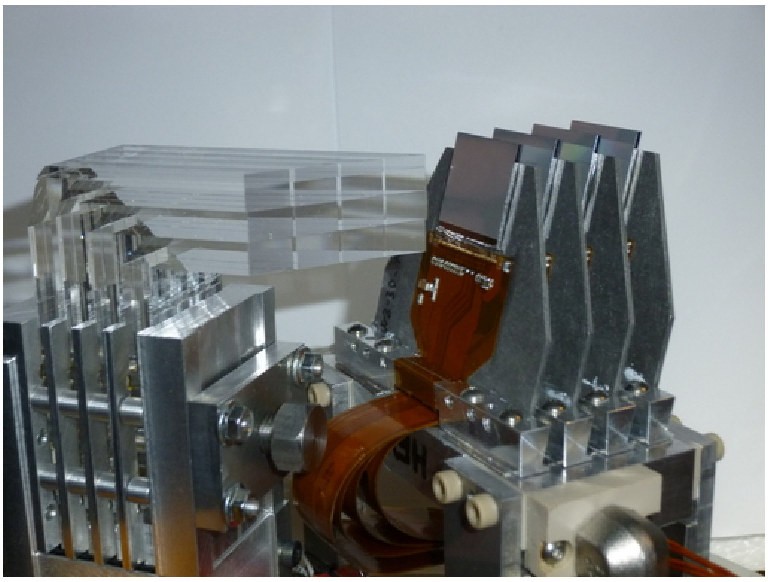

Figure 1.6: A photo of the AFP detector far station with SiT planes on the right and ToF bars on the left. The 4×4 bar arrangement and $90°$ L shape are clearly visible. The bars are angled $48°$ compared to the beam direction, with an appropriately cut end plane parallel to the beam.

photomultiplier tube serves this role as these tubes are known for their excellent timing resolution. A chain of amplifiers and signal processing circuits follows before feeding the signal into a high precision clock for digitization. The resulting timestamps on each side are then compared, allowing for pinpointing of the vertex from which the pair of protons originated or discarding them as accidental pairing of unrelated forward protons, each coming from a different collision event.

The detailed motivation for construction of the AFP-ToF system follows in section 1.3, an in-depth description of the system and all its parts and signal processing stages is in chapter 3.

1.3 Motivation for a vertex-matching ToF

In particle detectors, a pileup is a situation where multiple distinct collisions occur very close in time and are detected together within a single detector readout. The ToF system is designed to counter in-time pileup (multiple collisions within one bunch crossing). The AFP system does not suffer from out-of-time pileup as the tracker can differentiate between different bunch crossings on its own. The central ATLAS detector lacks precise timing capability, but is capable of handling pileup through matching particle tracks to spatially distinct vertices, something the AFP tracker cannot do with its forward placement and therefore a very long lever arm.

As the diffractive events where both leading protons survive (central diffraction) are exceedingly rare, they are obscured by an overwhelming amount of accidental pairings of single diffractive protons originating from different collision events within the same bunch crossing, as shown in Figure 1.7. During a typical LHC run with high in-time pileup, these form an irreducible background in studies of interactions (such as exclusive production) where both leading protons survive and need to be properly matched.

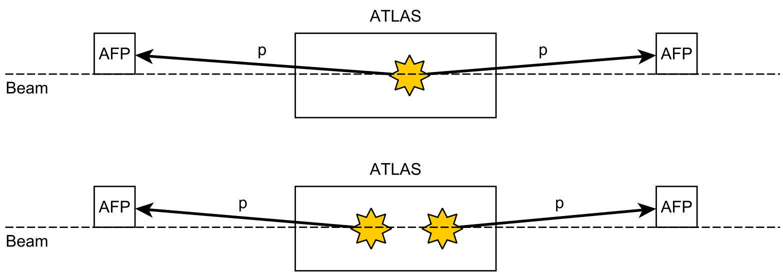

Figure 1.7: AFP double tag events with protons reaching AFP stations on both sides. The top diagram shows a true double tag with both protons originating from a single interaction (yellow). The bottom diagram shows a false double tag pairing with each proton originating from a different interaction.

The job of the ToF system is to match a proton pair to a collision vertex in IP1 or determine that it is a case of the above described fake pairing of protons which are actually coming from two separate collisions. The level of background suppression is directly related to the timing resolution available for this matching. In the case of AFP, the initial target is $< 30\,\text{ps}$ resolution, with $10\,\text{ps}$ being the long term goal.

An example of the vertex distribution at ATLAS is in Figure 1.8. The vertices are enough spread out along the beam axis z, allowing for their matching with the protons in AFP via timing. A detail of the vertices in a single bunch crossing is in Figure 1.9.

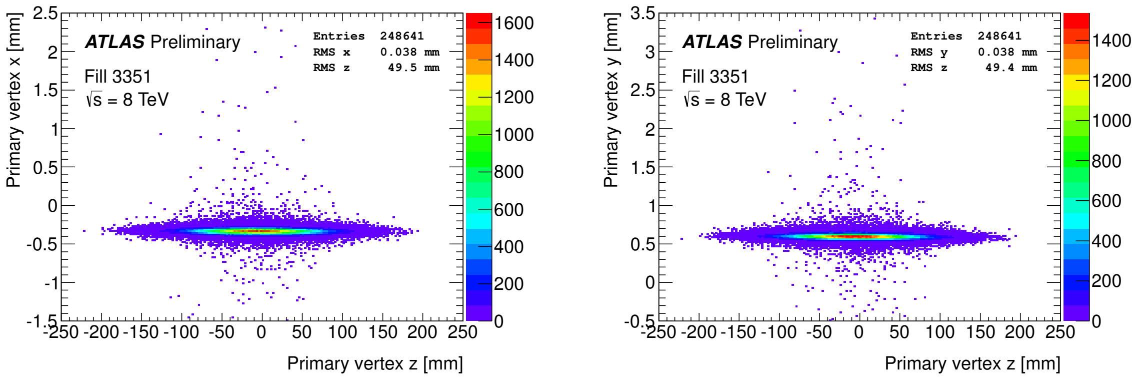

Figure 1.8: The x-z and y-z projections of the vertex distribution in the ATLAS detector during the fill 3351. The distribution is subject to change depending on the optics and beam quality of a given LHC fill, nevertheless, the prolonged shape along the beam direction is always maintained. Image credit: ATLAS Collaboration.

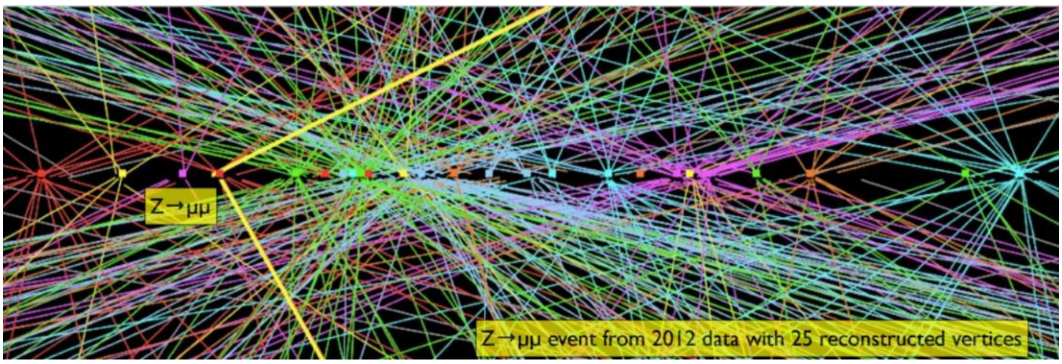

Figure 1.9: An event with severe in-time pileup of 25 reconstructed vertices as recorded by the ATLAS central detector in 2012. The beam crossing area shown is $\sim 6\,\mathrm{cm}$ long. Credit: ATLAS Collaboration.

In order for an AFP proton tag to be matched to the actual collision vertex by ToF, the ToF detectors on both sides of the ATLAS interaction point need to detect one proton each, both originating from the same collision (a double tag). This requirement is due to a missing precise time reference when the collision itself occurred, as each bunch crossing takes hundreds of picoseconds due to the actual length of the bunches[2].

The expected z coordinate of the vertex is calculated from the difference of these two timing measurements as

$$z_{\mathrm{ToF}} = c(t_{\mathrm{C}} - t_{\mathrm{A}})/2\,, \tag{1.1}$$

where t_{C} and t_{A} are times measured at the 'C' (Clockwise) and 'A' (Anticlockwise) sides of the ATLAS interaction point IP1; the z coordinate is oriented along the beam and increases towards A side. The relevant ATLAS coordinate system is marked in Figure 1.2.

The speed of light c in Equation 1.1 is more than a good enough approximation of the speed of the very highly relativistic protons at the TeV energy scale, as 7 TeV protons move at $0.999999991c$. This results in a systematic error of just under 6 fs on each of the two ToF detectors, three orders of magnitude below the expected resolution of the ToF system. However, since there is currently no central detector timing available on ATLAS and ToF operates only by subtracting the two measurements on A and C side, these already tiny errors mostly subtract and propagate as a simple factor of 0.999999991 on the z coordinate, making the resulting error of the $v \approx c$ approximation truly insignificant.

[2]If ATLAS had a precise timing capability in the central detector, single tag events could be matched too, while double tag events would benefit from a further improved matching precision.

Chapter 2

Cherenkov radiation in particle detectors

Cherenkov radiation (described in more detail in section 2.1) is not as widely used in particle detectors as other particle-matter interactions. This can be mostly attributed to low light yield per unit of detector material length. However, for sub-ns timing systems, it is very advantageous due to the fact that the photons are produced instantly as the particle passes through, unlike the significant random delay present for example in scintillators.

The Cherenkov radiation is a pivotal phenomenon for the AFP-ToF detector. It is the source of the optical signal, which is used for the precise timing measurements carried out by the detector.

Other notable uses of Cherenkov radiation in particle detectors often revolve around particle classification. The RICH (Ring-imaging Cherenkov) detectors utilize a Cherenkov radiator coupled together with a position sensitive photon detector (often aided by a focusing mirror), allowing to measure the Cherenkov angle and thus classifying particles. Another example are differential detectors such as CEDAR [8], typically employed at beamlines due to their narrow constraints on particle direction and momentum.

Neutrino experiments like Super-Kamiokande and IceCube Neutrino Observatory use Cherenkov cones to detect events of neutrino interactions within their immense volume, producing either a muon or an electron event. Examples of those from Super-Kamiokande are in Figure 2.1.

Cherenkov radiation is used in the renowned Pierre-Auger Observatory (PAO) as the detection mechanism in the ground stations covering a large area of the Argentinian pampa [9]. It is also at the core of the proposed Cherenkov Telescope Array (CTA) astroparticle experiment [10], where the Cherenkov cones are quite narrow due to the low refractive index of atmosphere (atmosphere is the detection medium here).

2.1 Origin of Cherenkov radiation

Cherenkov radiation is emitted when a charged particle passes through a dielectric medium where the speed of light in that medium c/n is slower than that of the particle v_{p}. This $c/n < v_{\mathrm{p}}$ requirement can be easily fulfilled by highly relativistic particles travelling through materials like water, glass or even air.

The behaviour of Cherenkov radiation described further is relevant for isotropic medium only, with the passing charged particle not considered to be polarized. Behaviour of Cherenkov radiation in anisotropic materials becomes much more compli-

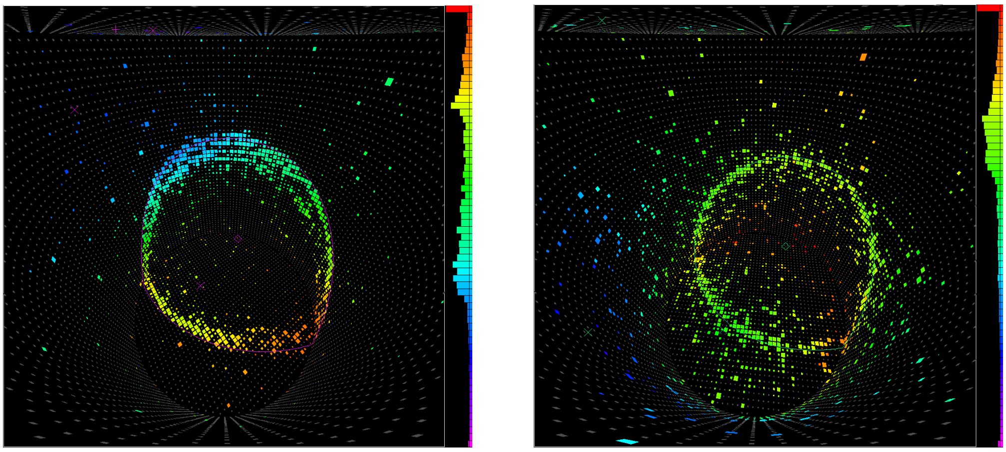

(a) **(b)**

Figure 2.1: Cherenkov rings produced by a a muon and b an electron, both originating from neutrino interactions within the Super-Kamiokande neutrino detector. The colour scale shows time progression, allowing for good directional sensitivity. Credit: Super-Kamiokande collaboration.

cated with orientation dependency, possible presence of multiple separate Cherenkov cones produced and even their elliptic deformation [11].

The Cherenkov radiation in an isotropic medium is emitted at any given point along the particle path as a characteristic cone pointing forward. As the particle travels forward, the Cherenkov photons form a coherent wavefront, cross section diagram is in Figure 2.2. The Cherenkov light is polarized with the polarization vector perpendicular to the cone, aligned with the wavefront [12].

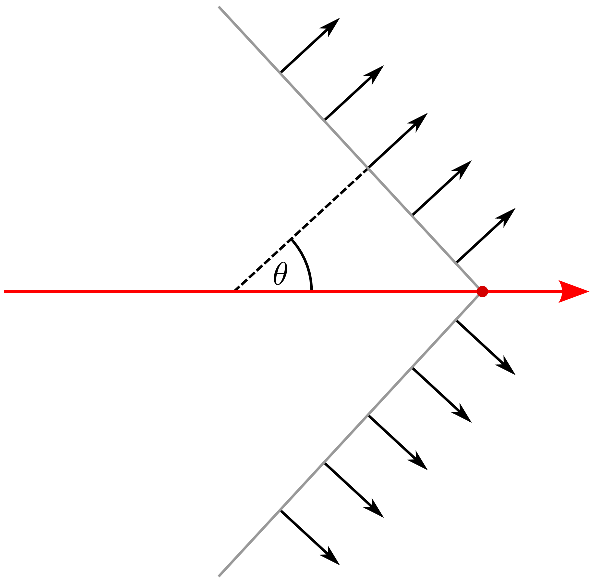

Figure 2.2: Cherenkov radiation produced by a particle (red) forms a wavefront of photons (grey) propagating outwards. The angle θ of the cone (dashed + arrows) can be determined using Equation 2.1.

$$\cos\theta = \frac{c}{n v_{\mathrm{p}}}\,. \tag{2.1}$$

In reality, the angle is not fixed and varies even for individual Cherenkov photons generated within a single particle pass. This is due to the fact that there are various emitted wavelengths, therefore dispersion causes the refractive index to be a function of the wavelength (or frequency) and this variation propagates to the angle θ through Equation 2.1. The Frank-Tamm formula in Equation 2.2 describes the energy E emitted per unit of length x at the individual frequencies, μ is the permeability of the medium and q the charge of the particle, where in our case we can use the elementary charge e.

$$\frac{\mathrm{d}E}{\mathrm{d}x} = \frac{q^2}{4\pi} \int_{v_\mathrm{p} > \frac{c}{n(\omega)}} \mu(\omega)\omega \left(1 - \frac{c^2}{v_p^2 n^2(\omega)}\right) \mathrm{d}\omega\,. \tag{2.2}$$

2.2 Propagation of light in the AFP-ToF bars

In the particular case of AFP-ToF, we can approximate $v_\mathrm{p} \simeq c$ in order to simplify the above general case relations, just as we did previously in section 1.3. This way the Cherenkov angle given in Equation 2.1 becomes simply

$$\cos\theta = \frac{1}{n}\,. \tag{2.3}$$

The refractive index n of fused silica, the material of the ToF radiator bars, is around 1.5 in the blue and near UV range of wavelengths (see Figure 2.3), where most of the Cherenkov radiation falls. We can therefore approximate the most typical Cherenkov angle using Equation 2.3 as $\theta = \arccos(1/n) \approx 48°$. This is where the 48° angle of the ToF radiators comes from, ensuring a part of the cone is captured and transported with a minimal need for internal reflections (also making the total path shorter), optimizing detector efficiency. This has been confirmed with Monte Carlo simulations performed using the Geant4 simulation framework [13].

The situation in the AFP-ToF LQbars is complicated by the fact that they are not straight, but feature a 90° angle due to spatial constraints of the Roman Pot container. Therefore being emitted at the range of angles that proved total internal reflection in the radiator part of the bar is not a sufficient condition for them to be able to reach the PMT. To improve the chances of the photons, the surface where most of them impact at the ankle has a mirror coating applied.

An illustration of the various photon paths is in Figure 2.4. The red path is the most straightforward, with the photon travelling relatively parallel to the bar and reflecting off the mirror coating at the ankle. These photons reach the PMT the earliest. The green scenario is of a photon that misses the mirror and hits the angled part of the bar behind it. It then depends on the incidence angle whether it gets reflected and has a chance of reaching the PMT or it is lost. Even if the photon is captured, it takes a longer path with many reflections and is also more likely to reflect off the bar end near the PMT. There are certain modifications of the bar shape to capture more of these photons that will be discussed later. The last scenario, blue, is a case of a photon that hits the mirror at such an angle that it is reflected backwards. Even if it managed to stay in the bar and reflect again off the bar edge, it would reach the PMT too late to have any effect on the timing measurement.

More details about the Cherenkov light propagation through the ToF bars can be found later in this work and in [1, 17].

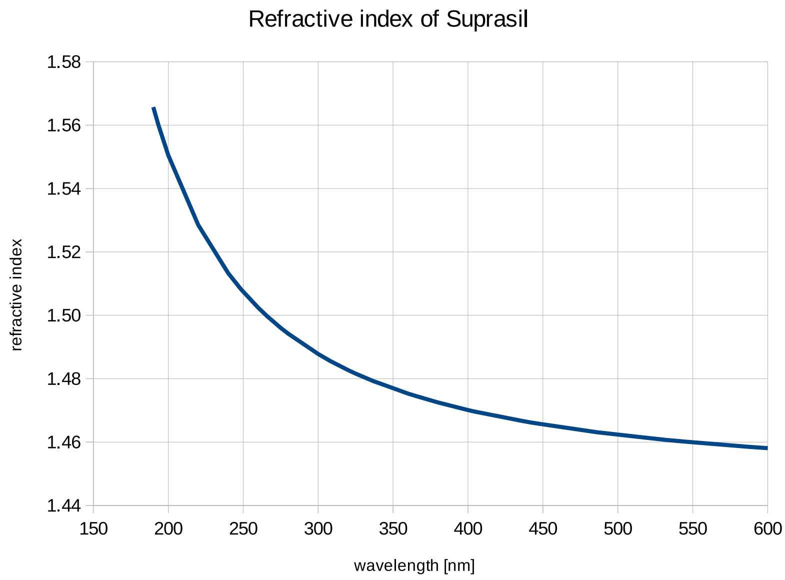

Figure 2.3: Refractive index of Suprasil. Suprasil is a commercial name for a particular variant of commercially available fused silica materials. Suprasil is equivalent to SK-1300, the specific material used in the construction of the AFP-ToF Cherenkov bars [14]. The values in the plot were extracted from the relevant Suprasil datasheet [15]. The values are equivalent to those in the SK-1300 datasheet [16], but with significantly more data points at short wavelengths, giving a better picture of the refractive index in the area of our interest.

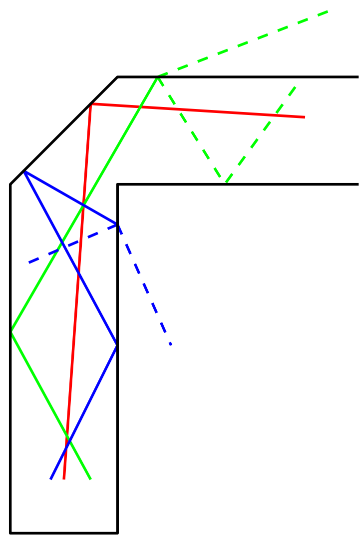

Figure 2.4: Photon propagation scenarios near the LQbar ankle. The photons originate in the lower part, propagating upwards

Chapter 3

Original AFP-ToF design

In this chapter, the ToF design in 2016/2017 (shortly after the author joined the project) is described and characterized. This state is very close to the original Technical Design Report [5] design published in 2015, although some aspects were already modified following the first beam test of an early prototype in 2015. The AFP-ToF detector as described here was installed on the LHC in February 2017.

3.1 AFP Roman Pot and flange

The Roman Pot (RP) is a type of a particle detector container intended for operation very close to the particle beam in the forward area. Roman Pots serve as an interface between the high grade vacuum inside the accelerator beamline and the outside, allowing for insertion of detector equipment close to the beam without it having to be placed in the primary vacuum.

The RP for AFP is made of stainless steel and has a very thin ($300\,\mu$m) “window” machined in it to present as little material close to the beam and in the way of particles passing the active part of the detector. The pot with the window is in Figure 3.1. The inside of the Roman Pot contains a secondary vacuum in the range of $5-30\,$mBar in order to prevent deformation of this thin window due to pressure difference and also prevents condensation formation on the actively cooled SiT.

To hold the secondary vacuum, the RP flange must provide a good vacuum seal, which is accomplished via knife edges that bite into a copper single use sealing O-ring (Figure 3.2). All signal and power supply lines must also use vacuum-tight feedthrough solutions. The fact that the photomultiplier is placed in the secondary vacuum imparts severe requirements on proper electrical insulation due to the presence of high voltage of $\sim 2\,$kV.

3.2 Cherenkov radiator bars

3.2.1 Bar design origins

The radiator bars for AFP-ToF detector are made of fused silica, an amorphous quartz glass. We used specifically a quartz material with commercial designation “SK-1300” produced by OHARA GmbH. SK-1300 is equivalent to the known “Suprasil” available from other manufacturers, for example Heraeus Conamic or UQG Ltd. The design of these bars is based on the QUARTIC [18] Cherenkov counter with the angled bar design, shown in Figure 3.3. In our case however we needed to fit the detector inside the

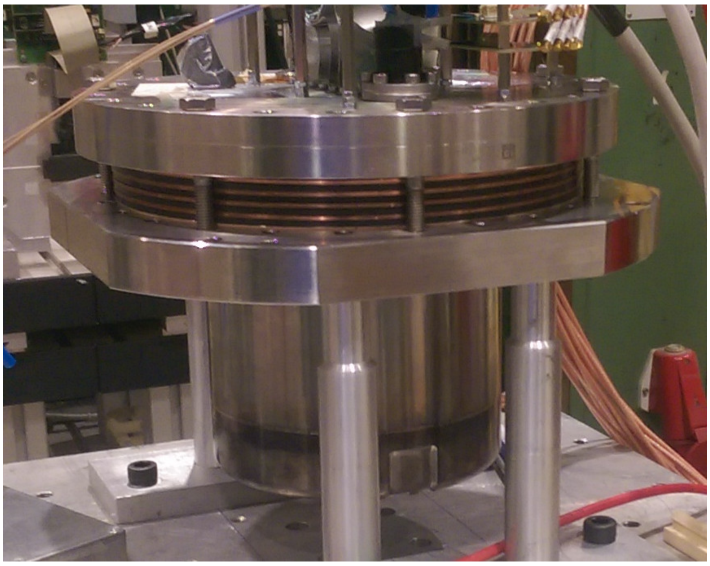

Figure 3.1: A Roman Pot with the thin window machined at the bottom, as used at a Beam Test. At the top of the pot, a flange with the actual detector hardware is mounted, while the pot is just a container. Mounted on the LHC, the pot would not stand upright as shown here, but be on its side instead, rotated around the beam axis. Multiple sealing rings are stacked between the pot and the flange here; this is to get extra safety clearance of the detector edge from the bottom. At the LHC, a single copper ring will be used and a proper height alignment of the detector will be done, ensuring a tight clearance from the pot bottom.

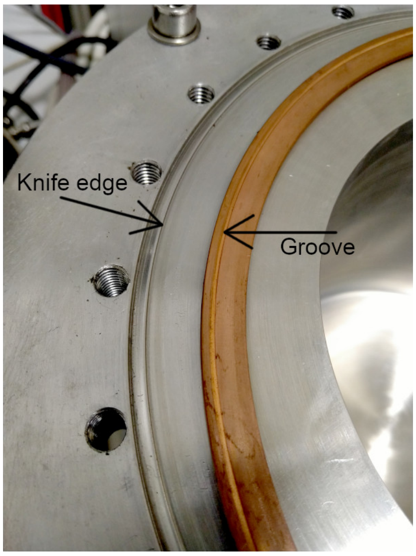

Figure 3.2: A knife edge on the AFP Roman Pot with a used sealing copper O-ring next to it. The groove in the ring is clearly visible; to ensure a proper seal, a new ring without the groove and coated with a vacuum grease must be used each time the pot is closed.

Roman Pot container of the AFP system, therefore they are L-shaped due to spatial constraints, as can be seen in Figure 3.4. Note that this is different than the L-bar QUARTIC variant, which has the radiator part parallel to the particle path.

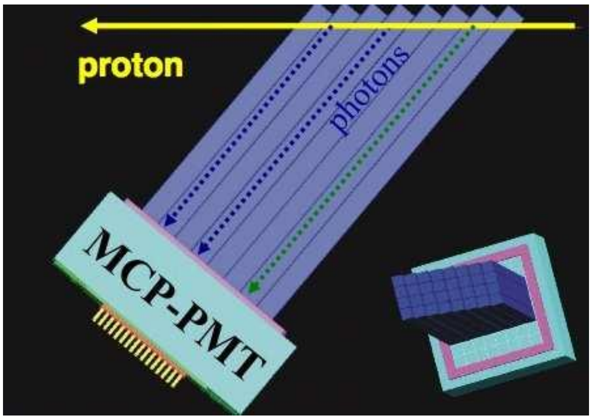

Figure 3.3: The QUARTIC fast timing Cherenkov detector, which served as a basis for the AFP-ToF design. Image credit: [18].

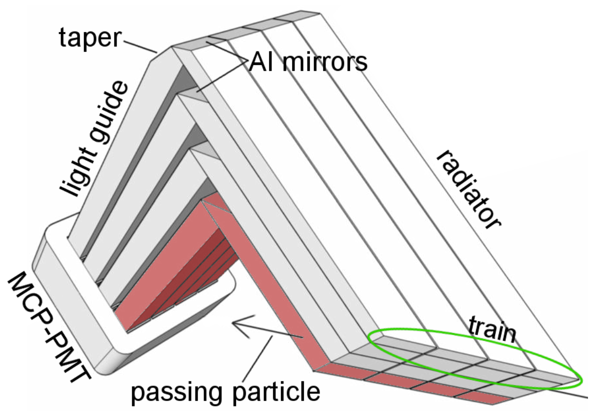

Figure 3.4: The ToF cherenkov bar design. The bars are organised in a 4×4 matrix, whith each passing particle hitting four in a row, which we call a "train". One such train where a signal is generated by a passing particle is marked in red. The bars are angled 48° from the particle path to optimize light capture and transfer via total reflection.

3.2.2 Specifics of the AFP-ToF L-shaped bars

The 90° L-joint in each ToF bar unfortunately incurs several weaknesses into the system:

- significant loss of light and a risk of optical crosstalk,
- need to apply a mirror coating to reduce losses near the L-joint, increasing complexity of the production process,
- the glued joint (using the Epotek 305 optical grade epoxy) is mechanically fragile, limits wavelengths that can pass and is a radiation hardness weak point (Figure 3.5).

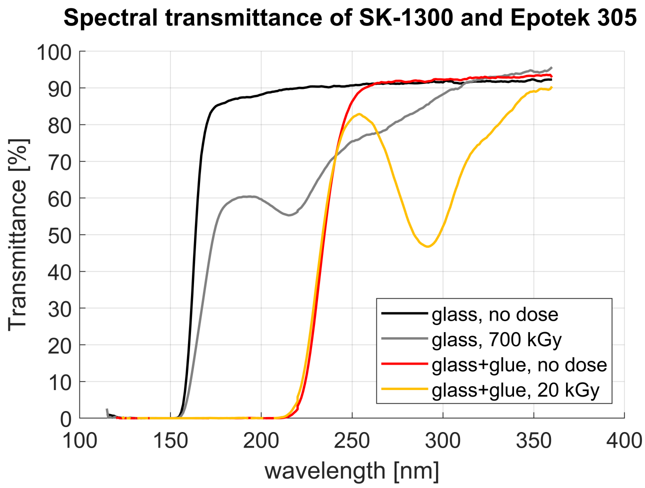

Figure 3.5: Spectral transmission of the relevant materials before and after irradiation tests. SK-1300 quartz glass, the material used in ToF bar construction, is examined in the grayscale curves that reach into lower wavelengths. The combination of the quartz glass with the Epotek 305 epoxy, plotted in colour, is seen to have a shifted transmission threshold to 250 nm even without irradiation and a significantly degraded transmission already after experiencing a much lower dose than what the quartz can withstand, showing the epoxy to be the radiation hardness weak point. This plot has been previously published in [19].

A further modification compared to QUARTIC is the angled surface at the end of the bar, made parallel to the particle path, which we call "the edge". This arrangement helps gather more light for hits close to the edge, as they get reflected back into the bar instead of losing them as in the QUARTIC system. This effect is visualized in Figure 3.6.

3.2.3 Single vs opposing ToF setup

The ToF as described in the AFP TDR [5] has already somewhat evolved before the author joined the project in 2016. The most notable change was the use of a single-PMT ToF on each side for a more cost-effective result with only a small impact on performance, where the TDR presumed two ToF assemblies as in Figure 3.7. At a first glance, this would halve the rate capability of the system. However, the events of interest have a strongly non-uniform pattern under an angle as shown in Figure 3.8, resulting in the significant hotspots still hitting mostly one of the two opposing bar trains in many cases, not evenly splitting across them. Absence of the edge in the most exposed area in case of the single-ToF variant also prevents a hypothetical loss of events due to imperfect alignment of the opposing bar pairs.

A visible impact of the single ToF assembly approach is however on the amount of light gathered, which is much improved near the bar edge as previously shown in Figure 3.6. With the single PMT layout, the majority of events hit roughly 1 cm from the edge, completely negating this effect for the first bar in each train and mostly for the second ones too. This, together with a typical PMT non-uniformity (lower gain at corners and edges), is causing the first bars in each train to have noticeably less signal (lower both amplitude and efficiency) compared to the rest of the bars, as was previously shown in [1]. A detailed plot of the own photon generation and accepted

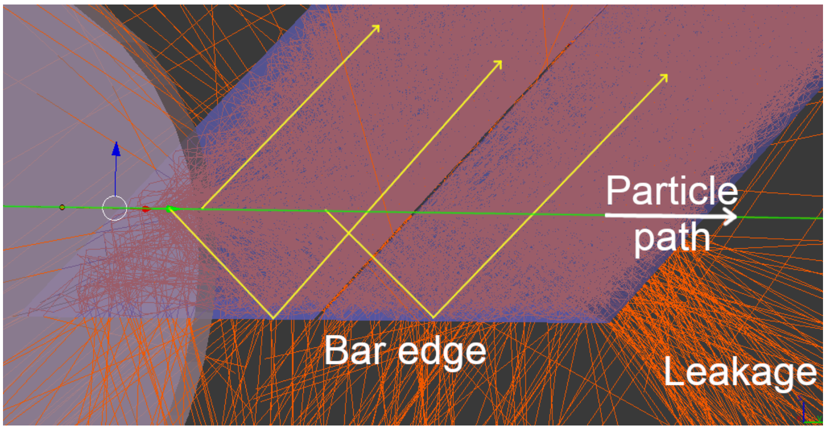

Figure 3.6: A simulation of the Cherenkov light generation and propagation in the ToF bars near the bar edge. A particle path is marked in green, the produced photons in orange. A few of the photons travelling either straight or via edge reflection are highlighted in yellow. Note that the photon can be reflected and accepted by the next bar in the train, which turns out to be also helpful for signal strength and timing resolution of that bar, as discussed in the author's master's thesis [1]. The last bar in the train leaks a lot of light through the same mechanism as there is no next bar to accept it (while not all of the photons necessarily originate in that bar, depending on the particle distance from the edge).

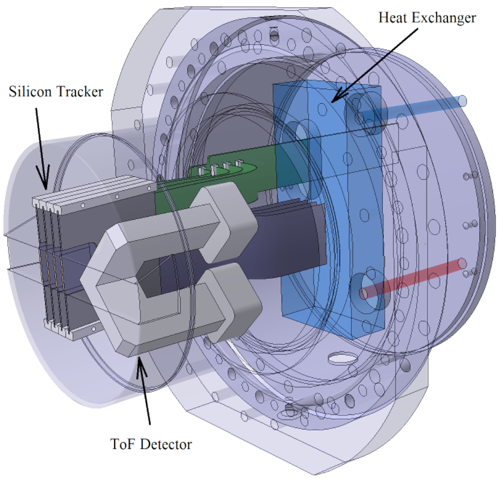

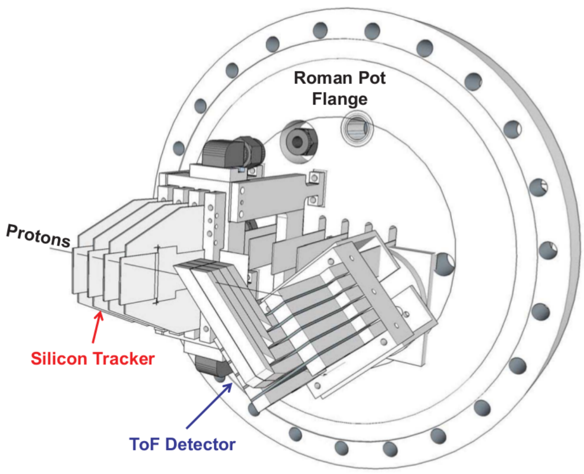

Figure 3.7: The AFP Roman pot (left) with ToF as described in the AFP TDR [5]. Note the major difference compared to the subsequent development up to 2016 (right): the opposing double-ToF assembly setup. Only two bars per train are present in these models as that was the setup being initially tested before more bars were produced.

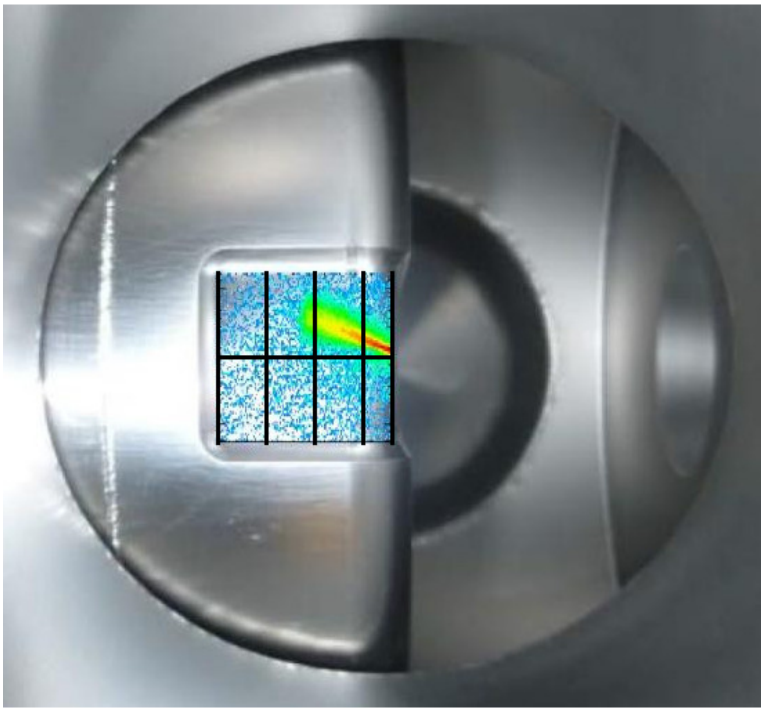

Figure 3.8: A view of the AFP Roman Pot container in the beamline from the point of view of the incoming beam. The pot can retract away from the beam to a “garage position” to the left when not in use. A typical diffractive pattern as recorded by the AFP SiT is laid over the thinly machined window near the bottom of the pot, where the active area of the AFP detector is. The layout of the bars is marked with black lines, the horizontal line showing where the two opposing ToF bar assemblies would meet with their bar edges if the original double ToF design was used. In the single ToF variant, only a single edge is present at the top of the active area. The vertical lines mark the individual ToF bar trains.

leakage fractions in the second bar is in Figure 3.9. The plot shows that a bar gradually stops benefiting from reflection on it's own edge with increasing hit distance from the said edge. At about 5 mm distance (after adding half the height of the trigger window), no light is reflected from the edge and is leaked downstream, where further bars might benefit from it instead.

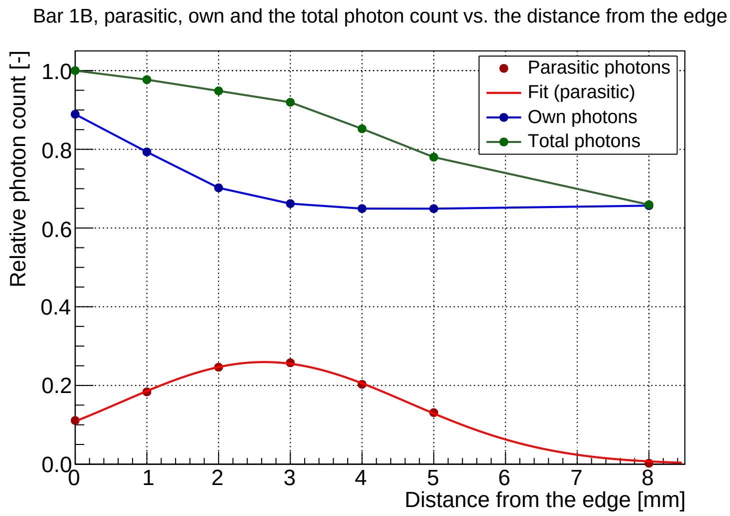

Figure 3.9: Simulation of own light retention and accepted light leakage (parasitic photons) from the previous bar for various hit distances from the bar edge. The values are represented as fractions of the total detected number of photons by the PMT in the best case (0 mm on x axis). This plot represents the second bar in a train and originates from the same simulation as the visualization in Figure 3.6. The distance from the edge here is not of the particle, but a 3 mm tall trigger area, which shifts the axis by 1.5 mm and smears the results slightly, explaining why there is observable photon transfer at zero distance. The plot shows how the light leakage helps to partially compensate the significant reduction of total detected photon count for hits further from the edge. This figure has been previously published in [14].

3.2.4 Bar thickness and taper

The bar thickness has also changed. Compared to TDR where uniform thickness was assumed, the ToF radiator bars closer to the LHC beam are thinner to roughly equalize rates as these regions experience higher particle flux. The precise flux distribution depends on the accelerator optics used in a given LHC fill.

The thinner bars closest to the beam (train 1) require a taper right after the L joint, which has advantageous effect on capturing more light that would normally escape and is also straightening paths of photons that would otherwise travel through the rest of the bar with many reflections Figure 3.10, essentially accelerating their arrival to the PMT. This helps these bars to achieve better timing resolution and trigger efficiency. A similar approach cannot be used on all the bar trains however as it would reduce the active area of the ToF system too much, resulting in only a partial coverage of the silicon tracker planes.

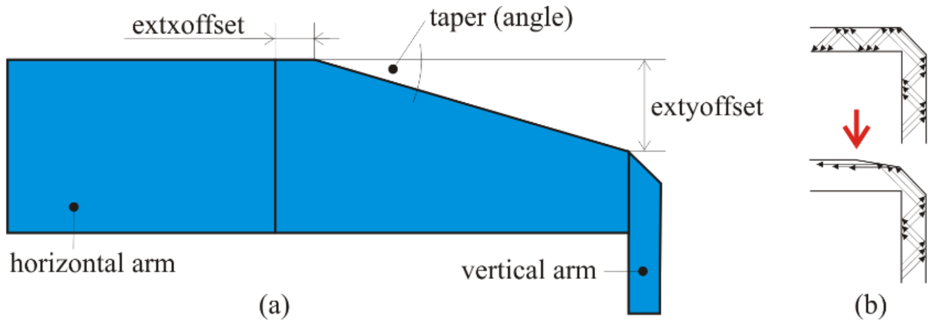

Figure 3.10: Schematic of the taper implemented near the right angle joint of the LQ bars (a) and the effect it has on the photons that miss the mirror surface at the ankle (b). Proportions of the bar in (a) are excessive for illustrative purposes. This has been previously published in [13].

3.2.5 Timing dependence on hit position

The ToF timing information is linearly dependant on the distance x of the detected particle track from the bar edge, with light from hits at higher x arriving sooner. This is due to the fact that while the light is generated later as it enters the angled bar at higher x, the photons produced have shorter path, which impacts the timing much more as they travel slow due to the refractive index of ~ 1.5. The magnitude of this effect could be geometrically calculated for a given wavelength, but the Cherenkov light is spread over the blue and near UV spectrum and the refractive index varies (Figure 2.3). Therefore the most straightforward approach is to use Monte Carlo simulation that takes the spectrum and its interaction with the ToF bars into account. The result of such analysis is in Figure 3.11, showing a dependence of about 4 ps/mm. This is very significant given the target ToF resolution is few tens of ps, making the variability 80 ps across the 2 cm SiT sensor size. SiT hits therefore need to be paired to ToF hits even for timing processing and compensation of the x coordinate dependence has to be applied to mitigate this source of smearing.

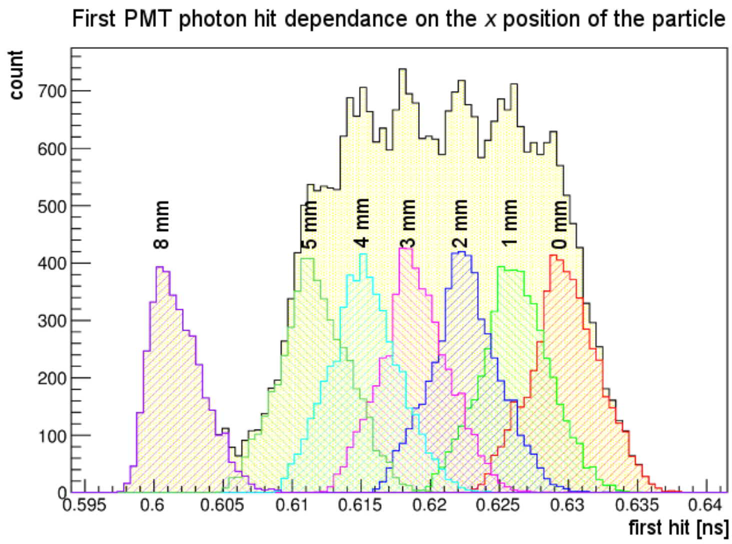

Figure 3.11: Dependence of ToF timing on the x coordinate of particle hit (distance from bar edge) as obtained from simulation. The time shift is roughly 4 ps/mm.

Another effect of timing dependence on hit position is in the y coordinate as well, although tracker information is not needed to correct for it. That is because it is not a continuous linear shift as in case of the x coordinate, but simply a dependence on which train the particle hit. The effect is again of a simple geometrical nature as the bars of different trains have variations of length, resulting in an extra path the light signal has to travel through the trains closer to the beam. This can be corrected for by a simple fixed offset applied on the timing information obtained from each train.

Many more details about the design of the bars and light propagation in the ToF optical part can be found in [1, 13, 14, 17].

3.3 Considerations of using optical contact

The use of optical contact (immersion) was considered for application between the ToF bars and the PMT face. This was expected to improve signal strength by mostly eliminating undesired reflections from the bar end, while potentially improving the timing resolution as well.

The assumptions about optical contact effectiveness were put to test using a Monte Carlo simulation. The results in Figure 3.12 show that the later arriving photons would benefit the most (those with many reflections), but the first wave that most contributes to the signal edge used for timing [1] is not improved that significantly. This corresponds to the timing resolution results which are mostly unchanged. Put simply, only the photons that are generated under a steep angle against the bar walls and travel longer through many reflections have a significant benefit from the application of the optical contact. This is easily explained by the fact that they are the most likely to otherwise reflect from the bar end due to their incidence angle, unlike the early arriving photons travelling mostly parallel to the bar length that reach the bar end nearly perpendicularly.

As can be seen in Figure 3.12, the application of optical contact clearly benefits the trains without a taper more. The train 1 with taper manages to straighten the paths of the photons with many reflections (as discussed in subsection 3.2.4), preventing them from reflecting off the bar end and also ensuring they arrive earlier. For this reason, the optical contact is not very useful in train 1, but has a serious impact in the other trains.

A decision was made not to use any optical contact due to the small impact on timing and a high risk factor. The risks include questionable vacuum stability in the secondary vacuum (risk of outgassing and coating the equipment inside the pot) and unknown radiation hardness, risking quick deterioration of the transmissive properties.

3.4 MCP-PMT

Microchannel Plate Photomultipliers (MCP-PMTs) are a specific type of photomultiplier tubes utilizing a microchannel plate (MCP) as the amplification apparatus. A cross section diagram with electron paths marked and a picture o the device itself is in Figure 3.13.

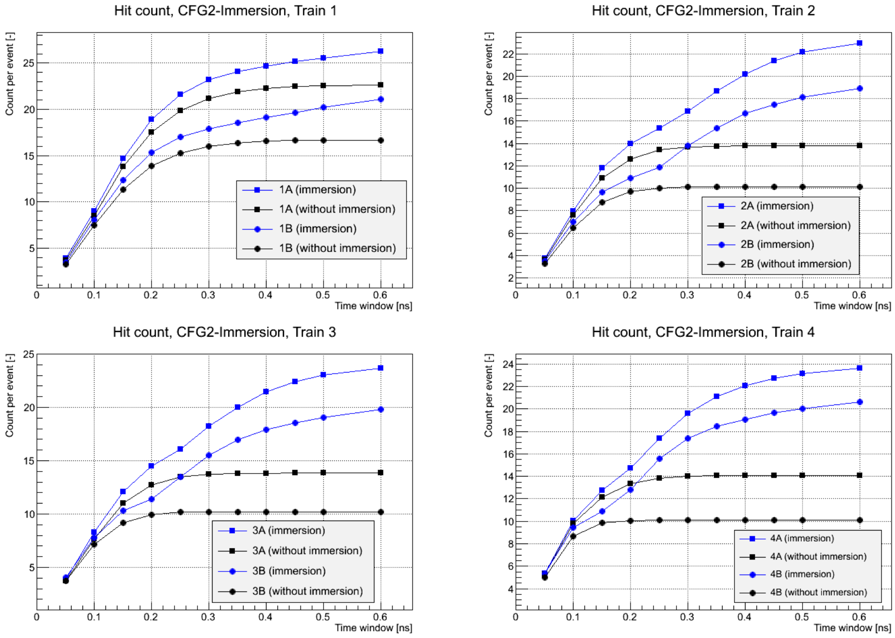

Figure 3.12: Cumulative plots of photon arrival over time, showing the effect the optical contact would have on the signal in the individual ToF trains.

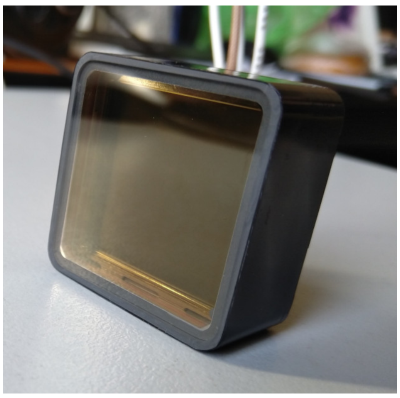

(a) Photonis miniPLANACON

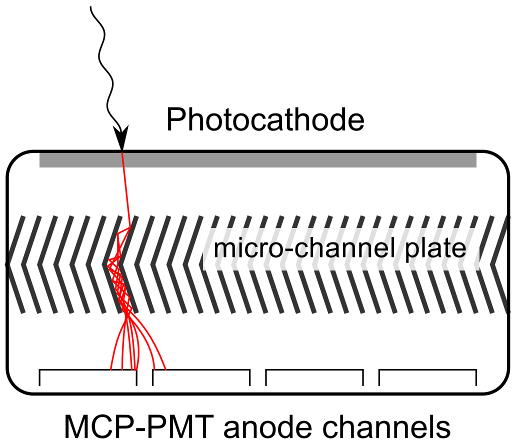

(b) MCP-PMT Cross section

Figure 3.13: A photo of a Photonis miniPLANACON MCP-PMT (a) and a cross section view of a typical MCP-PMT device (b). In the cross section diagram, a single photon hits the photocathode and is converted to a photoelecron, which is then multiplied and the resulting charge is collected on the anode pads. The electron propagation and multiplication in the MCP is marked in red. Proportions of the MCP thickness and pore size to the PMT body in (b) are not realistic.

3.4.1 General properties

The MCP is typically made of a glass substrate $< 1\,\mathrm{mm}$ thick, covered with tightly packed pores running through it. The inside surface of the pores is covered with a special emissive layer. The front and back are coated with metal and connected to a high voltage supply, creating a potential gradient along the pores. Electrons created by the photocathode are accelerated by a front stage potential towards the MCP front face. Those that are accepted by a pore then hit its internal wall, kicking out multiple electrons. These secondary electrons are then accelerated along the pore by the high voltage bias applied over the MCP, hitting its wall again. This way a multiplication cascade is created.

Most MCP-PMT devices use two MCP plates in cascade with a narrow gap between them, spreading the electron cloud from one pore into multiple ones for greater multiplication. These devices can easily reach gain of $10^5 - 10^6$ required for detection of single photon events. The PMTs used for AFP-ToF are of this type.

The MCP-PMT technology has a number of advantages as compared to a classical photomultiplier tube. The most obvious is a small package (short length). There is also an easy possibility of segmenting the anode pads, providing hit position sensitivity. Another advantage is high tolerance of strong magnetic fields up to several T [20, 21] due to the fact the electrons travel only very short free paths, mitigating any significant bending of their trajectories by the external magnetic field. The short paths within the MCP also allow the MCP-PMTs to reach very good timing resolution of few tens of picoseconds or even less [22, 23].

In the original ToF design, the Photonis miniPLANACON XPM85112 [24] MCP-PMTs were used. These PMTs feature an active area of $25 \times 25\,\mathrm{mm}$, $10\,\mu\mathrm{m}$ pore MCP and a bialkali photocathode for good sensitivity in blue and near UV parts of the spectrum. They also allow for a limited spatial resolution through a matrix of 4×4 anodes gathering charge, although some crosstalk is to be expected. Single photon timing resolution (TTS – Transit Time Spread) is typically $< 35\,\mathrm{ps}$. The typical parameters of these photomultipliers are summarized in Table 3.1.

Window	Synthetic Fused Silica
Photocathode	Bialkali
MCP structure	2 layer chevron, $10\,\mu\mathrm{m}$ pores, 60:1 L:D ratio
Anode structure	4×4 matrix, $5.8/6.4\,\mathrm{mm}$ size/pitch
Active area	$25 \times 25\,\mathrm{mm}$
Package dimensions	$32 \times 32 \times 24\,\mathrm{mm}$
Spectral range	$200 - 650\,\mathrm{nm}$
Peak quantum efficiency (380 nm)	18 % min, 22 % typical
Spatial uniformity	$2:1$ max, $< 1.5:1$ typical
Rise time	0.5 ns
Pulse width	0.7 ns
Transit Time Spread	50 ps max, < 35 ps typical
Maximum magnetic field operation	2 T

Table 3.1: Parameters of the Photonis miniPLANACON XPM85112 MCP-PMT as given in its datasheet [24].

3.4.2 Gain curve

A gain curve is a relation between the supplied high voltage bias and the multiplication factor of the MCP (how many electrons it produces from a single hit). As the bias voltage increases, the multiplication factor rises as well. A typical gain curve given by the manufacturer in a datasheet for the MCP-PMT used in AFP-ToF is in Figure 3.14.

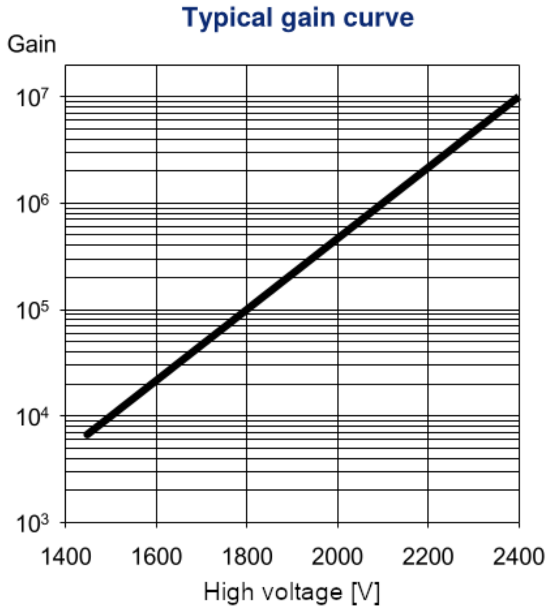

Figure 3.14: A typical gain curve as supplied in the datasheet for a Photonis mini-PLANACON XPM85112 MCP-PMT [24].

Individual MCP-PMT pieces will vary somewhat due to the manufacturing process variability. A specification of the voltage required is supplied on the manufacturer's test protocol for multiple gain values (usually 10^5 and 10^6) for each particular PMT piece, together with values of dark current at those gain points and the precise MCP internal resistance for that PMT piece. Depending on the application (especially light levels), the required supply voltage for the desired gain is selected. In the case of AFP-ToF, a gain of $10^4 - 10^5$ is targeted, while the actual values are then refined during a beam test campaign in order to achieve an optimal performance of the ToF system.

3.4.3 High voltage divider

The job of a high voltage (HV) divider is to prepare the multiple necessary voltage levels for the PMT. Compared to the classic PMT tubes with many distinct dynodes, MCP-PMTs require only few levels – cathode bias, MCP input bias, MCP output bias and ground. The bias is negative and highest at the photocathode (for example around 1800 V for 10^5 gain), ensuring the photoelectrons are extracted by the field and accelerated towards the MCP input by roughly a 150 V potential. The MCP is biased by about a 1500 V potential, facilitating the multiplication by accelerating the electrons inside a pore. Finally, the MCP output is again at roughly 150 V against the ground, attracting the electrons towards the anode pads. The anodes are connected to ground through a load connected at the PMT signal outputs, typically a load resistor serving as a current to voltage converter for a preamplifier. The PMT must not be used without any load or short to ground on the signal outputs as it could cause excessive accumulation of charge on the anodes.

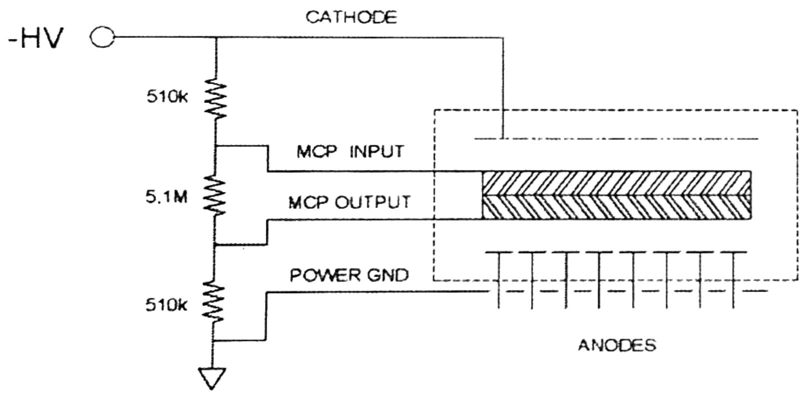

Figure 3.15: The recommended HV divider supply scheme as depicted in a test protocol for each of the Photonis miniPLANACON XPM85112 MCP-PMT pieces. This exact divider setup was adopted as the AFP-ToF baseline.

The reference implementation of a HV divider is in Figure 3.15. The divider supplies a cascade of voltage levels at the ratio of 1:10:1. Of course the divider ratio is not perfectly translated into the real voltage levels as the MCP internal resistance (tens of MΩ) is connected in parallel with the MCP bias divider resistance, influencing slightly both the resulting ratio and the total divider resistance. The test protocol provided with each PMT piece however takes these effects into account as long as the precise recommended divider is used – not only the ratio, but the resistor values as well. That recommended HV divider setup was adopted for AFP-ToF, therefore the manufacturer's test protocol values for HV vs gain can be used as a baseline before further HV level tuning.

The fixed ratio of the supplied HV division also means that as the supplied voltage changes, not only the MCP supply is changed, but the front and back stage voltages as well vary. Under the standard operational conditions, these changes are not of any great concern.

3.4.4 Detection efficiency

Detection efficiency is simply the ratio of number of photons reaching the PMT and how many of them are actually detected by the device. It can be split into two distinct components – the quantum efficiency and the collection efficiency. The relation between these is in Equation 3.1, where λ is the incident photon wavelength.

$$\underbrace{\mathrm{DE}(\lambda)}_{\text{detection efficency}} = \underbrace{\mathrm{QE}(\lambda)}_{\text{quantum efficency}} \cdot \underbrace{\mathrm{CE}}_{\text{collection efficency}} \tag{3.1}$$

Quantum efficiency

Quantum efficiency (QE) is the ratio of how many of the photons reaching the PMT succeed in kicking out a photoelectron when they impact the photocathode. These photoelectrons are then extracted by the front stage bias (voltage applied between the photocathode and the MCP front face). By its nature, QE is very wavelength dependant. A typical spectral response of the photocathode provided by the manufacturer in a datasheet for the MCP-PMT used in AFP-ToF is in Figure 3.16.

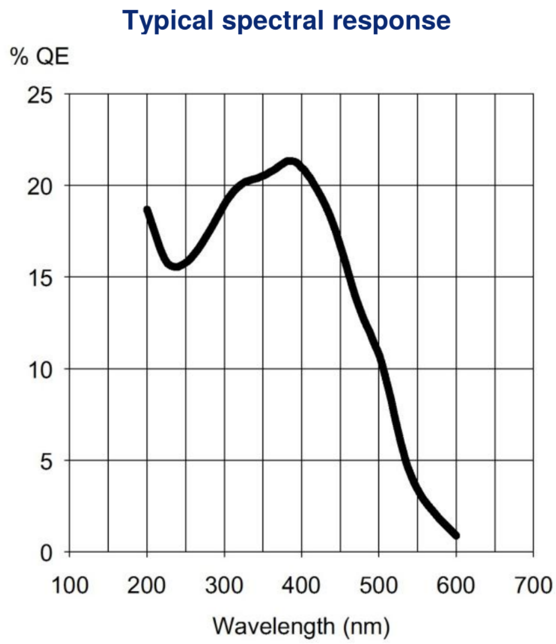

Figure 3.16: A typical quantum efficiency as supplied in the datasheet for a Photonis miniPLANACON XPM85112 MCP-PMT [24]. The included Bialkali photocathode is clearly optimized for shorter wavelengths, which is exactly what the AFP-ToF system requires.

Quatum efficiency (QE) of the PMT is given by the photocathode type and cannot be easily further optimized, as the photocathode in use (Bialkali) is the most optimal variant for applications involving blue and near UV light. However, other aspects of ToF development can take advantage of a known QE curve. One such example would be the attempt to remove the need for the epoxy glue in the L-joint of the ToF bars. Based on Figure 3.5 in the section related to the ToF bars, having deeper UV, which is both more prevalent in Cherenkov and well accepted by PMT, would significantly improve the signal strength. This upgrade was eventually implemented, as described in the development chapter in section 4.5.

The fact that a photon passes the QE and successfully produces a photoelectron that is extracted from the photocathode does not guarantee that it will be detected – it also needs to pass through the collection efficiency probability.

Collection efficiency

Collection efficiency (CE) is the probability that a photoelectron produced in the photocathode will start a cascade in the multiplication element(s), in our case the MCP chevron. As the photoelectron is already generated and its energy comes from the bias pulling it from the photocathode, CE does not depend on the original photon wavelength.

CE is most impacted by the simple geometry of the MCP pores. As shown in Figure 3.17 and corresponding to the specification of the device, the pore coverage on the MCP front face is 60 %. The relation of pore coverage to CE is not perfect – some photoelectrons missing a pore might bounce and be accepted later, while some entering a pore might fail to produce secondaries inside the pore. Still, the resulting collection efficiency is $\sim 60\,\%$.

Figure 3.17: An MCP plate inside an MCP-PMT as seen by an Olympus OLS LEXT 5000 confocal microscope looking through the front PMT window. The $6.5\,\mu$m pores with coverage of $60\,\%$ are clearly visible (this is a different generation of the MCP-PMT device than initially used by AFP-ToF). A few small defects stand out (dark spots) as well as the edges of the hexagonal macroscopic tiling structure, a likely artefact of the manufacturing process.

3.4.5 Signal shape

The MCP-PMT signal shape has a very fast rise time of only a few hundred picoseconds, enabling the very fast timing performance the AFP-ToF system is meant to provide. The rise time may be as low as 150 ps when not processed by the amplification stages, as seen in Figure 3.18. The steeper the edge is, the less opportunity there is for any noise to smear the measurable arrival time. An example of the pulse shape is in Figure 3.19. The pulse width for the Photonis miniPLANACON MCP-PMTs (defined as FWHM, Full Width at Half Maximum) is below 1 ns.

3.4.6 Timing resolution: Transit Time Spread

Transit Time Spread (TTS) is a fundamental measure of the timing performance of any photodetector. It is obtained by measuring the timing resolution when detecting only single photons. A true single photon pulse is hard to obtain, so the typical approach is to filter down a beam from a short pulse laser to a level when only about $5\,\%$ of the laser pulses actually deliver a photon that the device detects. This way, only a very small fraction of pulses (roughly again $5\,\%$) contain two or more photons accepted by the photodetector. As previously shown in Table 3.1, the expected TTS of the Photonis miniPLANACON XPM85112 MCP-PMT is < 50 ps, but typically < 35 ps. We of course aim to obtain the best performing ones possible. The typical TTS of the

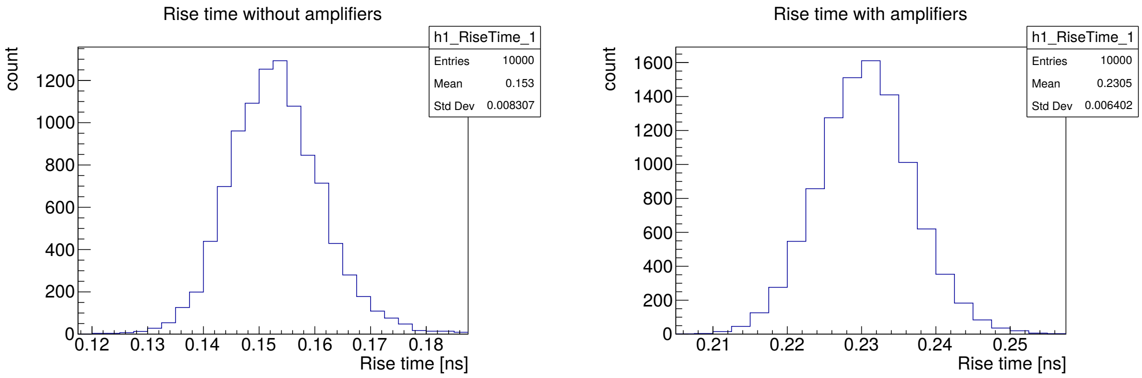

(a) **(b)**

Figure 3.18: Histograms of the $20-80\,\%$ rise time of a PMT pulse when the signal is unprocessed (a) and processed by amplifiers (b).

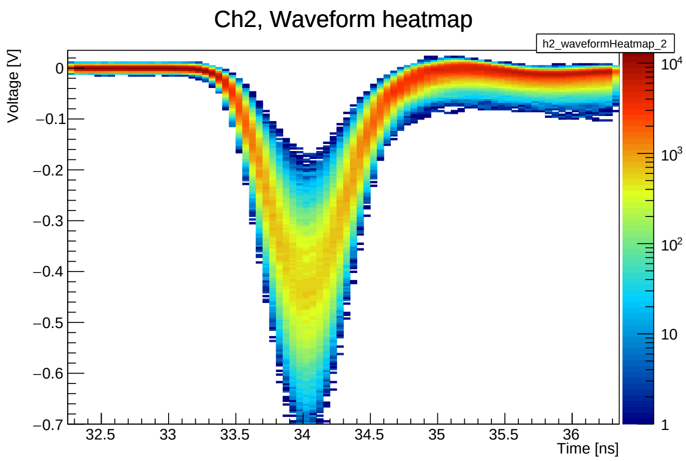

Figure 3.19: A heatmap of the PMT waveforms when hit by a short laser pulse, collected from 15000 waveforms, showing the typical pulse shape. The readout of the oscilloscope was triggered by the laser sync out signal. The rise time of an unamplified PMT pulse can be as low as 150 ps, but the amplifiers smear it to $200-300$ ps, as is the case here.

PMTs used by AFP-ToF is therefore $30 - 35$ ps. An example of a TTS measurement result is in Figure 3.20.

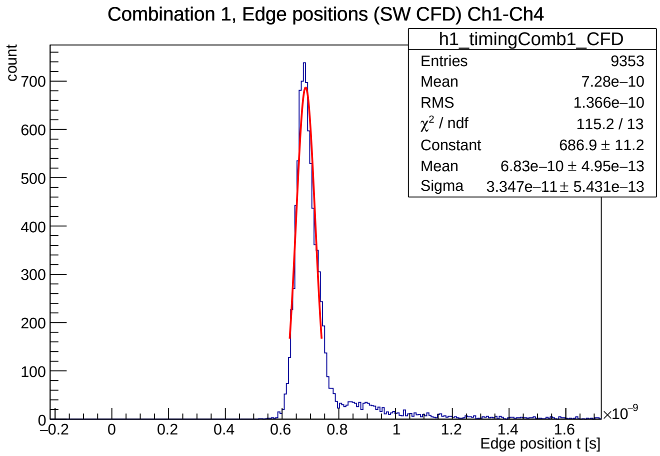

Figure 3.20: A Transit Time Spread measurement, a timing performance measurement when detecting single photons. After subtracting contribution of the laser pulse length, the result of this particular measurement is 29.0 ps with the typical uncertainty of ± 0.5 ps.

When single photon events are detected, certain phenomena emerge that ore otherwise hidden when the light pulses are stronger. One of these is the effect of photoelectrons extracted from the photocathode that miss the MCP pores, but instead of being absorbed bounce off the MCP front side. These then can be accepted by a pore at a later time when they are attracted back by the bias voltage. This results in a pulse that is delayed by hundreds of picoseconds. These pulses are visible in Figure 3.20 as a small secondary peak with a later arrival time. That is one of the reasons why a Gaussian fit of the main peak is used to extract the TTS value, as a simple histogram RMS is too influenced by the bouncers and other outliers.

In scenarios with many photons, this bouncer feature in the timing histogram disappears simply because the typical photons are way more numerous and also arrive earlier than the bouncers, not enabling the occasional bouncer to make a mark the way they do when they are alone during TTS measurements. When the number of photons increases to n, the timing resolution should theoretically improve by the factor of $1/\sqrt{n}$. In reality, the interaction of combining the waveforms and detecting the edge is more complex and this theoretical limit of combining two fully uncorrelated measurements does not apply. The timing resolution is still however significantly improved. The resulting timing resolution under realistic conditions will be explored in chapter 4.

3.5 Signal transmission and processing

The signal produced by the PMT is very weak and unless the PMT gain is set very high, gets typically lost in noise. Therefore we need to properly process it by amplification and filtering, but also set a minimum threshold for passing through and convert the pulse shape to a fast edge suitable for the readout electronics, in order to prevent parasitic effects of variable pulse amplitude on the timing performance. A diagram of the signal processing chain is in Figure 3.21.

Signal processing modules from PAb up to HPTDC use the the NIM (Nuclear Instrumentation Module) standard form factor [25]. This standard defines the NIM crate container that houses and provides power for the individual NIM modules through connectors at the back and is widely used in particle physics instrumentation.

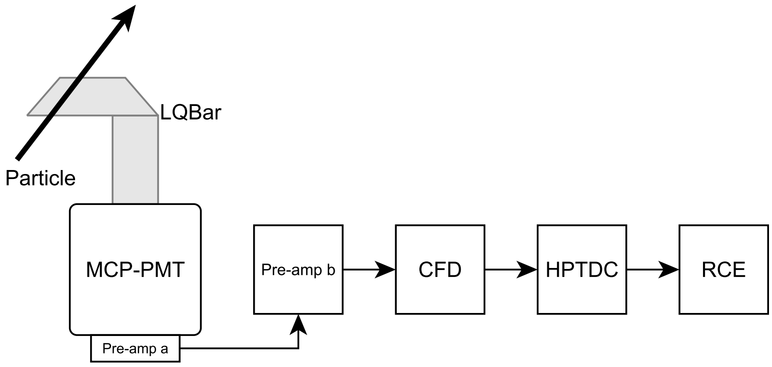

Figure 3.21: Scheme of the signal processing chain. The electric signal created by the PMT is amplified by two stages of amplifiers and further processed by a Constant Fraction Discriminator. The processed signal is then suitable for the Time-to-Digital Converter which feeds data into the readout system. Details about the respective modules are in the following subsections.

3.5.1 Amplifiers

The current pulse from the PMT is very weak and unless very high gain is used, can be impossible to detect among the unavoidable noise on any typical oscilloscope input. Even with high PMT gain, the signal to noise ratio would be poor, especially when timing measurements are involved. That is why a PMT signal needs to be further amplified in most applications.

AFP-ToF in the original design utilized two broadband amplification stages with GaAs (gallium arsenide) semiconductor as the amplification element. GaAs semiconductors have a more favourable characteristics at high frequencies that silicon semiconductors and are also more radiation resistant, an important consideration for high energy particle experiments.

Both stages of amplification are inverting amplifiers, resulting in an unchanged negative pulse polarity at the output of the second stage. The input and output impedances are matched to 50 Ω for signal transmission between modules, however the input impedance of the first stage is more complicated. The input impedance of the amplifier element itself is again 50 Ω, but there is a load resistor in parallel with it (50 Ω) acting as a current to voltage converter. Furthermore, there is a 20 Ω coupling resistor in series at the current input for oscillation suppression.

PAa

PAa is the first stage amplifier processing the PMT signal. The GaAs MMIC amplifier PSA5043 is used as the active element with a frequency range of 40 MHz to 4 GHz. At 5 V supply bias, it has a 16.5 dB gain, or a 6.7 factor of amplitude increase.

The first stage amplifiers are best placed as close to the signal source (PMT) as possible, limiting the length of cable where noise can distort the yet unamplified weak signal. For this reason, they are mounted directly on the PMT back side inside the Roman Pot, implemented as four-channel mini PCBs. Pairs of these PCBs are attached back to back, forming small 8 channel modules. Two of these modules are needed to process all the 16 PMT channels. To mitigate the need for a dedicated power line, each PAa channel is individually powered by a 5 V bias on the signal output line. The PCBs also include a thermistor for monitoring the temperature. The PAa PCB is in Figure 3.22a.

The fact that the PAa modules are placed inside the pot (in the secondary vacuum) also implies a special cooling solution is needed. This is achieved through a copper slab sandwiched between the PAa board pairs, affixed to a special part of the holder assembly to conduct the heat away towards the RP flange. This mechanical fixation is also a way to secure the PAa modules in place as the pin header on the PMT back features no locking mechanism. Without the PAa modules being secured, they might slip off the pin header during flange handling or due to vibrations, jeopardizing the connection quality or even causing loss of signal. Thermally conductive pads are placed between the copper cooling slab and the holder assembly to ensure electrical isolation while allowing the heat to dissipate easily. This can be seen in Figure 3.22b.

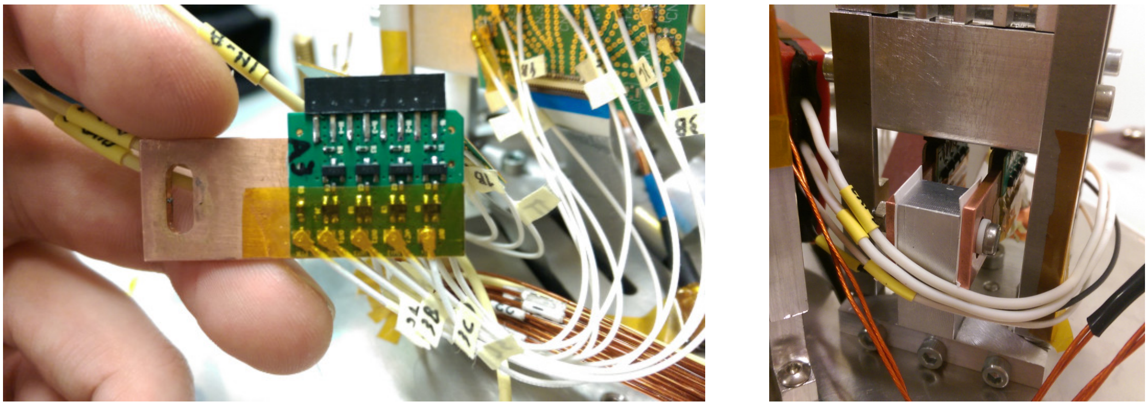

(a) **(b)**

Figure 3.22: The PAa integrated board pair (a) with its wiring connected and the way these were mounted on the ToF holder (b). The copper slab conducts heat away to the Roman Pot flange while being electrically isolated from it.

PAb

PAa is the second stage amplifier of the PMT signal. The GaAs amplifier ADL5611 is used as the active element with a frequency range of 30 MHz to 6 GHz. This is a wider range than in case of PAa, however as a second amplifier it sets the limit on the maximum signal amplitude before saturation effects set in. Based on tests of the AFP-ToF setup, saturation starts to significantly influence the signal at 1.8 V. Effects of this saturation are explored in more detail in section 4.9. The PAb has a 19 dB gain, resulting in amplitude increase by a factor of 9.

PAb channels are grouped by eight into a unified NIM module enclosure which provides shielding and power connection to the NIM crate. Again, two of these modules are needed to handle all 16 PMT channels. The NIM modules can be seen in the fully populated crate in Figure 3.32 in subsection 3.5.6.

The PAb modules have a 5 V bias on the signal input side, providing power to PAa channels. In case we need to amplify another signal source with the PAb, such as a SiPM on a beam test, a simple capacitor can be used on the signal line to isolate the bias while letting the signal through.

3.5.2 CFD

CFD working principle

A Constant Fraction Discriminator (CFD) is a critical signal processing technique for any fast timing system dealing with signals of variable amplitude. It's goal is to mitigate the "time walk" incurred by triggering on a set amplitude threshold. Time walk is a timing smearing caused by the fact that while the signal shape may not be changing significantly (rise time histogram has a narrow range), the amplitude significantly differs in individual detection events, shifting the trigger point of a fixed threshold trigger. A CFD circuit processes the signal in a more complex way to trigger on peak height fraction instead while producing a sharp edge on its output. The time walk effect is illustrated in Figure 3.23.

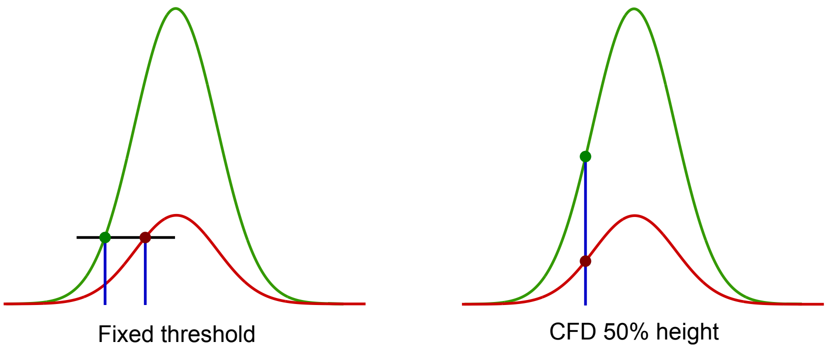

Figure 3.23: Illustration of the time walk effect when triggering on a fixed threshold (left) and how a CFD handles the same situation (right). A fixed threshold triggers sooner for higher amplitude signals while the CFD mitigates this effect by triggering at a peak height fraction.

The CFD logic of triggering on peak height fraction is straightforward to implement in software when working with sampled signals. An example of such implementation is in Appendix A, this particular implementation was widely used in the raw oscilloscope data analyses described in this work.

A hardware CFD circuit however has to work with an approximation of the CFD principle and needs to be tuned for a particular signal shape. A CFD circuit is usually implemented through splitting the signal, running one branch through an attenuator and the other through a delay line. These signals are then compared, effectively triggering when the delayed signal rises over the attenuated one. The working principle of a hardware CFD is illustrated in Figure 3.24.

A standard fixed threshold discriminator is also included in the CFD circuitry to compare the original signal to a threshold value. This is then paired with the CFD logic output by a single AND gate – a CFD without a threshold function would be constantly triggering on noise. The threshold discriminator has to trigger sooner than the one implementing the CFD logic in order to serve as a qualifying condition without injecting the time walk it suffers itself. A scheme of such hardware CFD is in Figure 3.25.

A well tuned hardware CFD has the delay set to a value that ensures the delayed signal rising edge crosses the attenuated signal's plateau around the peak, as is illus-

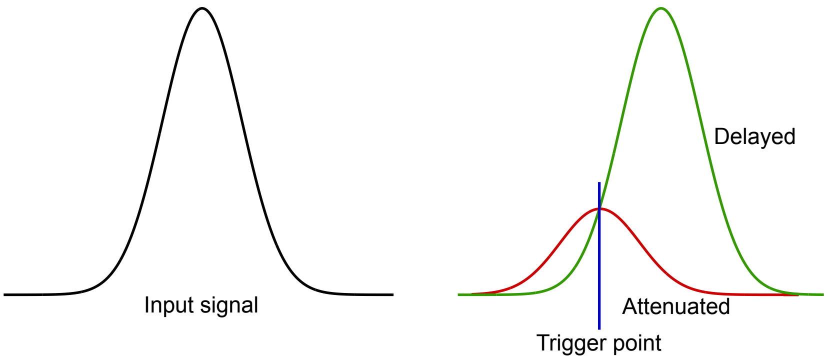

Figure 3.24: Illustration of the hardware CFD working principle of comparing attenuated and delayed signal branches.

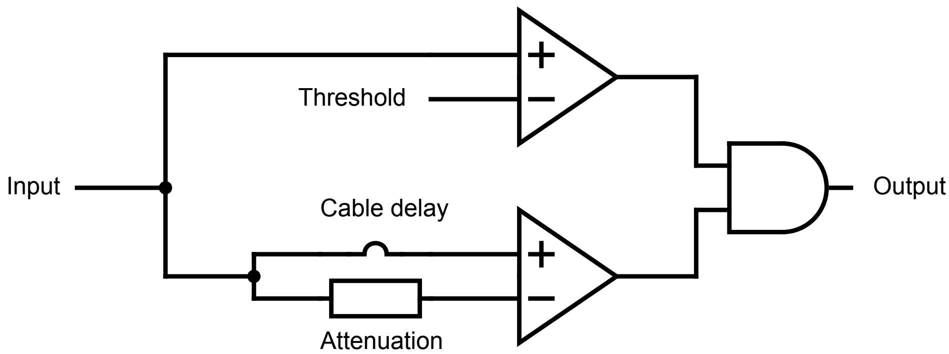

Figure 3.25: A block diagram of a typical CFD circuit for triggering on positive peaks. The bottom branch with delay and attenuation implements the actual CFD logic of trigger on peak fraction while the top branch is a simple threshold discriminator. Both are fed to an AND gate, making sure the CFD implements the principle in Figure 3.24, but also only triggers above a certain threshold, rejecting noise.

trated in Figure 3.24. This delay setup then means the attenuation value is effectively the CFD fraction value. It also means a CFD circuit has to be tuned for signals of a particular rise time and will not work well if the rise time significantly differs.

Furthermore, the attenuation fraction should be set to the height of the steepest part of the rising edge, which might not always be a simple 50 % height, although 50 % may serve as a sensible default if unsure. A proper trigger fraction selection minimizes the time jitter due to noise by ensuring the steepest possible difference of the two signals around the trigger point. A well tuned delay then makes sure there is a minimal variation of the effective trigger fraction (which might be caused by small signal shape variations if the crossing of the two signal paths was not near the plateau at the peak). A CFD implemented in software can avoid the delay completely and is therefore more universal, but benefits from the trigger fraction tuning in the same way.

CFD modules for AFP-ToF

The CFDs used for AFP expect negative peaks, as the two inverting stages of amplification (PAa+PAb) maintain the original negative signal polarity the PMT produces. Trimmers exposed on the individual CFD boards allow for tuning of the delay and threshold values. The delay is set once to provide the best performance with the typical PMT signal shape while the threshold is expected to be varied under different experimental conditions. For this reason, a remote control of the CFD thresholds is implemented via I^2C communication. Whether the remote or local (trimmer) control is used is determined by a position of a jumper. The attenuation value is fixed at 0.42 as that is where the typical PMT signal has the steepest edge. The CFD modules can be seen in Figure 3.26.

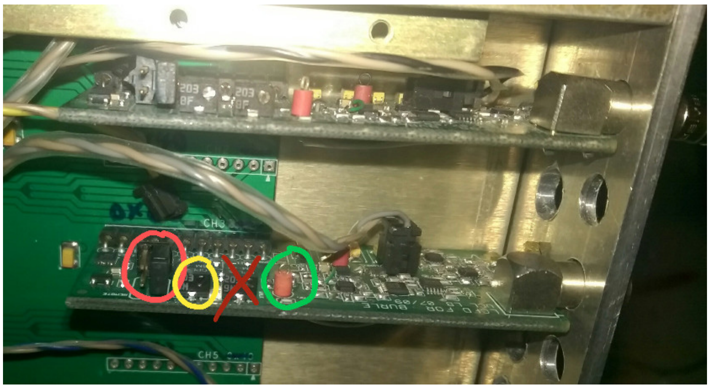

Figure 3.26: Two AFP-ToF CFD daughter boards in a NIM module container with its side cover removed. A fully populated NIM module contains 8 of these, each processing a separate ToF channel. The control elements are marked on the lower board: light red is the remote/local jumper; yellow is the threshold trimmer; red cross is the walk (delay) trimmer; green is a probe point for the threshold tuning.

The CFD modules have two outputs, LVPECL for the TDC and Lemo for other purposes, like probing with oscilloscope or triggering other equipment while testing. The Lemo output signal is a fast edge with amplitude of 450 mV and a rise time of < 100 ps. The signal shape is in Figure 3.27.

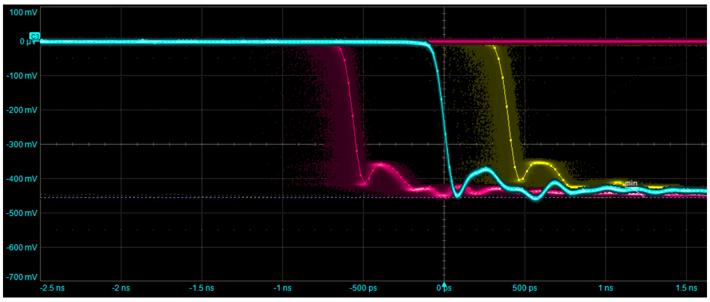

Figure 3.27: CFD signal edges as captured by an oscilloscope. The cyan coloured channel is triggered on, the others undergo smearing due to a variable time of signal arrival on the CFD inputs. The slight signal ringing after the edge is not detrimental, on the contrary – it allows the primary edge itself to be steeper.

3.5.3 HPTDC

High Performance Time-to-Digital Converter (HPTDC) is employed as the digitizer of the timing information. For the purpose of the AFP-ToF system at the LHC, it needs to receive a reference clock signal (estimated to have a 3 ps jitter) in order to synchronize the HPTDC modules on both A and C side.

HPTDC as used for ToF utilizes the "very high resolution mode", where it operates by doing four individual samplings of the Delay Locked Loop signal, with 4 normal TDC channels working together [26]. The loop length is 25 ns (the LHC bunch spacing), looping over 1024 bins. This produces a theoretical bin width of 24.4 ps.

For maximum precision, the HPTDC chips need to be individually calibrated. This calibration is typically done by recording input signal with random timing (in reality, an unsynchronized clock input works well). In the perfect case with sufficient statistics (high event count), the number of events in each of the 1024 bins in the 25 ns loop should be almost the same, with some expected statistical fluctuations. In reality however, these bins are not of the same width, which can be easily seen as highly disproportionate event counts. An example of an uncalibrated HPTDC information is in Figure 3.28. This data in turn allows for calculation of the real bin widths and lets relevant corrections be applied to the timing information. The calibration is somewhat temperature dependent, so for the best results it needs to be performed with properly warmed up HPTDC boards once installed in their intended operational environment.

The HPTDC is configured by loading a config file at the start of a run. This configuration contains information like channel mapping, timing latencies and trigger configuration. It also allows to set the CFD thresholds (each channel individually). This is communicated to the CFD modules by I^2C.

3.5.4 RCE

RCE (Reconfigurable Cluster Elements) system [27] is the data acquisition system used by AFP. It is used in conjunction with the HSIO-II (High Speed Input Output) board, as can be seen in Figure 3.29. The RCE stores data as a ROOT file, allowing straightforward reading and processing using the ROOT data analysis framework.

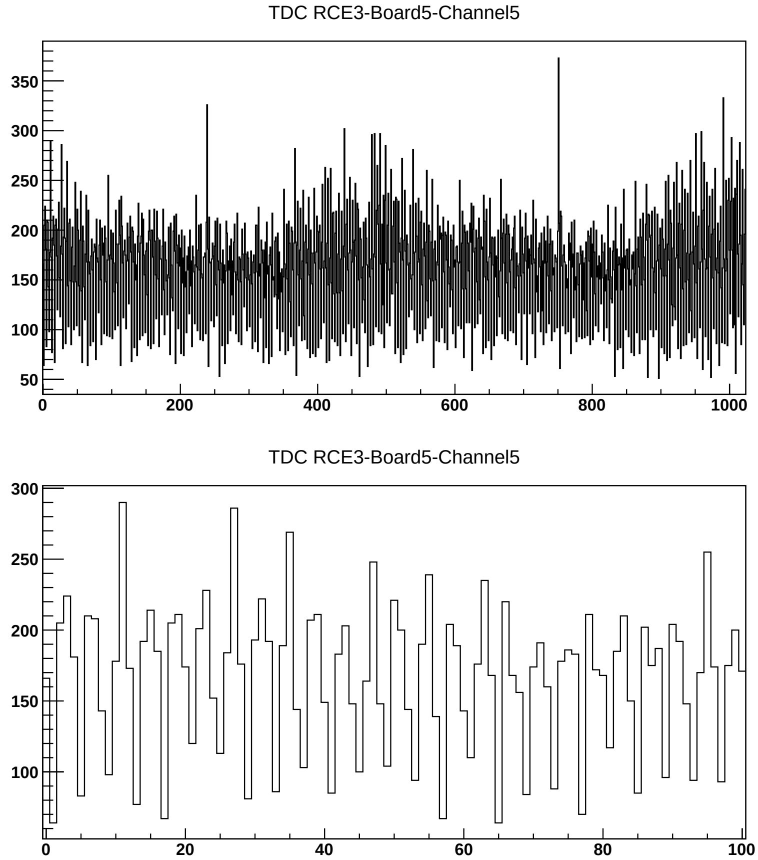

Figure 3.28: Occupancy of timing bins of a single HPTDC channel when fed with with a random timing input (unsynchronized to the clock). In an ideal case, all bins would have roughly the same number of hits, with the necessary statistical fluctuations. In reality, the bin widths are highly non-uniform, so a calibration information about the real bin widths is necessary to achieve a good timing performance. An overview of all the 1024 bins is in the top plot, the bottom plot is a zoom of the first 100 bins. A non-uniformity with a significant periodicity of 4 bins is clearly visible. This is an artefact stemming from the way the very high resolution mode is implemented in the HPTDC, where four channels are used together and their individual samplings are combined into a single interpolated result [26].

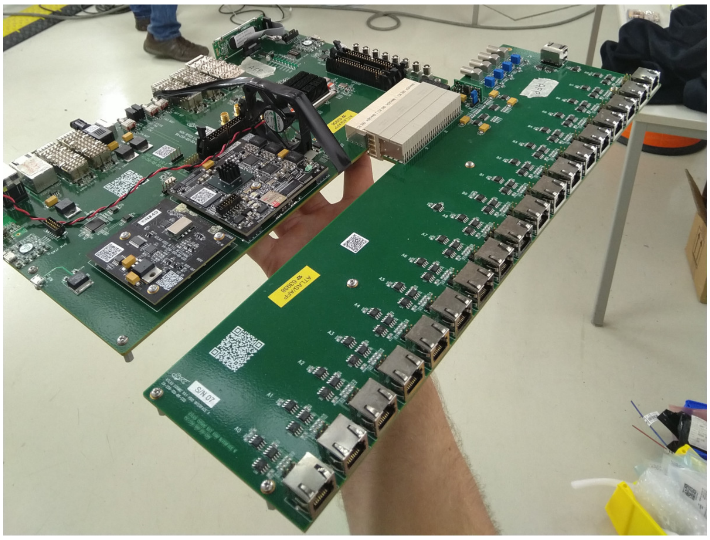

Figure 3.29: The RCE system with HSIO-II attached (bottom right), allowing a common readout of many data stream channels.

3.5.5 Trigger

AFP is expected to provide L1 trigger capability for ATLAS. This is challenging due to the long distance to the Central Trigger Processor (CTP) of ATLAS and limited time window for the L1 trigger delivery.

In 2016, only SiT trigger was available since ToF was not yet installed in the AFP Roman Pots at LHC. Trigger capability was later implemented in HPTDC firmware and tested on beam tests. The trigger source (SiT or ToF) could be selected via a switch box once ToF was added to the system in 2017.

3.5.6 Signal transmission cables and signal path

The objective of the signal transmission cables is quite simple: transfer the signal between the signal processing equipment modules with minimal losses and distortions while also limiting external interference and crosstalk between the individual signal lines.

"Crosstalk" as a term likely originates in old telephone lines, where different calls could sometimes hear each other despite each being carried by a separate line. Twisted pair lines were introduced to limit this effect, but it was only the invention of the coaxial cable that provided a suitable solution for this problem. In coaxial cables the signal line is the core, being completely encased within a hollow ground connection, acting as a shield. These two are separated by a gap, typically filled with a dielectric material.

The impedance of the signal lines has a great influence on the signal behaviour, as was studied in Bell Labs in 1929. The optimum for power transfer is 30 Ω, for maximum voltage 60 Ω and 77 Ω for minimum attenuation, as shown in Figure 3.30.

The available coaxial cables are commonly tuned for 50 Ω impedance, a good compromise between the power transmission capability and the voltage limit. The voltage is what practically limits the power in most applications due to the limits of the dielectric separators, explaining why 50 Ω impedance was chosen as the widespread standard, being closer to the maximum voltage impedance than the peak power capability. 75 Ω cables are also widely used in applications where signal power is lower and loss mini-

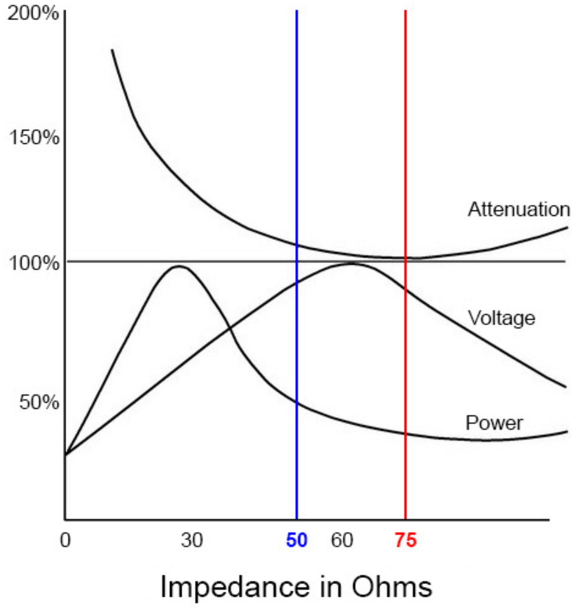

Figure 3.30: Impedance of transmission lines has a great influence on the power and voltage limits as well as signal attenuation, as was shown by Bell Labs in 1929. Image credit: [28].

mization is the primary concern. The value of 75 Ω is used instead of 77 Ω due to ease of manufacturability stemming from the necessary inner and outer conductor diameter ratio.

The impedance of the cable connection needs to be matched to the signal input and output terminals of the signal processing equipment to prevent losses from reflections. Signal reflections due to impedance mismatch could also cause fake delayed triggers in some cases. AFP uses 50 Ω matching as equipment (especially amplifiers) with favourable characteristics and 50 Ω terminal matching is readily available, as described in [5]. We don't need to transmit signal over too long distances, so the extra losses compared to 75 Ω are not of any great concern. Testing equipment like oscilloscopes are also commonly equipped with 50 Ω signal inputs, which is very favourable for the development phase.

Signal path and connectors

The AFP-ToF signal path starts at the pin header of the PMT. It is then amplified by the PAa channels. The PAa modules are mounted directly on the back side of the PMT to ensure the shortest possible signal path before amplification (limiting interference pickup). The amplified signal is transported out of the Roman Pot with flat flex cables, as shown in Figure 3.31. The flex connections lead to the "halfmoon" breakout boards at the back of the flange. The flex cables are a weak point of the design, not being well matched to the 50 Ω impedance of the rest of the signal line. This can result in signal attenuation and pulse reflection. These reflections should however follow shortly after the primary signal and fall in the dead time of the electronics further down the line, not posing any significant issues. Only the attenuation and possible signal shape distortions are of concern, as well as interference pickup.

Further down the signal path, AFP-ToF makes an extensive use of the SMA (Sub-

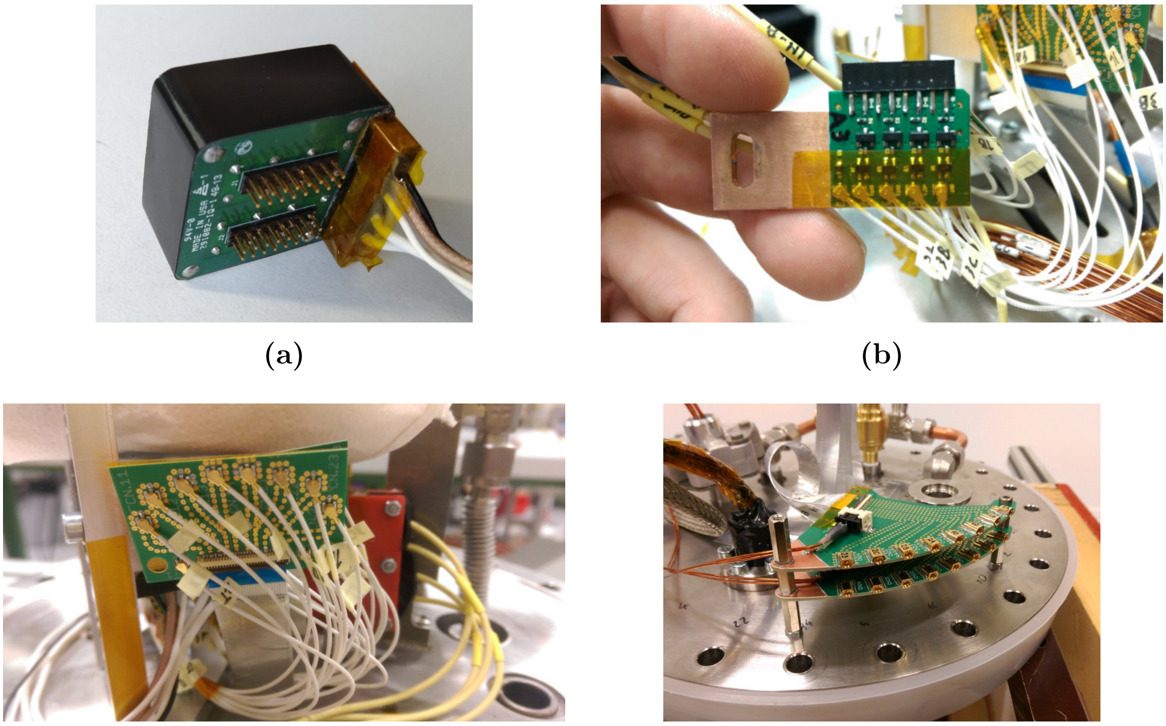

(a) (b) (c) (d)

Figure 3.31: The signal path from the PMT to the PAb. The PMT back exposes the signal lines in the form of pin headers (a) that are populated with two pairs of PAa first stage amplifiers (b). The amplified signal is carried to a pair of interconnection boards with small coaxial cables (c) that connects to two flex cable feed throughs. On the other side of the flange (outside the secondary vacuum) are the "halfmoon" boards, breaking out the flex lines to individual MMCX connectors (d). These then directly lead to the PAb NIM module through individual coaxial cables with SMA connectors at the other end.

Miniature version A) connector type. This includes connection of the MMCX-SMA cables from the halfmoon boards to PAb modules and PAb-CFD connections.

The inferior twisted pair cables are used in AFP for connection from the CFD units to the TDC. These are deemed sufficient for transmission of the digital LVPECL signal with sharp edge and a large 800 mV swing, while allowing for a very compact ribbon cable and connector setup. The CFD modules also feature a parallel Lemo outputs, which are very useful for both signal path testing purposes and non-standard signal routing to trigger other equipment (such as an oscilloscope). The HPTDC modules also feature Lemo outputs that were used for ToF trigger signal.

From HPTDC onwards the signals (except of the trigger output) are digital data streams of encoded timing information, hence not interesting from signal transmission point of view. The DAQ systems are connected to the HPTDC modules with shielded RJ45 patch cables. The fully populated ToF NIM crate can be seen in Figure 3.32.

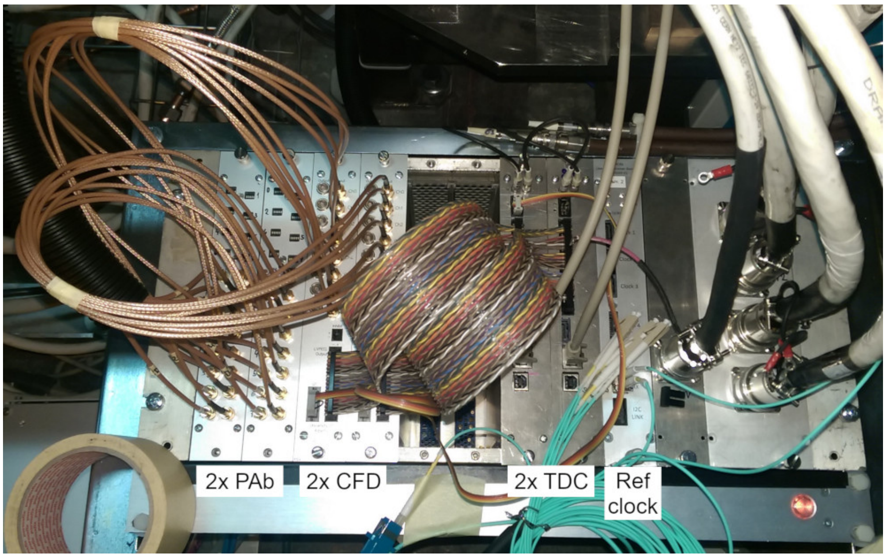

Figure 3.32: A populated NIM crate used for ToF signal processing modules. The PAb, CFD and HPTDC are paired, each processing 8 channels corresponding to two ToF trains. A reference LHC clock signal for the TDCs is provided by the reference clock module.

The trigger signal is carried to CTP from both sides by air-core coaxial cables. The reason for choosing those instead of the widely used optical fibres is due to latency; as AFP is quite far from ATLAS (~ 200 m), every nanosecond counts. Air-core cable transmits the signal faster than the optical signal would travel through the fibre material and it also avoids the conversion delay from electrical to optical signal and back. The downside is pulse shape deterioration, which is not a major concern for a simple trigger signal. As there was no ToF installed in 2016, these could be only used for carrying trigger signal from SiT at the time.

Chapter 4

Development of AFP-ToF

This chapter explores the various ways the AFP-ToF system was modified and upgraded between 2017 – 2023 and the performance evaluations of both the individual parts and the full system.

To say that AFP-ToF underwent an overhaul would be an accurate statement; essentially all the parts, from the Cherenkov bars and the PMT, down to the signal processing chain modules, were significantly modified. Even the mechanics of the ToF mounting solution on the flange were redesigned from ground up. Some new modules providing new capabilities, like the dedicated trigger module or a pulsing light source for testing purposes, were also added.

These modifications are aiming to hit several goals. The first is improved event rate capability, necessary due to the increased luminosity that was planned for the LHC run 3. Another critical requirement is an improved lifetime of the MCP-PMTs in order to survive large integrated charge while not deteriorating their performance in a significant way. A clear target is also to improve timing resolution, a core parameter of the system – this would also help to better cope with the luminosity increase (more numerous and more tightly packed collisions require better timing to achieve the same background suppression). Hand in hand with the timing resolution go targets like suppression of outside interference and internal channel crosstalk. A major point is also the reliability of parts, especially the PMT HV supply being troublesome in the vacuum and the PAa and PAb channels sometimes dying during handling. Lastly, the serviceability of parts needed improvements, especially the PMT and PAa that were enclosed inside the Roman Pot. This was facilitated through changes in design and an improved ease of access to replace them if such need arises.

As was mentioned in the Preamble, the author of this work played an instrumental role in the initial characterization and further development of the ToF system for AFP, performing and evaluating the vast majority of the laser measurements needed, attending all but one of the many beam test campaigns (while over time becoming a critical workforce for their success), and eventually even taking up the responsibility as a beam test coordinator at the AFP project.

4.1 Laboratory tests performed with picosecond and femtosecond laser systems

Two distinct laser systems were used for testing the MCP-PMTs for the AFP-ToF system, each with their share of advantages and shortcomings. As the readout, a LeCroy

WaveMaster 806Zi-B oscilloscope with a 6 GHz bandwidth and a 40 GS/s sampling rate was typically used.

4.1.1 Ti:Sapphire laser

The Ti:Sa laser was used initially for timing resolution (TTS) tests, benefiting from its extraordinarily short pulses.

The laser itself is pumped by a green laser and produces near infrared light at 840 nm. This light is then processed by a sequence of non-linear crystals to multiply the frequency to the second and third harmonic wavelengths of 420 nm and 280 nm. The third harmonic is then separated using a dichroic mirror. The laser can operate in two modes, resulting in 50 kHz or 50 MHz pulse rates. The pulse length is only a few hundreds of femtoseconds, orders of magnitude below the timing resolution we aim to measure.

The Ti:Sa laser setup (as shown in Figure 4.1) is unfortunately very complex and sensitive, resulting in frequent need of tuning to maintain the beam. This also means the beam intensity is not stable enough to perform some other measurements, like determining the gain curve. The pulse rate limitations then do not allow proper measurement of the rate capability of the PMT. Furthermore, for timing measurements we have to rely on an external trigger source, such as a SiPM (silicon photomultiplier) [29] triggering off the split beam, further complicating the setup.

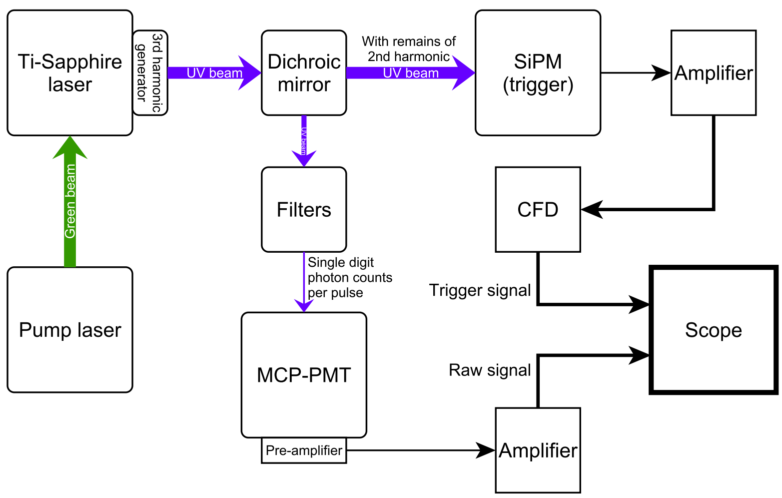

Figure 4.1: Laser setup using the Titan:Sapphire laser.

4.1.2 Diode laser

During AFP-ToF development, it became clear that the Ti:Sa laser's many shortcomings were a hindrance in performing the PMT tests effectively and did not feasibly allow for many parameters to be probed at all. As a result, the Hamamatsu C10196 diode laser system (depicted in Figure 4.2) was purchased.

The diode laser provides pulse rates in the range of 2 Hz – 100 MHz using internal trigger and also allows for operation with an external trigger source. Once the laser head temperature is stabilised, the laser light produced is also exceptionally sta-

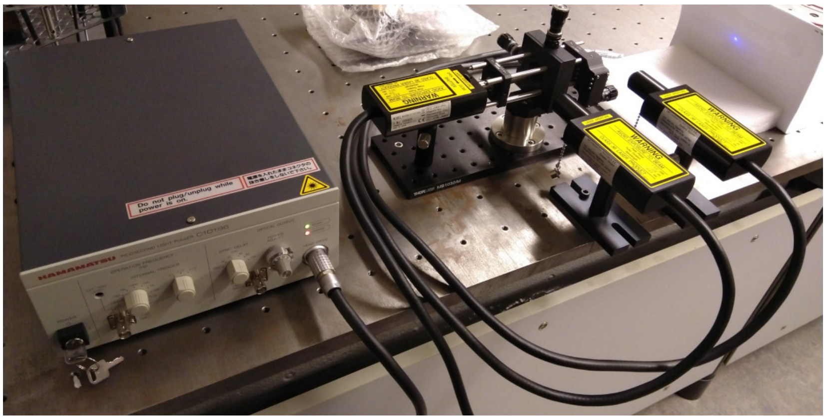

Figure 4.2: The Hamamatsu C10196 picosecond light pulser system. The laser driver unit is on the left with three laser heads on the right, in our case allowing to select the wavelengths of 402 nm, 421 nm or 443 nm. The pulse length is 50 − 60 ps.

ble. Additional advantages are short setup and stabilisation time, simple switching of wavelengths by swapping of laser heads and a much more compact footprint.

The laser driver also provides a very useful trigger output with low jitter, experimentally confirmed to be no worse than 6 ps, a level that could be considered negligible when the PMT TTS is > 30 ps. This was tested by letting strong pulses with thousands of photons hit the PMT operating at very low gain, reaching the resolution of 6 ps. The trigger jitter therefore cannot be worse than that.

Overall, the only downside of the diode laser system is the longer pulse length. Since the pulse is known to be of roughly a square nature and of a known duration, its effect on timing is well defined and can be subtracted. RMS of a 58 ps long square pulse is 17 ps, well below the typical TTS timing resolution of 30 − 35 ps. Therefore the subtraction does not introduce significant uncertainty of the result. Even with the shortcoming of longer pulses, this system is suitable for the timing measurements of the ToF MCP-PMTs. In case the pulses are not in reality perfectly square, the measurement result will be simply slightly pessimistic, which is fine for our purpose (where the opposite, overly optimistic results, would not be that useful).

4.1.3 PMT channel masking

For the purpose of simulating the AFP-ToF signal with a laser, a mask mimicking the ToF bar size and layout on the PMT face was designed and 3D printed. It facilitates individual channel plugs, ensuring maximum flexibility of the illuminated channels layout. To ensure uniform light coverage, the beam was expanded using an adjustable focus collimator to cover the entire PMT active area. The mask was used ranging from a single channel, a train or a full PMT exposure. In cases where simulation of the bar footprint and the related charge sharing inside the PMT was not desirable, a simple optical fibre with a small fixed collimator was used to cover only a small area with a ~ 2 mm diameter in the center of the desired channel.

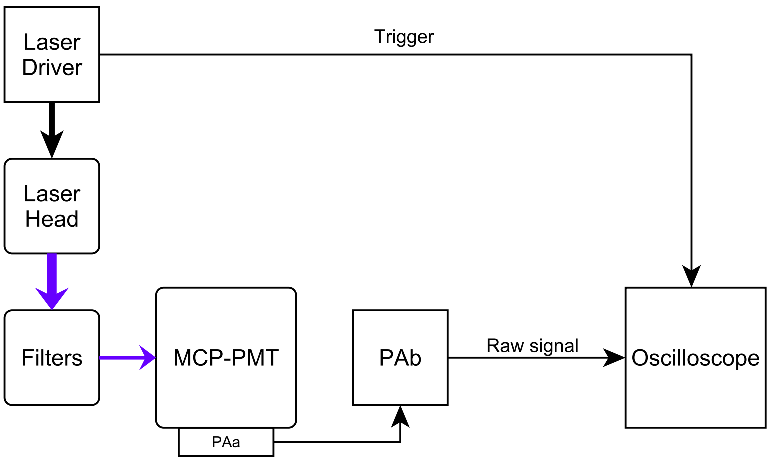

Figure 4.3: Laser setup using the Hamamatsu C10196 diode laser system. This setup allows to freely tune the repetition rate which allows for detailed measurement of rate capability of the PMTs.

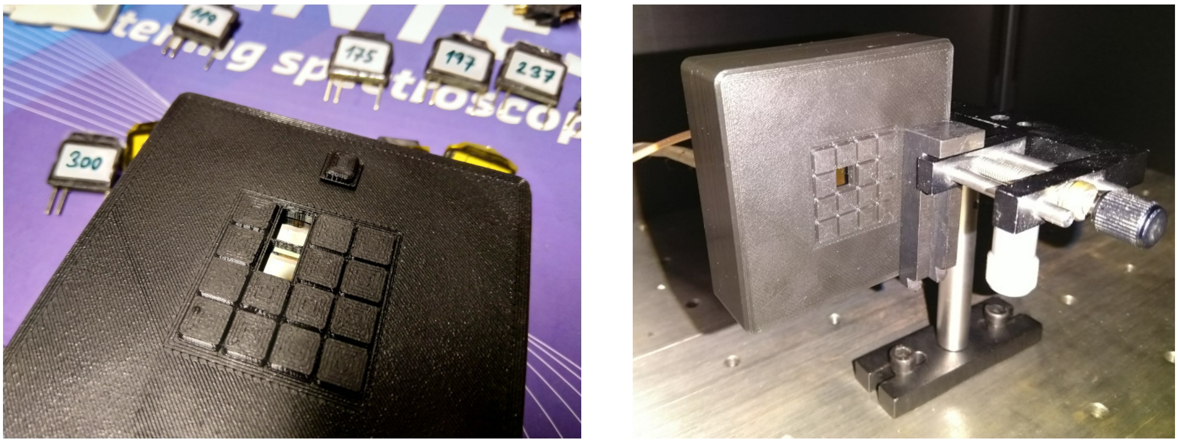

Figure 4.4: The 3D printed mask, a detail with a channel plug shown and in a mounted position during measurements of a single channel illumination scenario.

4.2 Beam Test campaigns and performance evaluation

A critical part of the AFP-ToF development cycle were beam tests, where the system was tested with an accelerator beam realistically simulating the conditions at the LHC (except high rates). In the period of 2016 – 2023, the dissertation author has attended a total of 14 beam test campaigns while taking on the responsibility of coordinating preparation and execution of 8 of them. This section contains a description of how these tests were performed. A photo of the typical AFP beam test setup is in Figure 4.5.

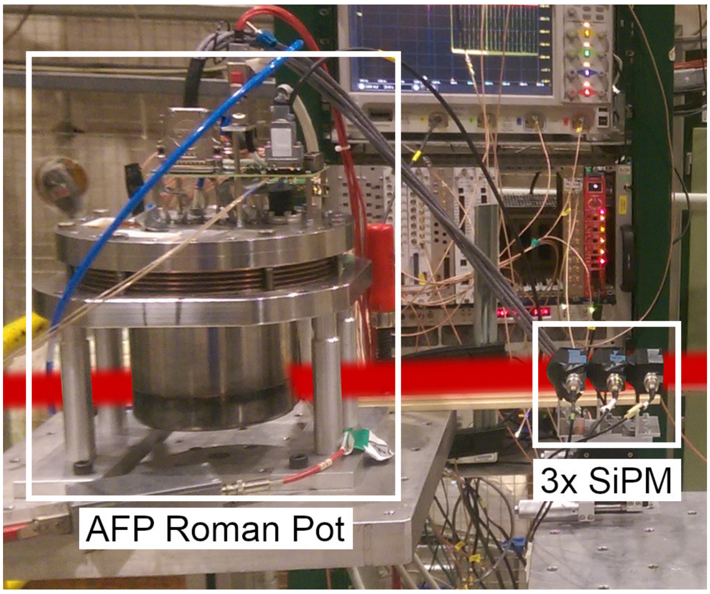

Figure 4.5: A test beam setup with the AFP Roman Pot (containing SiT and ToF) and the SiPM reference timing detectors marked in the foreground. The beam, coming from the left side, is artificially marked in red. In the background is visible a rack with an oscilloscope and a crate with the signal processing modules as well as a remotely controlled HV supply for the ToF PMT.

The ToF setup was typically tested on beam tests in two distinct configurations – recording the raw ToF PMT waveforms or with the full signal processing and readout chain.

4.2.1 Readout of raw signal using oscilloscope

The first setup configuration is a much simpler variant, observing the raw PMT signal. The signal is amplified, but not processed further. Instead it is fed into an oscilloscope to record the waveforms as shown in Figure 4.6. A SiPM (Silicon Photomultiplier) detector is used as a trigger and a timing reference. More details about the SiPM are in subsection 4.2.3.

This configuration is very useful for evaluation of the ToF bars, PMT and amplifier performance under varying conditions. In particular, the PMT high voltage supply can be tuned to an optimal level and an updated variant of the bars, amplifiers, HV dividers or the feedthrough/cabling solution can be easily compared to the predecessors. Observing the raw signal directly lets us also judge any impact on the rise time or signal to noise ratio. Finally, the ultimate timing resolution potential of the system can be determined, an important information for the future when a better performing TDC would be introduced.

As the PMT signal has a very fast edge of only a few hundreds of picoseconds, the oscilloscope must have at the bare minimum 1 GHz bandwidth to perform reasonably well. For the important timing studies, a LeCroy WaveMaster 806Zi-B with a 6 GHz bandwidth and a 40 GS/s sampling rate or an Agilent/Keysight DSO9254A with a 2.5 GHz bandwidth and a 20 GS/s were used.

For determining the timing resolution from raw waveforms, a software CFD implementation was developed (Appendix A). This implementation was validated against the HW CFD circuits and was shown to perform within 1 ps of the HW CFD reference at a beam test.

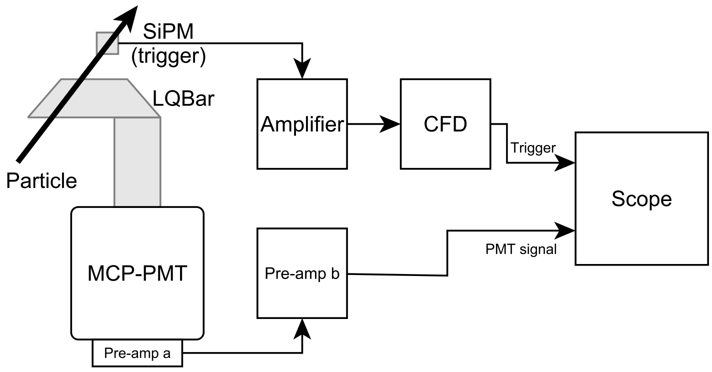

Figure 4.6: ToF setup block scheme on the beam test, variant with oscilloscope readout.

4.2.2 Full chain with HPTDC and RCE

The second configuration is closely aligned with the full processing and readout chain intended for use at the LHC, utilizing the HPTDC for digitization of the timing information and RCE for a combined readout of both the ToF and SiT subsystems. A scheme of this configuration is shown in Figure 4.7. The presence of SiT allows for cleaning up the data for clear tracks and spatially correlating them with ToF hits. The SiPM is present as well, again acting as a timing reference, allowing the determination of the timing resolution with almost all the factors included (the only exception being the LHC reference clock, impact of which should be negligible).

4.2.3 SiPM reference timing

A set of three SiPM (Silicon PhotoMultiplier) devices were placed downstream of the ToF detector as a part of the experimental setup, as seen in Figure 4.5. Each SiPM is in a nutshell an array of many avalanche photodiodes, arranged into a square acting as individual pixels. The SiPM detectors are therefore proportional (unless saturated) as multiple photons are unlikely to hit the same pixel.

The SiPM devices typically have a good timing resolution. The light source was a Cherenkov radiator bar (same material as ToF) of $3 \times 3 \times 30\,\mathrm{mm}^3$ dimensions, aligned with the beam direction, thus capturing the Cherenkov photons via internal reflection. Optical grease was applied between the bar end and the SiPM active area to prevent

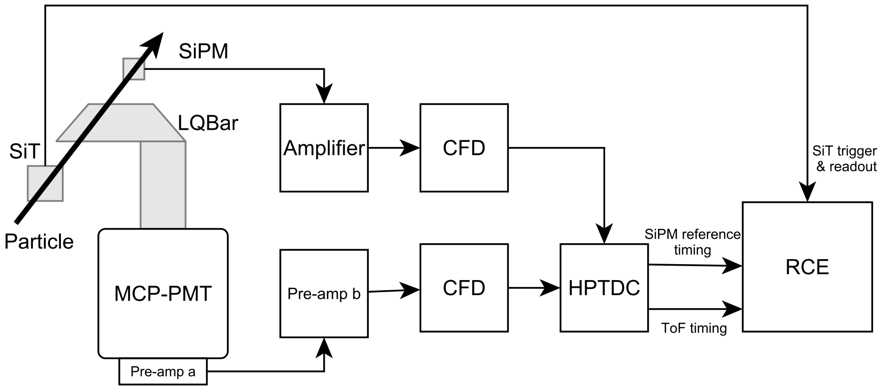

Figure 4.7: ToF setup block scheme on the beam test, variant with RCE readout, including silicone tracker trigger and hits.

the photons from reflecting back. The timing resolution reached by some of the better devices was routinely around 10 ps. The threshold level was set high to 400 mV to ensure good timing an rejection of any dark pulses.

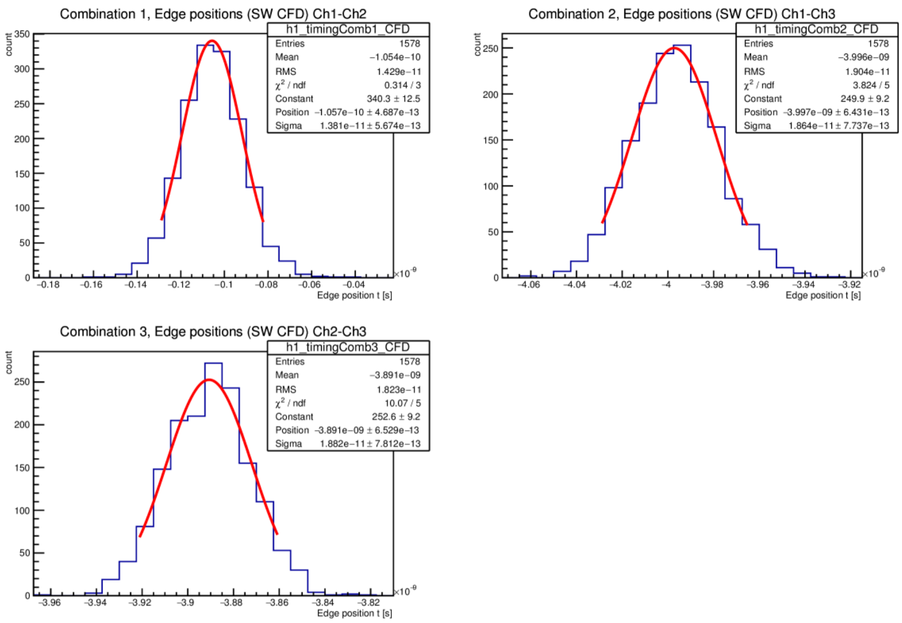

Figure 4.8: SiPM timing resolution combinations.

The Figure 4.8 shows a timing resolution analysis of the three pieces of SiPM detectors we used. Three are needed in order to calculate the individual resolution of each one from their combinations; if we could be certain they are identical, two would suffice, but that is not our case. The individual resolutions of the three devices σ_a, σ_b, σ_c can be extracted from the combined resolution values by solving the set of equations 4.1.

$$
\begin{aligned}
\sqrt{\sigma_a^2 + \sigma_b^2} &= \sigma_{ab} \qquad & \sigma_{ab} &= 13.81\,\text{ps} \\
\sqrt{\sigma_a^2 + \sigma_c^2} &= \sigma_{ac} \qquad & \sigma_{ac} &= 18.64\,\text{ps} \\
\sqrt{\sigma_b^2 + \sigma_c^2} &= \sigma_{bc} \qquad & \sigma_{bc} &= 18.82\,\text{ps}
\end{aligned}
\tag{4.1}
$$

The results we obtain are

$$\sigma_a = 9.6\,\text{ps},$$
$$\sigma_b = 9.9\,\text{ps},$$
$$\sigma_c = 16.0\,\text{ps}.$$

These SiPMs in this setup have a better timing resolution than the ToF bars, which is very advantageous for timing performance measurements. However they could not be used in place of ToF at the LHC, as the detectors are inline with the detected particles and would not survive exposure to the unavoidable radiation doses.

The set of SiPM detectors is mounted on a remotely controlled precise movable table. This means the $3 \times 3\,\text{mm}^2$ footprint is our trigger area, allowing to select a part of the bars (like near the edge or further from it) to be studied, as well as aim at a specific train, measuring its response, timing performance or observing crosstalk in the others.

More details about the SiPM devices are in [29].

Alignment of the SiPM

For proper operation, the SiPM detectors must be carefully aligned with the train we aim to test. This is best done using SiT with readout triggered externally. SiT hitmaps during this process are in Figure 4.9, where the simple beam profile is recorded by triggering on SiT itself, the bar profile from train 2 by triggering SiT by the bar and lastly the SiPM profile by in turn triggering SiT by it. The SiPM is moved using the precise movable table it is mounted on to align it with the center of a bar vertically and touching the edge of the bar horizontally. From this starting position, we can aim at the other trains by knowing the train widths and also move to the desired distance from the bar edge.

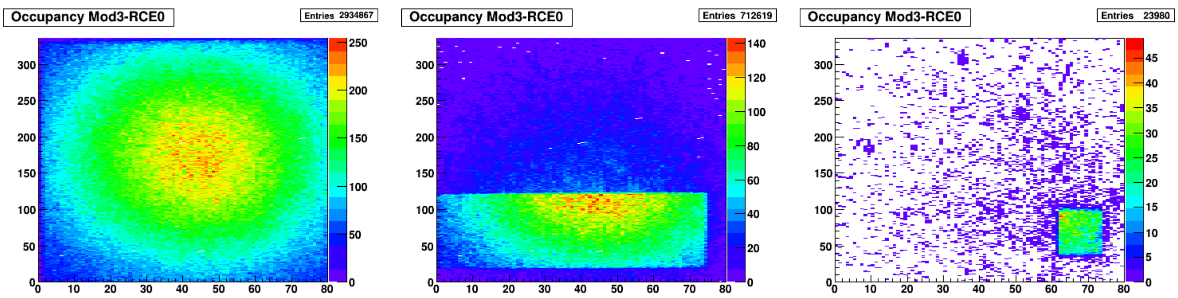

(a) (b) (c)

Figure 4.9: A set of SiT hitmaps during SiPM alignment. The image (a) shows the beam profile, (b) the profile of a bar from train 2 and (c) the SiPM aligned with the edge of the bar. The ToF is not well aligned with SiT here, which is not strictly necessary for a beam test.

4.2.4 Beam Tests at SPS North Area

The beam test campaigns were typically done at CERN SPS North Area (Prévessin site), beamline H6, which has a typical beam energy in the range of $80 - 140\,\text{GeV}$. The beam is secondary and is generated at a target (T4) hit by a proton beam from the SPS accelerator and usually consists of mixed hadrons at a set energy and polarity (in case of positive beam, the beam contains roughly 2/3 pions, 1/3 protons and a few kaons as well). The beam type, energy and polarity is set depending on the needs of the current users at both the H6 and H8 beamlines as they share a common target T4 from which the secondary beams originate. However, the beam shape can be tuned at each beamline independently while the current primary user at the beamline has precedence with their beam shape requirements. There are multiple experiments running at the beamline along the beam path.

Even with its variability, this beam is advantageous for our tests as it closely imitates the MIP (minimum ionizing particle) behaviour of the protons at the LHC while the variable beam constituents have only a small impact on the Cherenkov angle. In cases where identification of the particle type would be important, the CEDAR (CErenkov Differential counters with Achromatic Ring focus) particle identification detector can be used as a trigger [8].

Unlike a typical bunched beam, the beam at the SPS North Area lacks the bunch structure, coming in roughly 5 s long continuous spills each time. This is achieved by a period of "debunching" when the RF cavities are turned off temporarily and the particles are allowed to drift out of their bunches [30]. The debunched beam is then slowly scraped off by an extraction septum, as seen in Figure 4.10 – this produces the spill itself. The beam then hits the targets designed to generate the secondary beams leading into the individual beamlines. The typical beam intensity at our test stand is around 10^5 particles per spill, but can be tuned depending on user requests. The transverse dimensions of the beam can also be tuned, we usually requested at least 2×2 cm to cover the entire active area of our detector system.

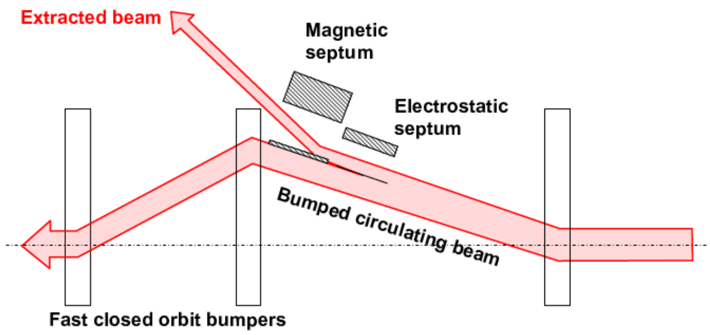

Figure 4.10: Extraction septum on the SPS. Image credit: [31].

When supplying the beam to North Area, SPS first accepts a lower energy beam from the preceding parts of the CERN accelerator complex (Linac2/Linac4, PSB, PS). This beam is then accelerated to several hundreds of GeV. After debunching is finished, the septum engages, producing a spill.

The SPS is also shared with other experiments, often including filling the LHC. The frequency of the spills depends on the current supercycle configuration (essentially on how many other experiments require the beam from SPS apart from the North Area) and usually range between $1 - 4$ per minute. The SPS suprecycle monitor is shown in Figure 4.11.

4.2.5 Beam Tests at DESY Test Beam facility

During the LS2 (Long Shutdown 2) period at CERN, several of the beam test campaigns were carried out at DESY in Hamburg instead, with a suboptimal electron

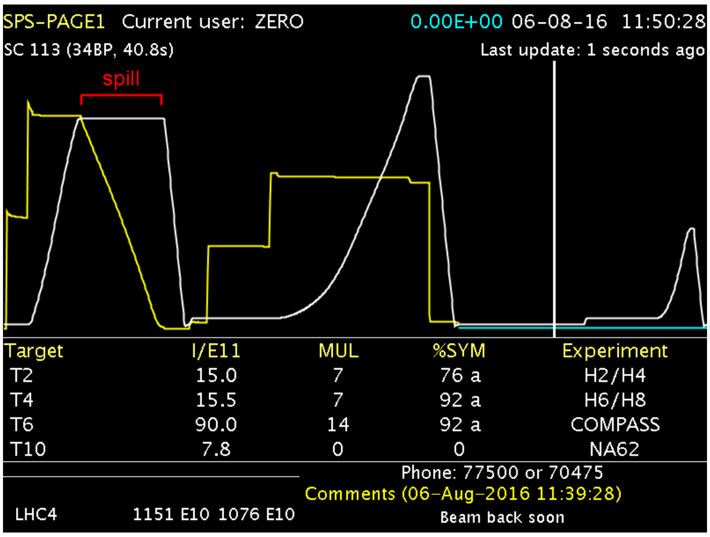

Figure 4.11: The SPS supercycle monitor. The white curve represents the current through the SPS magnets, which is proportional to the beam energy. The yellow and blue curves represent the SPS beam intensity. The spill period of about 5 s is marked in red, the intensity in SPS is seen to gradually decrease during the spill. The vertical white line scans across the supercycle, denoting the current point in time and plotting any changes behind it. The current status can be monitored at `https://op-webtools.web.cern.ch/vistar/vistars.php?usr=SPS1`.

beam with maximum energy of 5 GeV. This beam interacts differently than the MIPs, generating significantly more secondaries along its path. While direct evaluation of the detector performance was not seen as possible with enough precision, comparative studies evaluating the impact of particular modifications to the ToF system, like the out-of-vacuum upgrade and glueless ToF bars, were carried out.

The DESY II Test Beam Facility beam generation scheme is in Figure 4.12. More details about the infrastructure can be found in [32].

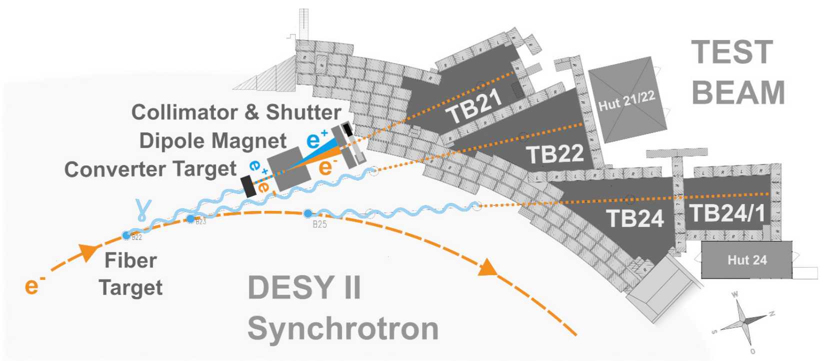

Figure 4.12: Beam preparation in the DESY II Test Beam Facility. Image credit: [32].

4.3 Outside signal interference considerations and setup shielding

Shielding the ToF setup from outside interference is paramount. Failure to do so would inevitably distort the precious fast edge the detector produces, reducing timing resolution. The effect of artificially adding interference to a ToF signal is in Figure 4.13. The interference added was recorded in the LHC tunnel and is most likely in large part originating in the TETRA communication system as the interference had a dominant frequency of 430 MHz (matching one of the TETRA frequency bands) and the system is known to be used by the CERN Fire Brigade. As per our information, this system cannot be turned off even during LHC fills for safety reasons.

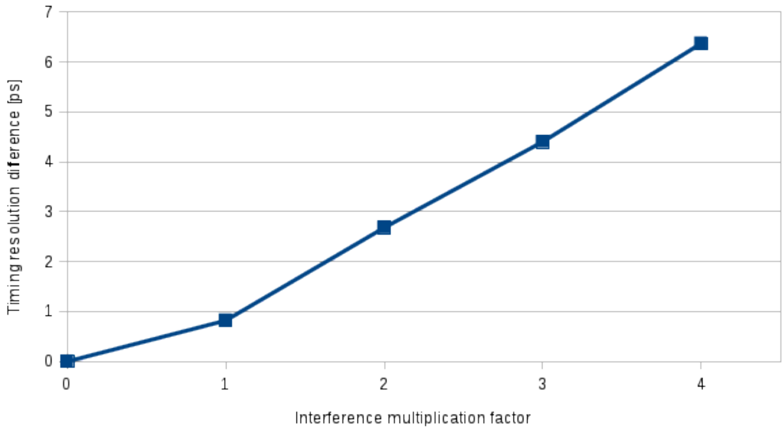

Figure 4.13: The effect of an artificially added interference on a ToF pulse timing resolution. The base interference waveforms (with the multiplication factor 1) were recorded with the ToF setup in the LHC tunnel during installation, while the timing pulses the interference was added to are from previous test beam measurements.

4.3.1 Interference in common microwave communication bands

During analysis of one of the very early PMT measurements using laser, the waveforms were in rare cases found to be contaminated with external interference of harmonic nature, reaching up to 100 mV amplitude with period of roughly 1.1 ns. Such interference inevitably led to much worse timing, but also smeared amplitude and other histograms of the signal characteristics. After a brief investigation, a likely source was identified as a cellphone communicating at the GSM-900 band. A closer look at these waveforms in Figure 4.14 supports the cellphone hypothesis further, as the frequency is identified to be about 910 MHz. The upper bound of the European GSM-900 band for device outlink is 915 MHz [33], making it a perfect match.

In hindsight, this is not surprising since we work with very high amplification ratios and the PMT was not shielded by the Roman Pot. A lesson was learnt from this and all further measurements were performed with all nearby cellphones set to flight mode. Further care was taken to make sure there are no WiFi access points or laptops nearby that could cause similar issues at the 2.4 GHz WiFi band. These precautions are the most relevant to laser measurements, where the operator is in a close proximity to the setup (something that is not possible at beam tests), however a readout laptop is present at beam tests and is therefore placed further from the sensitive parts of the

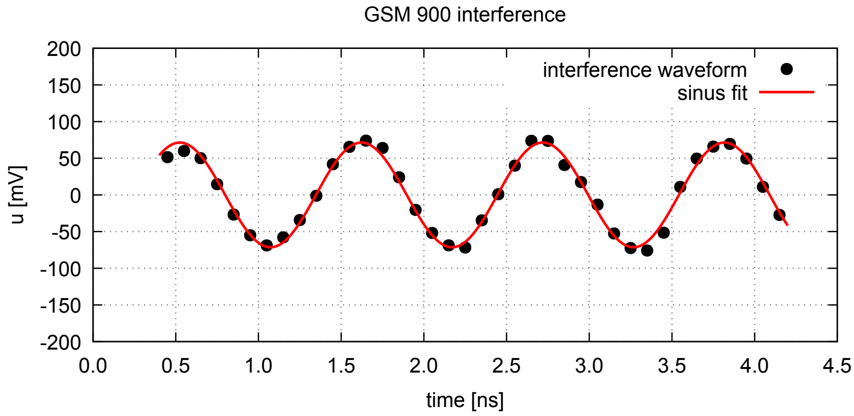

Figure 4.14: An example waveform of the interference picked up during the PMT measurements. The harmonic nature is clear, further illustrated by a sinus fit. The source was identified as a cellphone communicating at the GSM-900 band, as the fit frequency of 910 MHz falls within the GSM-900 uplink frequency range.

setup. In case of the diode laser measurements, the laser head itself is also a source of interference due to the fast nature of the driving pulse. The laser head was therefore also placed further and aimed away from the sensitive parts of the experimental setup. All the results presented in this work are based on data acquired with these precautions taken.

4.3.2 Shielding of the Roman Pot

Initially, the shielding of the experimental setup was expected to be provided by the combination of the Roman Pot container itself and good quality coaxial cables, while the signal processing modules (PAb, CFD, TDC) had their own aluminium/steel housings serving this purpose. Not all measurements were performed with the Roman Pot in use however, especially those using the laser setup instead of the particle beam. Initial attempts of determining what parts would benefit from shielding were performed, the results are in Figure 4.15. Based on these results, the high voltage line, especially the HV divider, is the most susceptible to carrying outside interference into the system, while physically shielding the PMT body itself also has a significant effect.

Another source of interference was previously identified in the flex cables for SiT, where the digital communication induced observable disturbances in the ToF signal lines. The flex cables for both SiT and ToF were therefore wrapped in a nickel shielding tape. This change was kept on the SiT cables even after the introduction of the radical out-of-vacuum redesign where ToF no longer uses the flex cables to carry its signal.

To make matters more professional, further tests in a specialized electromagnetic field exposure chamber (Figure 4.16) revealed that the Roman Pot itself is not sufficient at shielding, interference can for example again easily enter on the HV supply line for the PMT or any other feedthroughs.

Based on these detailed experiments, the HV line, HV divider, but also the ToF coax cables were further shielded using a special nickel shielding tape.

With further development of AFP-ToF, especially the addition of a third amplification stage and lower operational PMT gain, the requirements on shielding became much more strict and a renewed effort was launched in this direction. The above mentioned modifications proved very useful, while the out-of-vacuum redesign itself helped

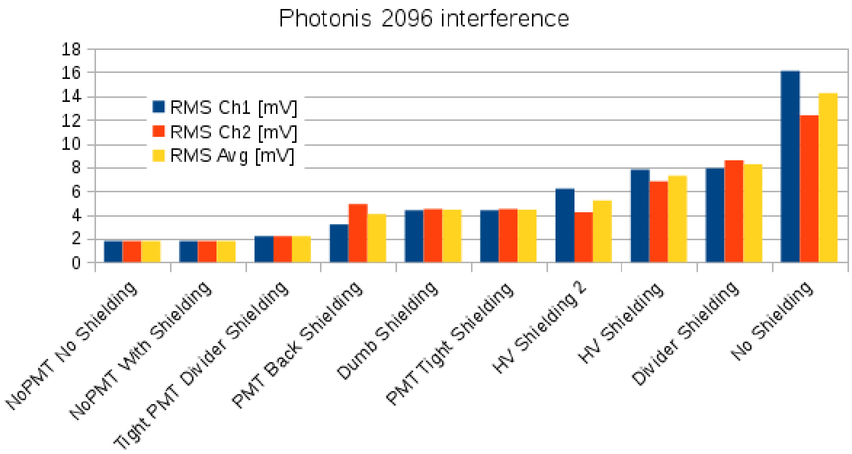

Figure 4.15: Results of simple attempts of shielding various parts of the system by a fine copper mesh.

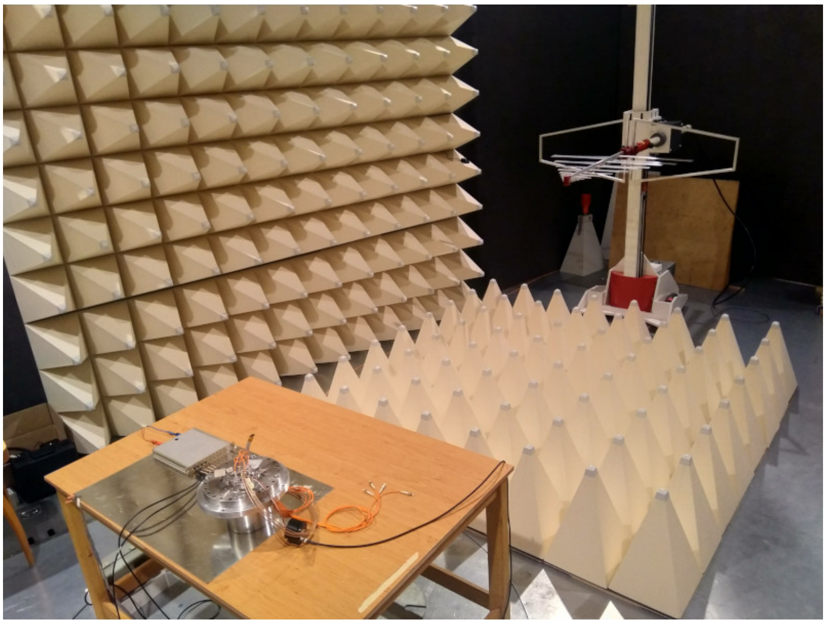

Figure 4.16: Professional tests of electromagnetic field interference with the ToF equipment. At a particular frequency during the scans, the power supply would always shut down; a battery was therefore used instead to power the ToF amplifiers.

greatly by simplifying the signal path and removing the problematic feedthroughs. Still, further steps were taken, like wrapping the PMT body in a thick shielding tape, as seen in Figure 4.17. Furthermore, a ferrite bead was installed on the HV line near the PMT in an attempt to block high frequency interference further.

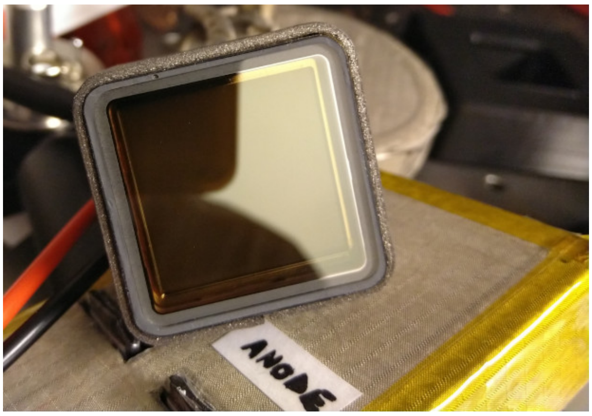

Figure 4.17: An MCP-PMT for ToF wrapped in the extra thick shielding material. An experimental HV divider with the thinner nickel shielding tape can be seen below.

4.4 High detection rate considerations

In real operational conditions at the LHC in Run 3, the AFP system can expect up to 20 MHz proton hit rates. This is up from 5 MHz in Run 2 due to a planned luminosity increase. In the future, HL-LHC (High Luminosity LHC) would ramp up intensities even higher, but this is out of scope of this work.

Such high rates have several impacts we need to take into consideration. Firstly, we need to make sure the detector can actually function at high rates. Most significant bottlenecks here are MCP-PMT saturation (deteriorating its gain) and TDC readout rate. Secondly, there is a higher pile-up, putting increased demand on the precise timing in order to distinguish individual vertices at the collision point. The third impact is the requirement of radiation hardness of all involved components and sufficient lifetime of the MCP-PMT in terms of integrated charge.

The nature of the beam tests does not allow to vary the event rate in a way that would be useful for evaluation of the rate capability limits. Since only two pieces of ToF equipment may be the rate capability bottleneck (the PMT and the HPTDC), dedicated tests were done to perform these stress tests in laboratory conditions. In case of the PMTs, the laser setup with the diode laser system was used, utilizing its capability to change the output pulse rate in a wide range while also being able to control the single pulse strength with filters. For the HPTDC, a testbench with artificial input signal source was sufficient.

4.5 Cherenkov radiator bars

One of the major improvements during ToF development was the introduction of glueless ToF Cherenkov bars.

Manufacturing the bars as a single piece was initially considered not feasible. The original ToF design, installed in 2017, included bars that were glued together from two pieces. While the geometrical precision suffered slightly, this was within acceptable levels. The primary issues were caused by the fact that the glued joint is a weak point in multiple ways. Not only is it prone to breaking with mishandling or during transport, but it also cuts off wavelengths below 250 nm and its optical properties further degrade with exposure to radiation doses. These effects were shown previously in Figure 3.5. A simple conclusion is that removing the need for glueing would improve both the performance and the lifetime of the ToF system.

Optical contact bonding of the polished surfaces was considered in place of the epoxy glue. This option was seriously pursued, but experts at Meopta in Přerov eventually concluded the bonding surfaces were too small for the long lever arm the bars constitute.

Finally, the optics manufacturing experts at our department (The Joint Laboratory of Optics in Olomouc), where the original bars we produced, came up with a procedure to manufacture the bars in one piece. This labour intensive process paid its dividends and produced perfect bars with only a minor compromise (a slightly rounded off internal corner, as can be seen in Figure 4.18).

The signal amplitude generated by the bars was increased by a factor of $1.6 - 1.9$, as can be seen in Figure 4.19. Timing performance was also significantly improved, reducing the timing resolution measured by $15 - 20\,\%$. This was however only apparent when testing at SPS again due to the unsuitable beam at DESY, where no significant timing improvement was observed.

While a more significant change in timing performance was expected given the signal strength improvement, the limited effect is likely due to dispersion effects on the signal arrival to the PMT (the additional short wavelength photons take slightly longer to reach the PMT due to the higher refractive index they experience, contributing less to the timing performance). The dispersion effect is well covered in [34].

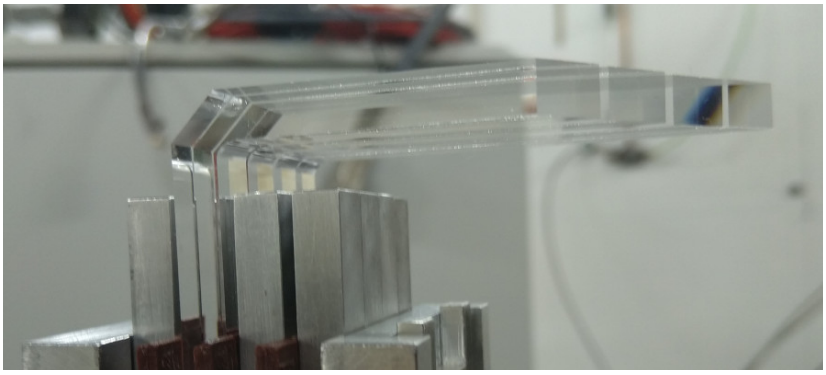

Figure 4.18: A first batch of the glueless bars put to test at the DESY beam test facility. Note the slight curve on the inside of the bar ankle where previously a clean 90° angle was with the glued bars. This is necessitated by the single piece production techniques.

The train widths in the final version of the ToF bars are 3 mm, 3 mm, 5 mm and 5.5 mm for trains $1 - 4$ respectively. The trains 1 and 2 feature a taper.

4.6 MCP-PMT

The MCP-PMT is a core component of the AFP-ToF system and as such is responsible for many of the capabilities and limitations of the system. In this section we will explore

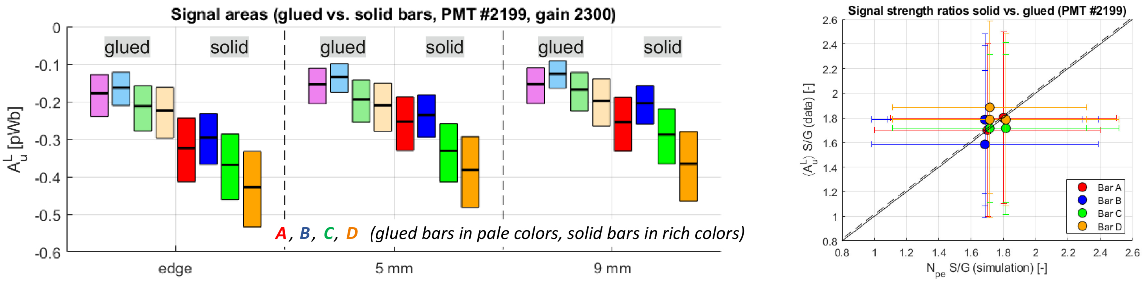

Figure 4.19: A comparison of signal strength when the original glued bars and the new glueless bars were used with otherwise equivalent test beam setup. The glueless bars have $1.6 - 1.9\times$ stronger response. The integrated pulse area was used for the evaluation. On the right, the beam test measurement results are compared to previously simulated predictions, showing a nice match. The error bars show the spread of the individual waveforms, not the uncertainty of the average value. These plots have been previously published in [34].

how the parameters of these devices changed as new generations became available and were evaluated.

4.6.1 PMT variants and modifications

There were three major generations of Photonis miniPLANACON MCP-PMTs of interest to AFP:

- **XPM85112/A1Q** – this variant was used during the first installation in 2017. It suffered from a short lifetime, offering a deteriorating performance throughout the one year operation. This variant has $10\,\mu$m pores.
- **XPM85212/A1-S** – an improved variant with ALD (Atomic Layer Deposition) treatment of the MCP pores, a technique that has been demonstrated to significantly improve lifetime [35]. These however suffered from numerous issues (extreme crosstalk when multiple channels are hit simultaneously, long recovery of gain after exposure to high pulse rates), as we reported in [36]. These have $6.5\,\mu$m pores, a feature hoped to improve timing.
- **XPM85112-S-R2D2** – the next generation of the devices manufactured with a modified ALD procedure, featuring double ALD treatment. These were evaluated as suitable for AFP-ToF [37] and are currently considered the baseline MCP-PMT type. These have $10\,\mu$m pores, returning to a proven technology.

Between the second and third generation, a decision was made to also change the PMT backend from the stock to a new solution developed in-house by the AFP-ToF group. Electrical diagrams of the changes are in Figure 4.20. These were then supplied to Photonis to be integrated onto the PMT during the final steps of the manufacturing process. The custom backend significantly improves the crosstalk behaviour and features proper MMCX RF connectors for individual channels instead of the pin headers, as seen in Figure 4.21. Details about the backend modifications were published in [37].

One other modification present in certain MCP-PMT pieces on our request was a reduced anode gap from the usual 2.9 mm to 0.6 mm. The reduced gap was expected to reduce the magnitude of the charge sharing effect, a claim that is scrutinized in

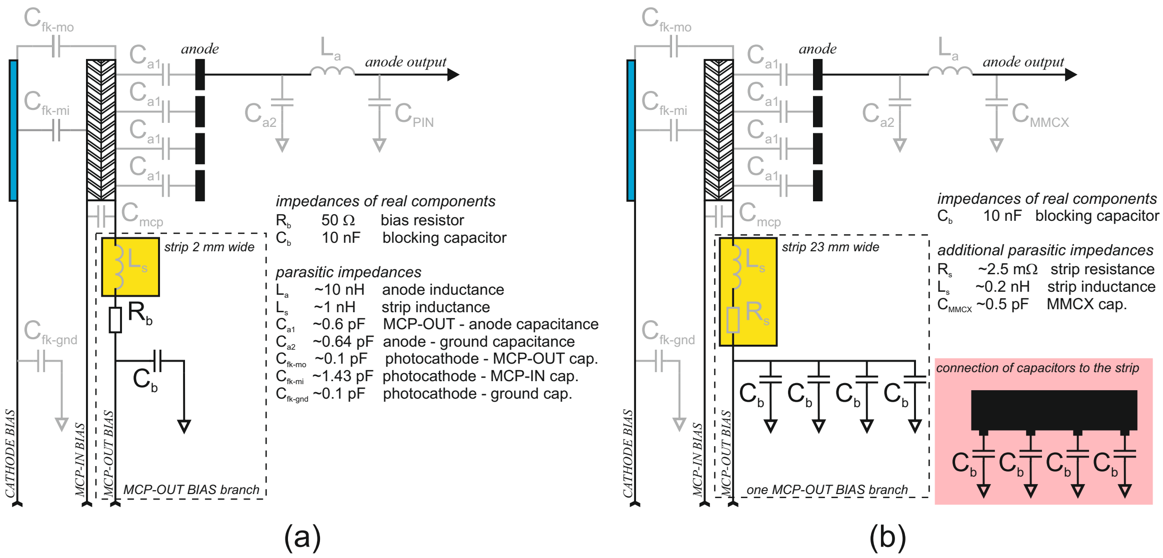

Figure 4.20: Semi-realistic circuit diagrams of the original backend (a) and the custom modified design (b). Real components of the backend are shown in black while the parasitic impedances are added in gray. This diagram has been previously published in [37], where a more detailed description can be found.

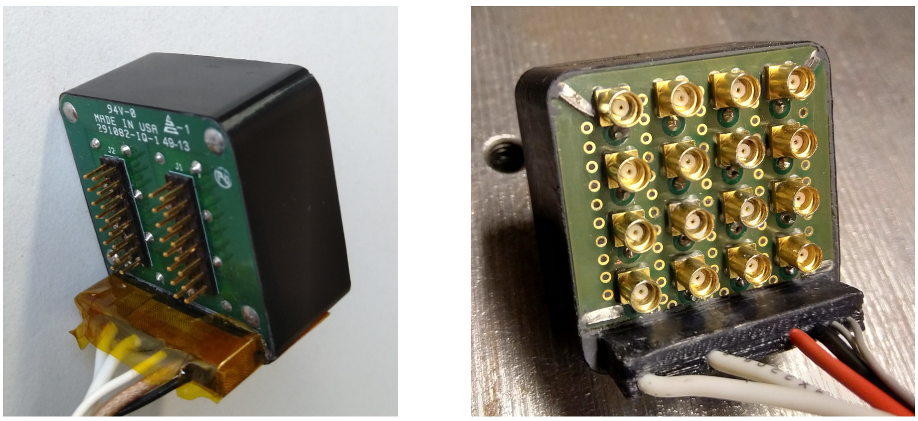

Figure 4.21: A comparison of the original PMT back end pin headers (left) and the new backend with the MMCX connectors (right).

subsection 4.6.7. This modification is not bound to any particular type of PMT and can be easily performed by the manufacturer by the removal of a normally present spacer during the assembly process.

A few comparable MCP-PMT devices by Hamamatsu were tested as well. These did not bring any significant improvement over the Photonis miniPLANACONs, so were considered to be only a backup solution. Due to the slightly smaller dimensions, to make a good use of them would mean redesigning and manufacturing entirely new sets of ToF bars, a very pricey and time consuming endeavour that we wanted to avoid unless absolutely necessary.

The updated generations of Photonis MCP-PMT devices were thoroughly tested and scrutinized for feasibility by the author of this work, resulting in the two core papers [36, 37] of the PhD. The following is in large part a summary of these, with many more yet unpublished results included as well. The only exception, where we relied solely on results of other groups, is related to lifetime.

4.6.2 Lifetime

As reported by the Lehmann group in [38], the originally used MCP-PMT type is not very suitable for prolonged operation and suffers from degradation after enduring as little as $< 0.5\text{C/cm}^2$ of integrated charge. In our case, this would mean the need for replacing them with fresh pieces even multiple times a year.

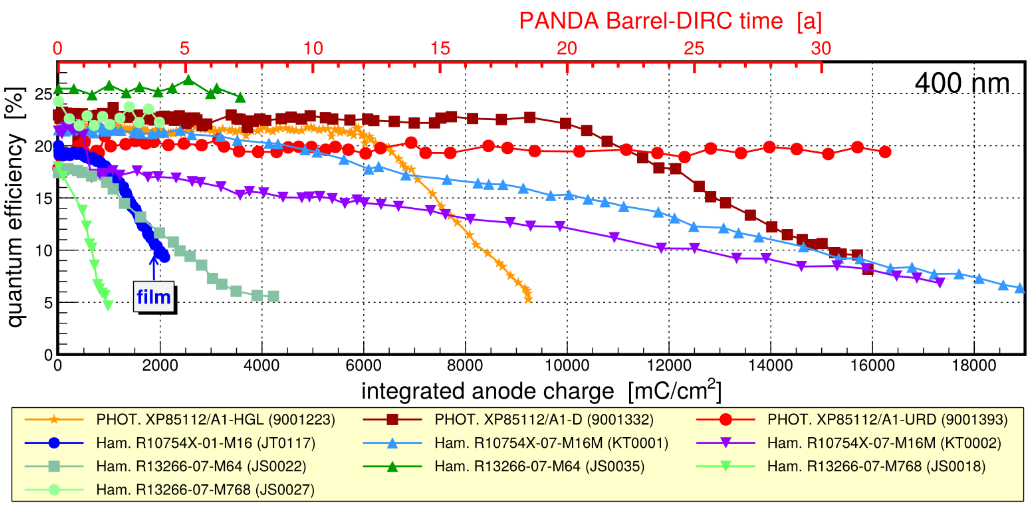

Figure 4.22: MCP-PMT lifetime heavily depends on the long life measures applied. Based on these result by Lehmann, the single ALD XPM85212/A1-S (equivalent to A1-D in the plot) can sustain up to 10C/cm^2 and the double ALD XPM85112-S-R2D2 (equivalent to A1-URD in the plot) shows no signs of degradation even above 16C/cm^2, a $10\times$ improvement on non-ALD lifetime enhancing techniques and $100\times$ improvement on the PMTs not treated for long life, like the XPM85112 originally used for AFP-ToF. Image credit: [35].

Improved variants of the MCP-PMT devices utilizing ALD (Atomic Layer Deposition) treatment techniques recently became available, some reaching nearly 2 orders of magnitude improvement over the standard MCP-PMT types [35], as shown in Figure 4.22. This was achieved by suppressing the mechanisms responsible for the accelerated ageing, such as ion feedback (charged ions are released by the high surface area of the MCP and are accelerated towards the photocathode, damaging it over time). As a welcome side effect, reduced ion feedback also reduces the presence of afterpulses.

In particular, the XPM85212/A1-S and later XPM85112-S-R2D2 MCP-PMT types from Photonis were selected for evaluation of feasibility for the AFP ToF system based on their excellent lifetime properties [35]. The lifetime is expected at a level where even annual changes should not be needed, with the expectation of enduring the entire Run 3 unless other issues arise.

4.6.3 Quantum efficiency

Quantum efficiency (QE) is a measure of how many photons get converted to useful photoelectrons by the photocathode. The photoelectrons are then pulled out of the photocathode by the front stage bias. In case of classical PMTs, these are pulled towards the first dynode in the cascade. In our case of MCP-PMT devices, they are pulled towards the MCP input side. QE value does not cover how many are then successfully multiplied (hitting a pore and starting a cascade); this is described by a separate parameter, collection efficiency (CE). CE is roughly proportional to the pore coverage factor of 60 % and is independent of the wavelength of the incident photon, whereas QE is strongly wavelength dependent.

Different photocathode materials excel at some wavelengths while being poor at others. In our case, the Bialkali photocathode is optimized for detection of blue and near UV light, a perfect match for our needs. This was therefore not changed during the ToF development, QE was simply monitored as a quality parameter of interest. QE deterioration due to photocathode damage by ion feedback is expected to be a major factor in PMT degradation [38]. Ions released from the high MCP surface area are accelerated towards the photocathode and can hit it at energies around 1 keV. We unfortunately do not have QE measurement data of the MCP-PMTs from the 2017 run to make a comparison of QE before and after the run. Still, QE curve is of interest – it was necessary for example for simulation of the glueless bars, giving an estimate of the signal strength increase to be expected.

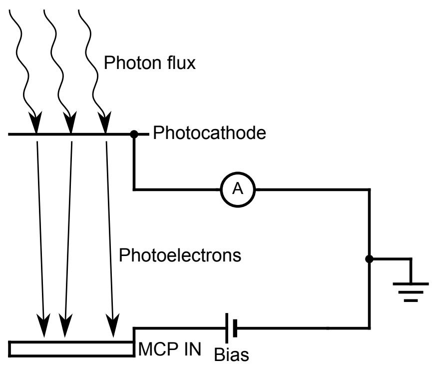

Figure 4.23: A scheme of the QE measurement setup. The photon flux releases photons from the photocathode, these are then extracted by the bias voltage. The current needed to replenish the photocathode with electrons is measured for each wavelength of interest.

The QE measurement scheme is in Figure 4.23. A small bias voltage is used to extract the photoelectrons (electrons freed by the photoelectric effect) from the photocathode. In case of classical PMTs, this bias would be applied between the photocathode and the first dynode; we have no dynodes in case of the MCP-PMT, so we chose the MCP input side instead. The current needed to replenish the extracted electrons from the photocathode is the measured variable, depending on the wavelength of the incoming light. The current is measured using a picoamperemeter. The light source is a xenon discharge lamp with a monochromator (pair of diffraction gratings) used to select the wavelength. The lamp needs to run for at least an hour for the light output to sufficiently stabilize.

In order to obtain the QE, we need to determine the photon flux at each wavelength. To do that, a reference detector is needed, in our case a calibrated photodiode. The QE curves of two such diodes are in Figure 4.24.

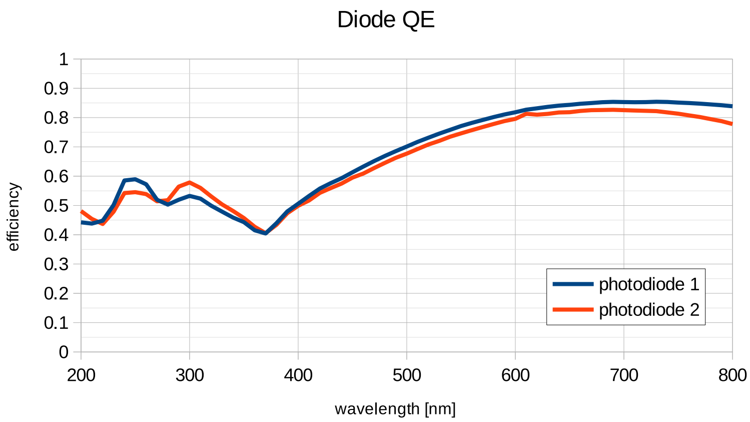

Figure 4.24: Quantum efficiency of the calibrated reference diodes as obtained from their calibration protocols.

Even when the lamp is stabilized, a good practice is to do two calibration measurements with the photodiode, one before and one after measuring the device of interest. This is to ensure the light output has not significantly changed. If the change is at an acceptable level, the average of the two calibration runs is used in the calculations. If not, the measurement is repeated.

Before measuring the PMT, we must determine the appropriate bias voltage. We start at few volts and slowly increase the bias until the current through the PMT (illuminated by the light source at a wavelength expected to give a good response) saturates. Then we add a 50 % margin. We do not want to push too high, we would be simply adding dark current to the measurement. With all the MCP-PMTs measured, the optimal bias was determined to be 15 V. Then we can start the full measurement with the PMT. The currents recorded at each wavelength step are in Figure 4.25.

The calculation of the $QE_{\mathrm{PMT}}(\lambda)$ at each wavelength is then straightforward, using Equation 4.2. The resulting QE curves are in Figure 4.26.

$$QE_{\mathrm{PMT}}(\lambda) = \frac{I_{\mathrm{PMT}}(\lambda)}{I_{\mathrm{diode}}(\lambda)} QE_{\mathrm{diode}}(\lambda) \tag{4.2}$$

The measured quantum efficiency matches the expectations from the manufacturer's datasheet for the type, as previously shown in Figure 3.16.

4.6.4 Gain curves

A gain curve is a crucial description of the amplification capability of any PMT. It can be used to tune the high voltage supplied to the PMT to set a particular gain.

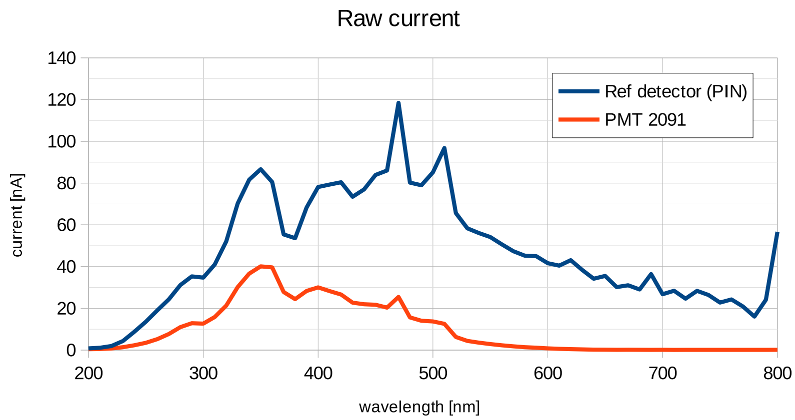

Figure 4.25: Current through the illuminated devices, recorded by the picoamperemeter at each wavelength step.

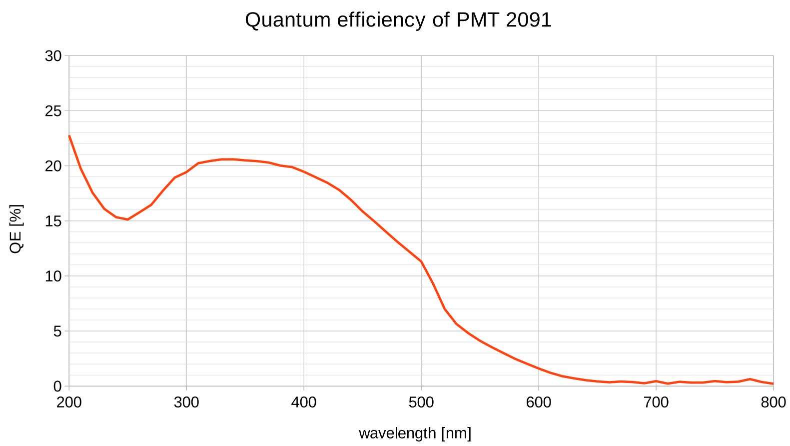

Figure 4.26: The obtained quantum efficiency curve for MCP-PMT with serial number 9002091.

A typical gain curve as it appears in the datasheet for the Photonis XPM85112 series MCP-PMTs is in Figure 4.27a.

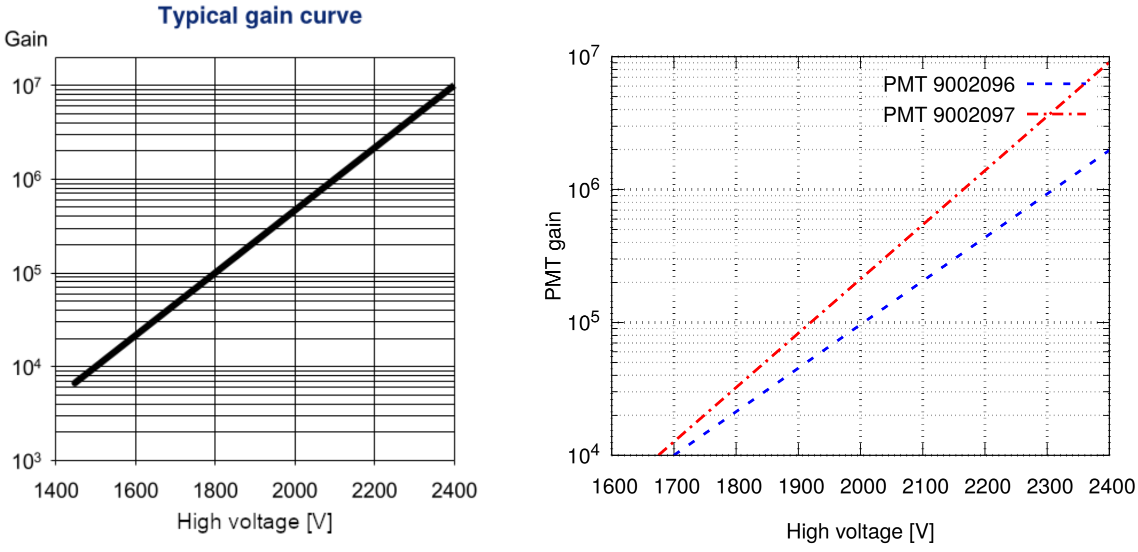

(a) **(b)**

Figure 4.27: A typical gain curve as supplied in the datasheet for a Photonis mini-PLANACON XPM85112 MCP-PMT [24] (a) and the approximate gain curves interpolated from the manufacturer's test protocol data for the XPM85212/A1-S (b).

At first, we relied on simple interpolation of the gain at two test points given by the manufacturer in the test protocol specific for each particular PMT piece, as seen in Figure 4.27b. We would then fine-tune the HV supply for the PMT to a desired level at a beam test.

As our understanding of the system progressed and we required more detailed results, such as an estimate of number of photoelectrons at test beam measurements, the need for measuring more precise gain curves ourselves arised. A gain curve measurement method using the available equipment was therefore devised and implemented by the dissertation author.

The developed gain curve measurement method is based on pulse charge integration. A baseline reference is obtained at a high gain (up to 10^6) without any amplifiers, recording waveforms when the PMT is struck by single photons only. The charge contained in the pulse is obtained by integrating the pulse waveform recorded by an oscilloscope and dividing it by the known load of $50\,\Omega$ at the scope input. This charge value can then be divided by the elementary charge e, obtaining the absolute gain of the PMT. This is due to the fact that the single detected photons generate a single photoelectron at the front of the PMT, so the ratio of the charges gives the MCP multiplication factor, or gain.

This exact same measurement is then repeated with amplifiers to get their precise gain. Continuing the measurement with amplifiers is critical as the weak pulse would soon drown in noise with decreasing PMT gain. The measurement without the amplifier is then used as an anchor point for the entire gain curve.

After obtaining the first point, the HV is reduced and the measurement with amplifiers repeated, recording the integrated charge again. The ratio to the first point with the known gain is then used to determine the gain at that new point as well.

Before the single photon signal pulse becomes too weak (too close to noise) with the decreasing gain, we continue the measurement at a stronger light level (more photoelectrons per pulse, ~ 5). We need to stitch the measurements at the different light levels together, meaning the measurement at the last HV value feasible with single photons is repeated at the same HV with the stronger pulses. This allows us to tie the different light level measurements together to form a single gain curve. This stitching of stronger light measurements usually needs to be done a second time, going to laser pulses that produce ~ 50 photoelectrons. These steps to stronger light pulses are usually done at gains of roughly 10^5 and 10^4. This allows the measurement to easily cover the gain range $10^3 - 10^6$, compiling the results into a single gain curve.

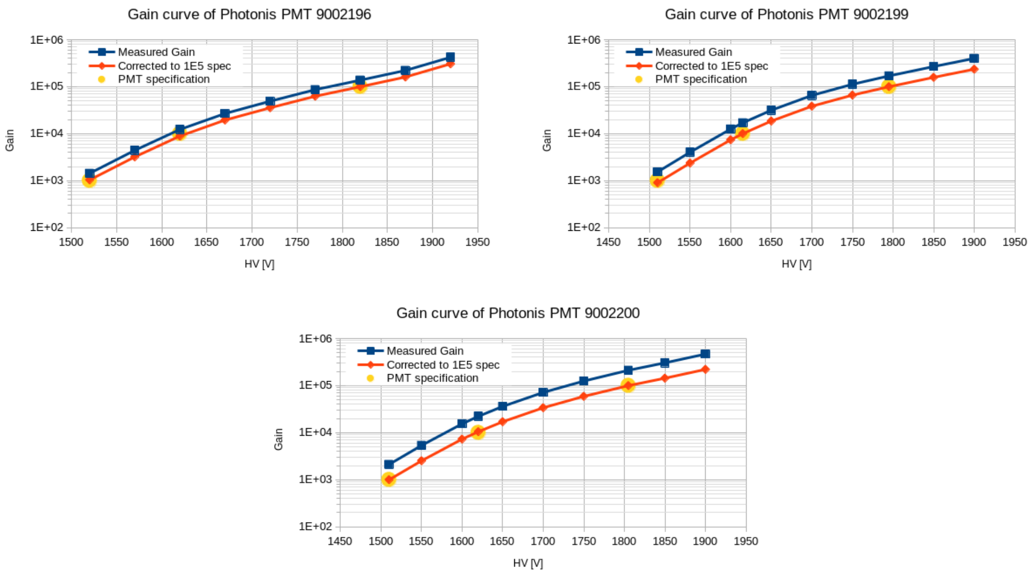

Figure 4.28: Gain curves of the three PMTs of the XPM85112-S-R2D2 type. The yellow points come from the manufacturer's test protocol for each individual piece. The blue curve is the measured gain curve with reference to the single-photon charge; the red curve is a copy of the blue curve, but multiplied by a fixed factor to match the 10^5 gain point from the PMT specification.

The results of this gain curve measurement process for the XPM85112-S-R2D2 (the PMT generation currently in use by AFP-ToF) are in Figure 4.28. There is a clear difference to the gain specification (yellow points) included by the manufacturer. This can be attributed to a different measurement method used; while we use pulse charge integration and our reference is a single photon pulse, the manufacturer uses a known light source to measure the average current given off by the PMT.

When our gain curve (blue) for each PMT is multiplied by a fixed factor in order to match the 10^5 specification gain (top yellow point), we get a shifted gain curve (red). This shifted curve confirms the measurements were performed correctly and the stitching works, because it nicely hits the other specification points with an error of only $1 - 4\,\%$. This means our measurements and the manufacturer's data truly differ only by a small factor. In many use cases for the gain curve, this difference is irrelevant as only a ratio of two points on the gain curve is used, the shift factor simply crosses out. In case of setting up the gain of the PMT, however, one has to be careful which curve is used. We tend to prefer our own measurement with the pulse integration method (blue) as our detector is using the PMT to detect short light pulses as well, making it more relevant.

One way to explain the discrepancy in more detail is to consider collection efficiency effect. The pulse method excludes this from the final result as only photoelectrons that hit a pore and start a cascade are taken into account, including in the single photon reference measurement without amplifiers. The current method on the other hand likely uses quantum efficiency measurements to determine how many photons get converted to photoelectrons and then simply includes the collection efficiency of $\sim 60\,\%$ in the result, making the apparent gain seem lower. This matches the results very well, as the correction factors are 0.72 for PMT 2196, 0.59 for PMT 2199 and 0.47 for PMT 2200.

This is not the full explanation however, as the ratio is somewhat different for the individual PMTs, but it still accounts for a majority of the correction factor with the $\sim 60\,\%$ collection efficiency falling nicely in the middle of the three values. As the devices of the same type are expected to behave the same, the rest could be a simple measurement uncertainty of the unamplified single photon signal where noise was a serious concern, or perhaps an insufficient period for stabilisation of the equipment temperature (laser head, amplifiers, oscilloscope). Another (very likely) source of the error could be PMT response non-uniformity, the gain curves here were obtained using only a single center channel 22 on each device. Nevertheless, these gain curves with uncertainty of roughly $\pm 20\,\%$ are precise enough for the purposes needed, especially considering the values span many orders of magnitude and the uncertainty is global, not of the individual data points, where $< 5\,\%$ variance is expected. After proving the ratio of the gain data points is correct when compared to the manufacturer provided values, the confidence in the results is high and they serve as a good reference for PMT HV tuning.

4.6.5 Uniformity

Uniformity is traditionally a weak point of the MCP-PMT devices, with the channels at the edges and in corners suffering from a reduced signal strength when exposed to the same light levels as the channels in the middle. An example of uniformity results for two PMTs of the XPM85212/A1-S and XPM85112-S-R2D2 types are in Figure 4.29.

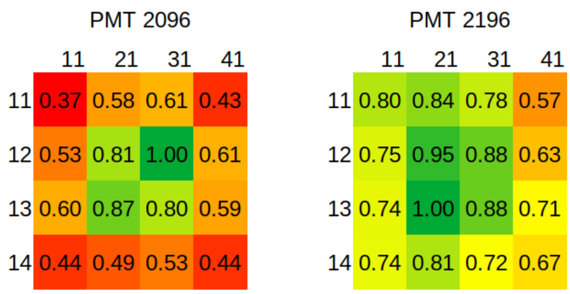

Figure 4.29: Uniformity of the PMTs, relative to the strongest channel. Notice how the edges and corners are significantly weaker, especially in the older generation PMT; the updated ones with the improved backend do not suffer as much, while the edge along the HV connection on the right performs noticeably worse than the other edges. Channel labels are around the outside.

4.6.6 Transit time spread

As previously described in subsection 3.4.6, Transit Time Spread, or TTS, is a measure of how precisely a given device measures the arrival time of single photons. While many experiments including our own use the PMTs to detect pulses stronger than simple photons, it is still a very relevant parameter, telling us how the device contributes to the overall timing resolution of the system.

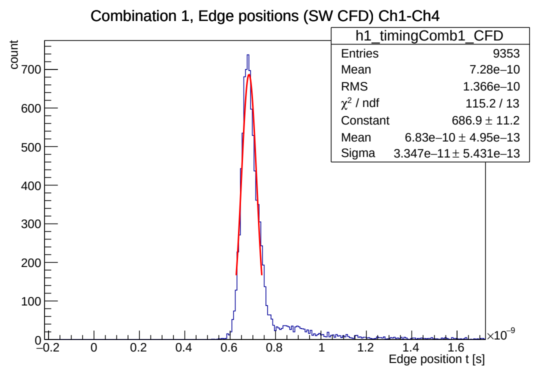

(a) XPM85112/A1Q

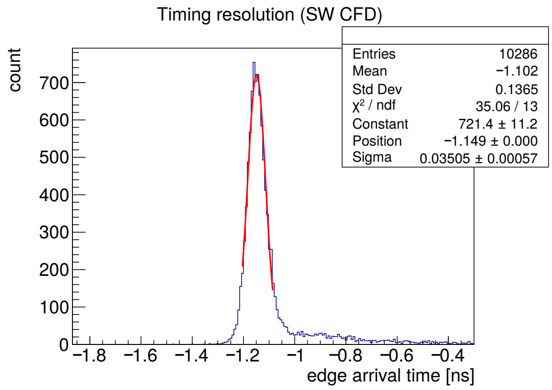

(b) XPM85212/A1-S

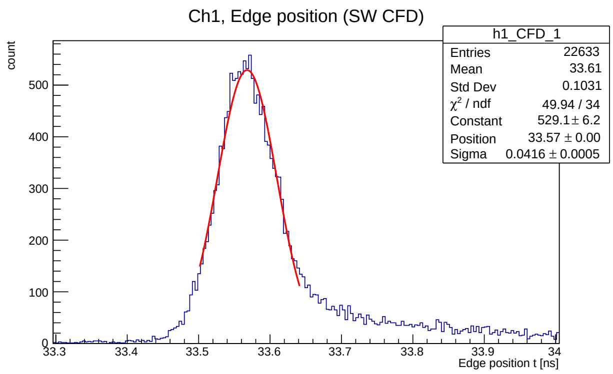

(c) XPM85112-S-R2D2

Figure 4.30: A comparison of TTS measurements of the PMT generations of interest. After subtracting the contribution of the laser pulse length from the fit sigma, the timing resolutions are 29.0±0.5 ps (a), 29.7±0.5 ps (b) and 38.8±0.5 ps (c). Variations among pieces of the same PMT type were not very significant (< 2 ps).

Results for representative pieces from each PMT generation of interest are in Figure 4.30. It is clear that the PMTs currently used for AFP-ToF are inferior to the previous generation in terms of timing resolution. While the PMTs would previously reach around 30 ps TTS, these are closer to 40 ps. Upon closer inspection, it features quite a heavy tail, unlike the other types (the influence of which on the result is circumvented by using a local fit in all cases) – the other types have a more confined area where the bouncing photoelectrons are prominent, not a continuous tail.

While this worse timing is unfortunate, their other properties make the XPM85112-S-R2D2 the necessary choice and the expectation is that the other ToF improvements would help partially offset the difference. As PMTs with smaller pores are expected to have a better timing resolution, it is possible the smaller pores of the XPM85212/A1-S help compensate any adversarial effects of the ALD treatment on timing, something the XPM85112-S-R2D2 cannot do with the return to the 10 μm technology. This is however currently a pure speculation.

TTS is slightly correlated to the gain used. The channel used can also make a difference, with channels at the edges and in corners consistently performing worse at both gain and timing. These effects are illustrated in Figure 4.31. The results in Figure 4.30 were all obtained at a common gain of $5 \cdot 10^5$ and using one of the center channels, channel 22.

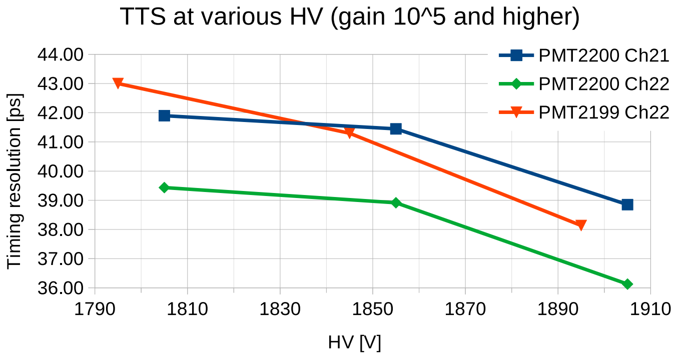

Figure 4.31: TTS as a function of the HV bias, with the timing slightly improving at a higher PMT gain. The channel at the edge of the device (21) is seen to perform noticeably worse than one of the central channels (22), a typical trait of these MCP based photomultipliers.

4.6.7 Crosstalk

Charge sharing

Charge sharing is an effect occurring at the PMT back stage, where the electron cloud leaving the pores is dispersed over more than one anode pad. An illustration of this is in Figure 4.32. While photon hits near the centre of the channel might not share charge with the neighbouring channels, the hits closer to the channel boundaries may share a significant fraction of the charge they generate.

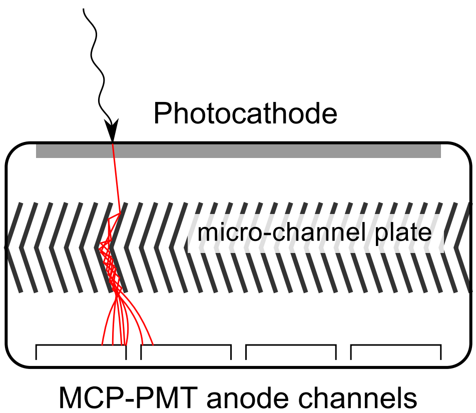

Figure 4.32: A cross section diagram of a typical MCP-PMT device, showing the charge sharing effect. Proportions of the MCP here are not realistic.

Charge sharing in AFP-ToF is not a significant issue when occurring between channels belonging to the same train of ToF bars; the timing information arrives mostly at the same time from all bars in the train, so certain exchange of charge within a train is not really that detrimental, simply causing slight correlation between the channels. While this could reduce the effectiveness of the time averaging from the four bars, it also slightly improves the timing of each bar by letting it “taste” a bit of signal originating from the photons belonging to the neighbours, making the overall impact small.

Charge sharing across trains however is not desired. This is reflected in the design of the bars, more specifically the spacing of bars where they interface with the PMT. The gaps within a train are very narrow (0.4 mm), but there are significant separators between trains (1.4 mm). This layout is shown in Figure 4.33a, which also serves as a visual representation of probed channel layout during the relevant charge sharing tests. In these tests, a single channels was illuminated. The illuminated channel together with two of its direct neighbours and one channel far away were probed for their responses by an oscilloscope. The PMT used was 9002199 of the XPM85112-S-R2D2 type.

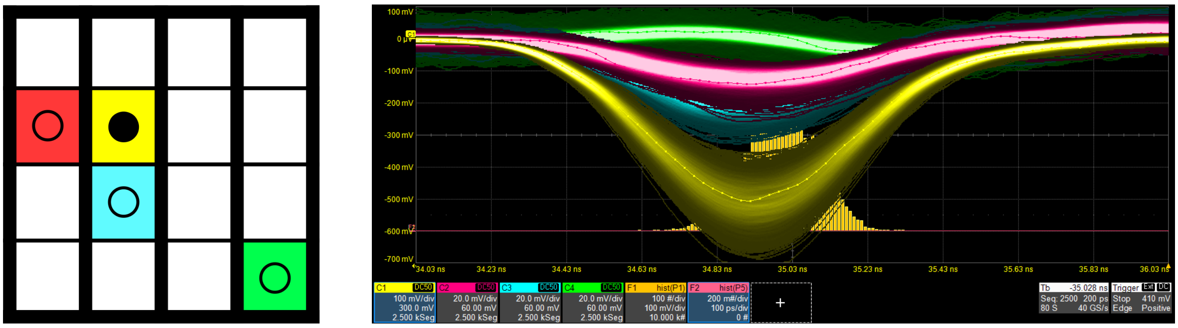

(a) Tested channels **(b)** Waveforms during charge sharing measurement

Figure 4.33: Layout of the channels tested for charge sharing with the gap sizes between the bars marked (a) and an example of waveforms during charge sharing tests (b). The colours in (a) and (b) correspond to where each channel was connected. The yellow channel with the full dot is the illuminated one, all the others with empty dots are also observed. Note the different vertical scale on C1 (yellow) on the scope view (b). These results were previously published in [37].

The results of measurements of the relative charge sharing magnitude compared to the primary signal in the illuminated channel are in Table 4.1. The effect of the anode gap (2.9 mm standard, 0.6 mm reduced) is also included. The illuminated channel was uniformly lit, using the channel mask imitating the ToF bar footprint. The green channel was not evaluated for charge sharing (it contains none due to not being in proximity to the illuminated channel). It serves simply to observe the electronic crosstalk that is present in all channels.

Channel spacing	Standard anode gap	Reduced anode gap
In train (0.4 mm)	7.5 %	5.5 %
Next train (1.4 mm)	5.0 %	3.0 %

Table 4.1: Charge sharing strength relative to the primary channel signal. These results were previously published in [37].

Based on the results in Table 4.1, the reduced anode gap clearly limits the charge sharing, proving to be a useful modification. The wider gaps between ToF trains also help to reduce the undesired parasitic response in bars that were not hit by a particle, showing the gaps serve the purpose as designed.

Electronic crosstalk and ringing

Crosstalk studies were usually done by recording the ToF train hit by a particle and another train (usually a direct neighbour) simultaneously. To capture 8 channels, a two oscilloscope setup was used, with the sync out signal from the first triggering the second. The first scope had an artificial dead time set to allow the other one to finish the readout and processing before recording another waveform, keeping them synchronised.

During beam tests with the XPM85212/A1-S series photomutipliers, this proved very useful, because these PMTs were not behaving well, exhibiting excessive crosstalk. What we recorded were really horrible waveforms with significant oscillations both in the train aligned with trigger and its neighbour (Figure 4.34), or even any other PMT channel for that matter. We could even call the response ringing due to its periodic nature without fast decay.

(a) **(b)**

Figure 4.34: Waveforms exhibiting the ringing behaviour in both the train where we trigger using a SiPM (a) and its neighbour that should ideally be quiet (b).

This massive crosstalk is also clearly visible in Figure 4.35, where the global bar coincidence is plotted when taking data with the full ToF readout chain on a beam test. While the bars in a train fire together quite often, the coincidence with other trains should be ideally minimal, which is not the case.

Timing-wise, the individual bars were in the range of 37-50ps and train combination 34ps (Figure 4.36), a significant downgrade from the previously achieved best ToF results that will be discussed in chapter 5.

The responses in the other trains were so strong that we could actually measure timing resolution on them as a joke too, despite the timing histograms having multiple peaks. Fit of the strongest peak would yield around 47 ps for some of the bars, on par with the train that was actually hit. In a well behaving system, this should never be possible.

We mounted a deep investigation of the causes. When all but one bar were removed from ToF, this behaviour seemed under control. When multiple bars in a train were added, the crazy behaviour returned. The PMTs simply could not handle multiple channels with signal at once. When replacing the PMT for one of the previous generation, (XPM85112/A1Q), the behaviour was fine with otherwise equivalent setup.

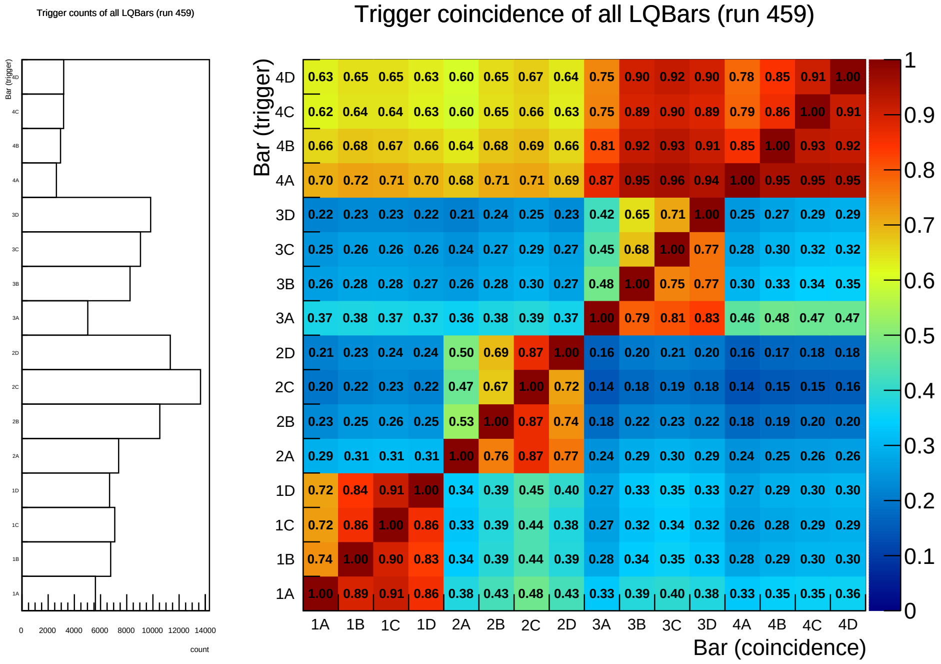

Figure 4.35: Coincidence of bars during full ToF chain measurements using the XPM85212/A1-S type PMT. The bars in train 4 have lower event counts as seen on the left (being mostly out of the beam), making their coincidence values inflated.

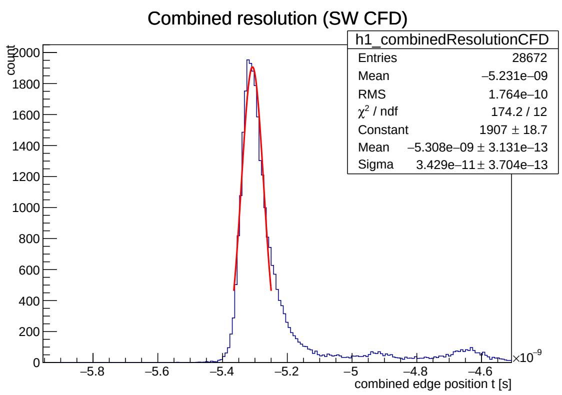

Figure 4.36: Timing resolution of a train using the XPM85212/A1-S PMTs is way worse than the previous generation.

It became clear the XPM85212/A1-S was the culprit, in particular the backend that featured some changes to the previous PMTs. When developing the new custom backend for the next generation of PMTs, one of these misbehaving PMTs was sacrificed and partially disassembled to serve as a test bed for the newly developed backend. Installing it remedied the situation immediately.

With the new backend, the crosstalk was a simple gentle upwards wave due to the unavoidable grounding line lifting when the fast pulse is generated on other channels, as shown in Figure 4.33b by the green waveform. The wild oscillations had disappeared. While the magnitude with a single channel lit was similar at 8 % (shown in Figure 4.37), with four channels illuminated the maximum crosstalk peak became much more manageable at $15-20\,\%$, whereas the problematic PMTs would easily exhibit over 40 % crosstalk of the primary signal in the same scenario.

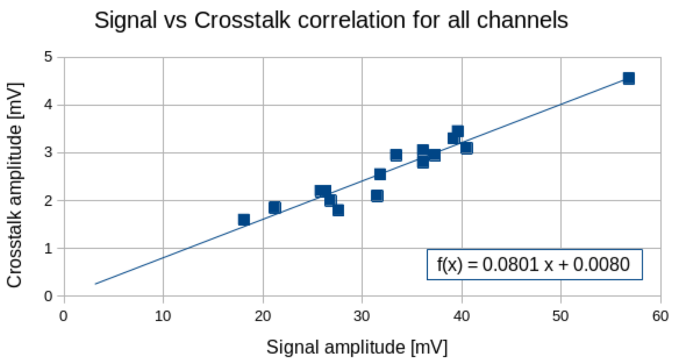

Figure 4.37: Correlation of the primary pulse of in the illuminated channel and the crosstalk observed in the other channels when using the custom modified backend, showing a linear relationship with 8 % ratio. All 16 channels were tested this way, forming the data points in the plot.

4.6.8 Event detection rate capability

Even at LHC Run 2, AFP-ToF was nearing the limit of its capabilities when it comes to event rate. The planned intensity increase for Run 3 therefore necessitated a dedicated development effort to increase the rate capability of the system, especially the MCP-PMTs used. The expected increase was by a factor of four, from 5 MHz up to a maximum of 20 MHz. The results of these efforts were published in [36, 37].

The rate capability cannot be tested on a beam test as there the rate is usually in the range of $5-20$ kHz, orders of magnitude below the target. This is where the diode laser setup becomes a critical tool.

Theoretical approximation

As a first approximation, a theoretical calculation for the rate capability can be used. For this purpose we estimate an average number of photoelectrons generated in the PMT by each ToF bar of the old glued variant (based on previous beam tests and the gain curve measurements) as $N_{\mathrm{pe}} = 20$. The high rate effects are expected to be highly local (discharging the michrochannels hit), we therefore need to multiply this by the number of channels (16) when doing the calculation for the entire PMT.

The calculation is based on the fact that the charge depleted by the multiplication process in the MCP has to be replenished. The strip current replenishing the charge is

$$I_{\mathrm{sc}} = U_{\mathrm{MCP}}/R_{\mathrm{MCP}},$$

U_{MCP} being the bias applied over the MCP (not the entire PMT) and R_{MCP} is the internal resistance of the MCP.

The current drawn from the MCP is

$$I_{\mathrm{m}} = 16efgN_{\mathrm{pe}},$$

where e is the elementary charge, f the event rate and g the PMT gain.

To calculate the rate capability, a naive approach would be to find the event rate f at which these two currents are equal. This represents the state where the charge is barely being replenished. In reality, the gain starts to deteriorate already when 10 % of the strip current value is drawn by the multiplication process due to the lack of available electrons in the MCP [39]. The rate limit estimate therefore becomes

$$f = 0.1\frac{U_{\mathrm{MCP}}}{16egR_{\mathrm{MCP}}N_{\mathrm{pe}}}, \tag{4.3}$$

where the PMT gain g is a function of the MCP bias U_{MCP} for a given PMT piece.

From Equation 4.3 we can easily conclude the rate limit can be improved by reducing the internal resistance of the PMT. In pursuit of higher rate capability, it soon became clear that simply procuring MCP-PMTs with low internal resistance was not going to improve the situation enough. The internal resistance also has a minimal safe limit, below which a risk of a thermal runaway event is significantly elevated. The manufacturer offered to produce pieces with no less than 15 MΩ exactly for this reason.

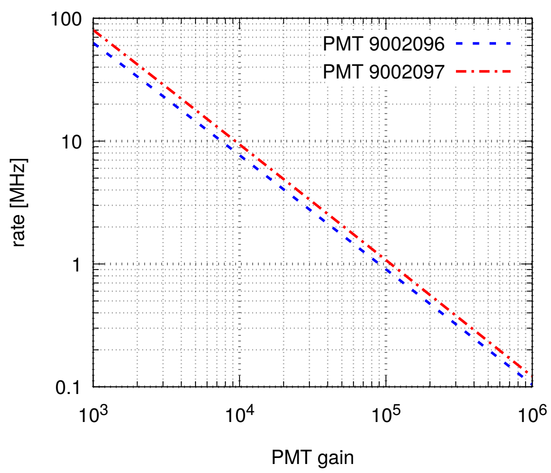

Figure 4.38: A theoretical prediction of rate capability of the XPM85212/A1-S MCP-PMTs based on Equation 4.3. The light level of $N_{\mathrm{pe}} = 20$ per channel is assumed. The internal MCP resistance of these is 36 MΩ and 29 MΩ, with the lower R_{MCP} resulting in a slightly higher rate capability, approximately proportional to the ratio of the resistance values.

Another way to improve the rate capability would be to reduce the gain of the PMT. While this would also reduce the strip current slightly due to the reduction in U_{MCP}, this change is negligible compared to the exponential nature of the gain value change. An example of the rate limit estimate is in Figure 4.38.

Rate capability – XPM85212/A1-S

In Figure 4.39 the rate capability results for the XPM85212/A1-S MCP-PMTs are plotted. The rate capability clearly improves with reductions of gain, this is however impacting the timing resolution as noise effect become more prominent.

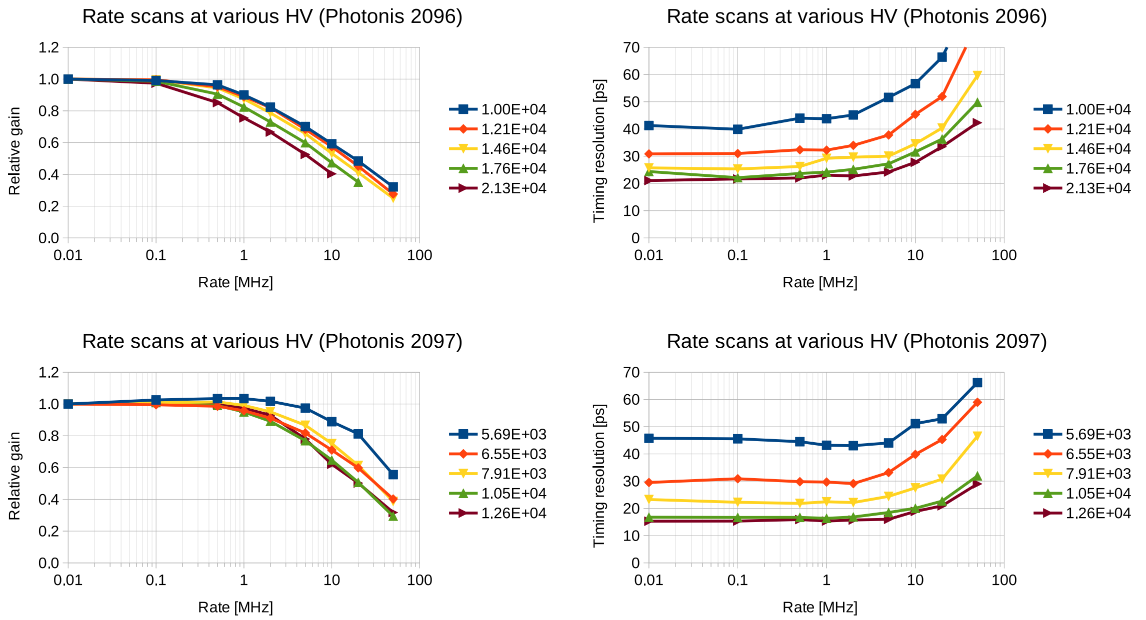

Figure 4.39: Rate scan results for two pieces of the XPM85212/A1-S with four channels illuminated (20 P_e pulses each), mimicking a ToF train, however only a $\sim$ 6 mm^2 area of each channel was exposed. The individual curves were recorded at various gains, these are noted in the plot legends. On the left the gain deterioration and on the right the timing performance results are plotted. The rate capability falls only slightly short of the predictions by Equation 4.3 plotted in Figure 4.38. These results were previously published in [36].

These measurements were performed using fibres leading the light to the individual channels, resulting in a $\sim 6\,mm^2$ area being exposed at the centre of each channel. To make conclusions about the rate capability of ToF, this needs to be corrected to the channel area of 41 mm^2, making the rate capability 6.8× higher than shown in the plots. That this can be easily done by a simple ratio is evidenced by Figure 4.40a. Even then, this is not enough for the expected 20 MHz event rates the AFP-ToF detector needs to handle during LHC Run 3. The rate capabilities measured for each PMT correspond to 1.38 $\mu A/cm^2$ and 2.38 $\mu A/cm^2$ current density for the PMT 9002096 and 9002097 respectively (taken as a density where gain drops by 20 %).

The effect of the rates is not completely local, as one could expect from Figure 4.40a. This in shown in Figure 4.40b, where one or four channels were exposed to the high rate light pulses. If the high rate induced MCP charge exhaustion was a local effect, the two curves would behave the same. This is not the case, indicating that the area near the exposed part of the MCP helps to recharge the depleted channel, an effect that is diminished when more channels or a significantly larger beam spot is used.

We can conclude the MCP charge exhaustion is not a completely global nor a fully local phenomenon. If the former were true, Figure 4.40a would show a constant rate, not a linear increase. If the latter were true, Figure 4.40b would show identical curves.

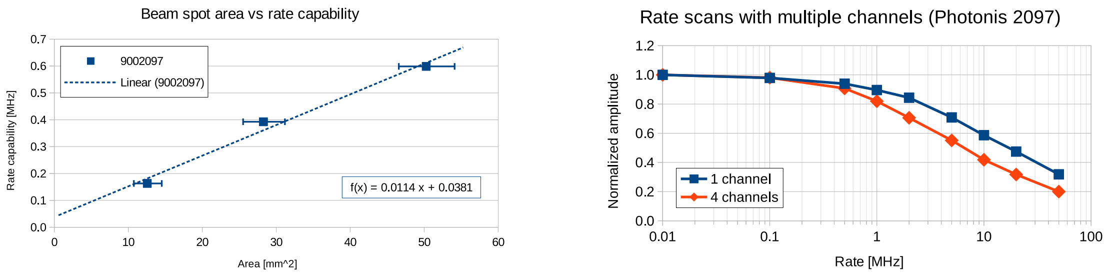

(a) (b)

Figure 4.40: Effects of the high rates when applied to various areas of the PMT. The rate capability rises roughly linearly when the area exposed is increased while keeping the total number of photons the same (a), $5.7 \cdot 10^4$ gain and 200 P_e per pulse were used here. However when more channels are connected, each exposed to the same number of photons the single channel experienced previously, the rate capability slightly drops (b), 6 mm^2 exposed area per channel and 10^5 gain with 7 P_e per pulse were used in this test. These results were previously published in [36].

Instead, Figure 4.40b shows the rate roughly halves when both the area exposed and the total light flux are quadrupled, laying somewhere between the two extremes.

Rate capability – XPM85112-S-R2D2

With the later generation of the PMTs, XPM85112-S-R2D2, the rate capability tests were repeated. While the internal resistance was not significantly reduced despite our request to do so (the novel manufacturing techniques were not yet fully understood to predict the outcome precisely), we hoped that the refined treatment of the pores would help to push the rate capability a bit further.

The measurement strategy was different here. We established the PMT gain 2000 as the lowest acceptable value giving a reasonable timing resolution, the low gain being compensated for by an additional amplification stage. Still, the four channels in the train were illuminated, this time using the channels mask instead of individual fibres. This ensured maximum relevance to our use case with a much better estimate of the illuminated area. Under these conditions, the current density necessary to reach 20 MHz with $20 - 30$ P_e per pulse was determined to be $\sim 1\,\mu$A/cm^2, a value expected to be reachable as the previous generation would have succeeded at this low gain, considering the current densities obtained were higher than this threshold.

The results of rate scans of the three pieces of XPM85112-S-R2D2 MCP-PMTs are in Figure 4.41. It is clear that the two tubes with lower internal resistance (9002199 and 9002200) are capable of handling 20 MHz rates at this low operational gain without dropping the gain to less than 80 % of the low rate reference, especially in the lower P_e scenarios more relevant for our detector. This matches the predictions given by Equation 4.3 very well (predicted $\sim$ 30 MHz limit for tube 2199). These PMTs were therefore selected for installation for the LHC Run 3 in 2021. The 36 MΩ XPM85212/A1-S tube 2096 exhibited a 20 % gain drop already at $1.38\,\mu$A/cm^2 in Figure 4.39, whereas the 2199 tested here with an almost equivalent MCP R of 35 MΩ MCP exhibits the same gain drop at $2.5\,\mu$A/cm^2. This shows the technological improvements of the double

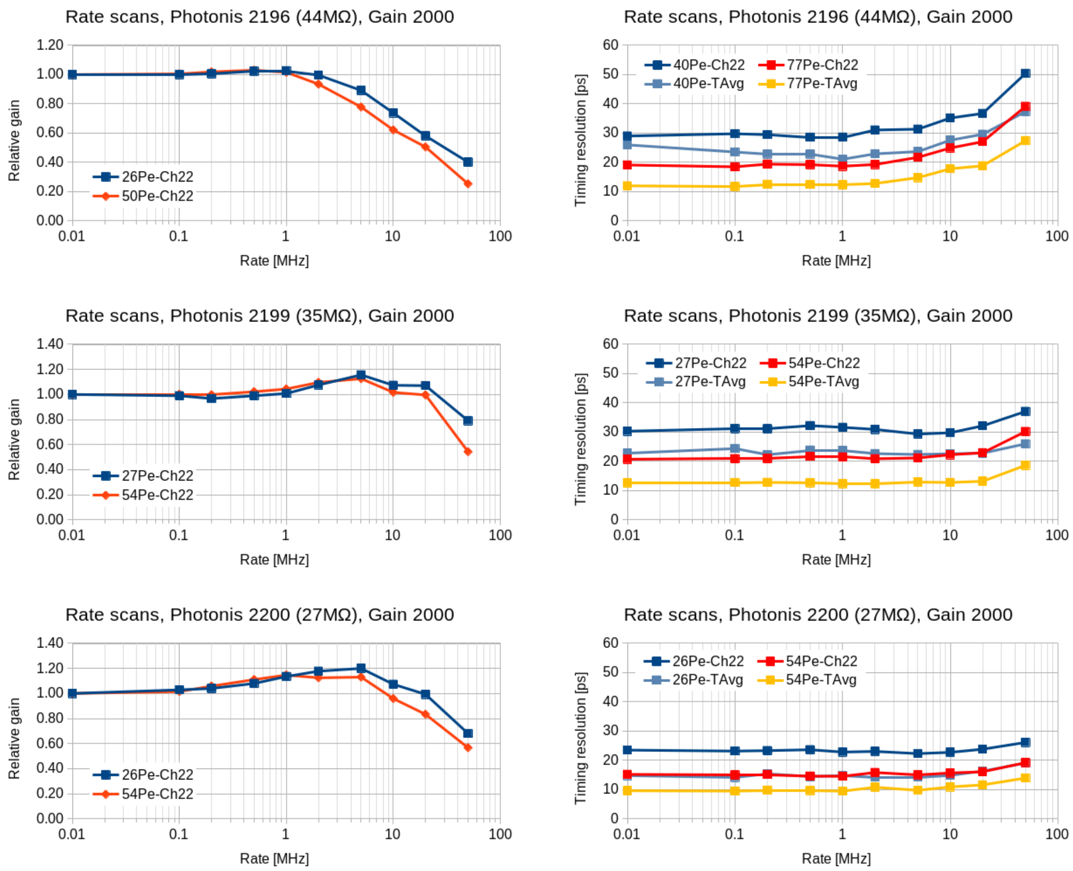

Figure 4.41: Gain deterioration and timing resolution of the XPM85112-S-R2D2 photomultipliers during rate scans with four channels exposed to the light levels noted in the legend. The TAvg timing is a train (4 channels in a row) average, relevant to our use case. 20 MHz rate of $\sim 25\,\mathrm{P_e}$ pulses in these tests corresponds to anode current of $\sim 1\,\mu\mathrm{A/cm^2}$. The rate capability is close to the predictions by Equation 4.3. These results were previously published in [37].

ALD application offer a slightly better rate capability in tubes with the same internal resistance.

For all the PMTs tested of all the variants, when the illuminated area of the channel is taken into account (it being smaller with the measurements using fibres), the rate capability results approximately match the expectations set by Equation 4.3 and Figure 4.38, while some variance exists due to differing treatment of the MCP pores. This means the predictions from Equation 4.3 are very useful to determine the expected performance. Still, actual measurements are needed to probe the exact limits before committing to use the devices in the demanding environment of the LHC. THese measurements show that operating the PMTs at the reduced gain 2000 is feasible and results in a sufficient rate capability for Run 3. This solution to the rate issue was selected as the AFP-ToF baseline.

Persistent effects of high rate exposure

In theory, the gain of an MCP-PMT would return to the original value within milliseconds of reducing the rates, this being the recharge time of the individual MCP pores. This is true for the originally used XPM85112/A1Q PMTs. With the ALD treated XPM85212/A1-S and XPM85112-S-R2D2, the situation turns out to be very different.

When we first measured the XPM85212/A1-S PMTs at high rates, it was easy to notice the gain had significantly changed even after the measurement was done and another dataset was being taken, starting at the low rates again. This was completely unexpected and prompted us to examine the phenomenon further. As it turns out, the recovery period for these PMTs is extremely long, taking several minutes for recovery to 80 % and up to a day to recover fully. The initial part of the recovery period also depends on the exposure time, with short 1 s exposure initially recovering faster before becoming indistinguishable from longer exposures. These result can be seen in Figure 4.42. The same behaviour was observed with ALD treated devices from other manufacturers as well [40].

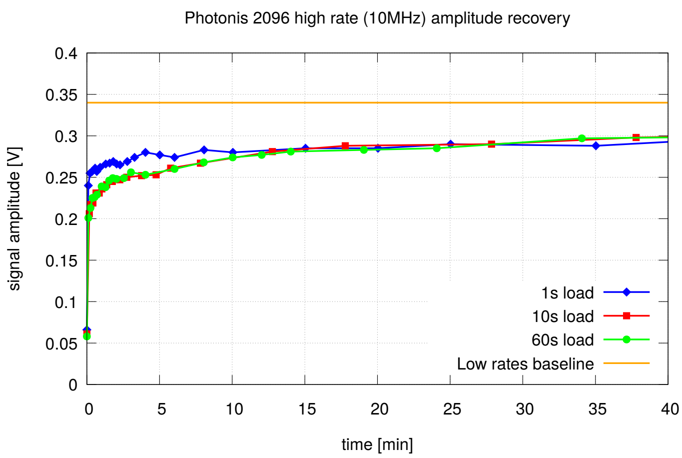

Figure 4.42: The recovery behaviour after exposing the XPM85212/A1-S PMT 9002096 to 10 MHz pulse rates of $N_{pe} = 20$ at 10^5 gain for various lengths of time. This result has been previously published in [36].

The mechanism behind this undesired long recovery behaviour could explain why the next generation of PMTs had somewhat better rate capability despite comparing PMTs with the same internal resistance. The suspicion about the cause is that charge could be being trapped below the pore treatment layer, taking an extremely long time to dissipate through the non-conductive MCP glass substrate.

The next generation, XPM85112-S-R2D2 PMTs remedy this problem. In fact, their behaviour is the opposite; after high rate exposure, the gain is temporarily higher by 20 % before returning to 110 % of the original gain within 10 − 15 min where it seems to stabilize, as seen in Figure 4.43. A very curious thing also happens if the PMT is not probed for the recovery behaviour (even with as little as 10 Hz pulses) and its HV bias is turned off instead. A complete recovery to the original gain then takes less than 30 minutes.

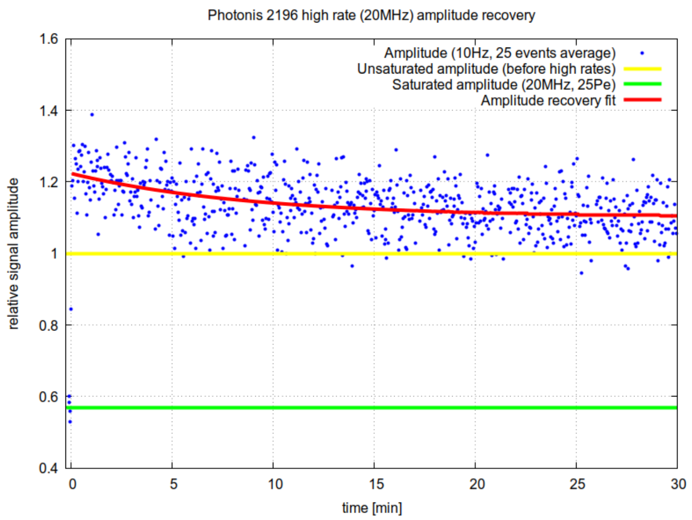

Figure 4.43: The recovery behaviour after exposing the XPM85112-S-R2D2 PMT 9002196 to 20 MHz pulse rates of $N_{pe} = 25$ at gain 2000. The laser source was switched to low rates of 10 Hz at $t = 0$. Each blue data point represents an average o 25 pulses in order to aid plot clarity. This result has been previously published in [37].

4.6.9 PMT operation in a vacuum / low pressure environment

Operating a high voltage device under reduced pressure is inherently risky and requires additional precautions.

While a very high vacuum would be fine in terms of high voltage sparks or corona formation risk, the AFP pots contain only a secondary vacuum maintained by ordinary rotary pumps. The secondary vacuum in the AFP Roman Pots is usually at a level of few tens of millibars. This lands us near the worst area in terms of high voltage conduction of the low density air over distances of many centimetres. The relationship between the pressure and high voltage discharge reach is in Figure 4.44.

The main issue is that there has to be a high voltage connection inside the pot that also has to be possible to disassemble without cutting the cables every time. A solution of a vulcanizing rubber seal was devised, but the reliability of it was not great, as seen in Figure 4.45.

Another issue was the PMT body itself. While it is theoretically possible, there is no guarantee for successful PMT operation in a vacuum by the manufacturer. This was a significant weak point of the original AFP-ToF design. For this reason, the PMTs went through a vacuum test depicted in Figure 4.46. Even then, some PMTs would eventually end up failing, tripping the current limiter on the HV supply with the discharge. One such failed PMT is again in Figure 4.45.

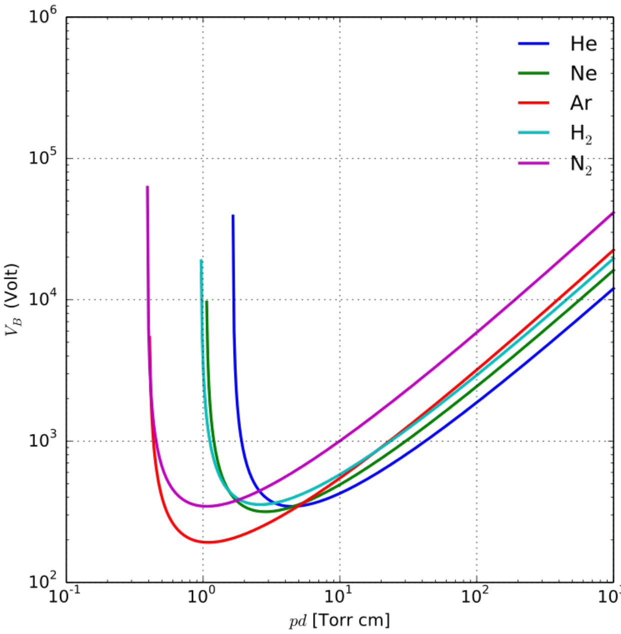

Figure 4.44: Paschen curves for various gasses. Lowering the pressure results in easier sparking of high voltage, an effect that is only reversed when reaching very high vacuum levels where not enough air molecules are available for the process. Image source: Wikimedia Commons, CC BY-SA.

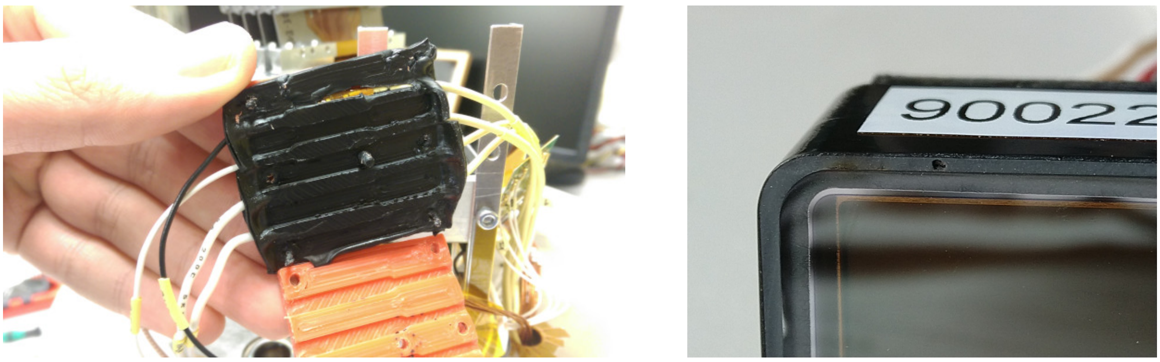

Figure 4.45: The HV vacuum insulation when disassembled (left) shows one of the lines is not sealed in the vulcanizing rubber properly. In this case, we were lucky it was the grounding line, if it was one of the other lines carrying high voltage, the HV vacuum tests would fail and the laborious sealing process would have to be repeated. The image on the right shows a defect in the delicate PMT silicone seal, leading to failing a vacuum test.

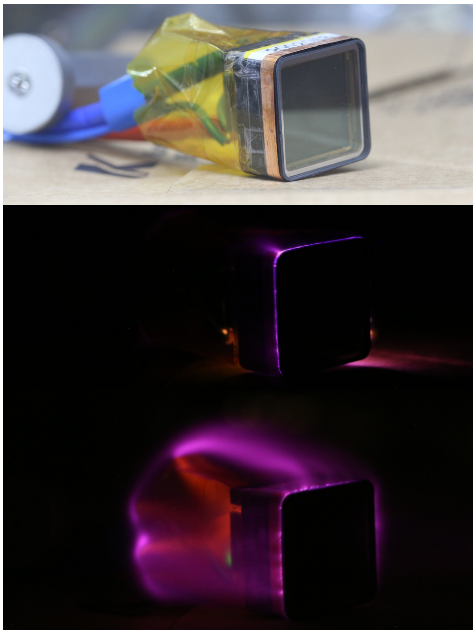

Figure 4.46: A corona produced during the vacuum tests of the PMT high voltage insulation. For safety of the device, all the PMT stages were grounded. At the top, a thin copper sheet can be seen wrapped around the PMT body near its front face, mostly covered with kapton insulation extending well beyond the PMT back side. In the middle and bottom images, a corona is forming with the decreasing pressure in the chamber as the copper sheet is biased at high voltage. The shape of the corona shows how the electric field lines are forced around the kapton insulation to reach the ground pins, proving the insulation at the front face of the PMT works as intended – no corona is seen anywhere at the PMT front face despite a much shorter path to ground than around the kapton insulation.

We were determined to find a commercially available solution for the high voltage connection in a vacuum. However the trouble with the vacuum (also of the PMT body itself) was so pervasive that a change of course was decided and a more comprehensive solution of the issues with high voltage was eventually implemented in the form of the "Out-of-vacuum" redesign of the RP flange and ToF mounts. This redesign and its other benefits are described in the following section 4.7.

4.7 Out-of-vacuum redesign

The Out-Of-Vacuum (OOV) design is a significant overhaul of the way ToF is implemented at the mechanical level.

4.7.1 Motivation for redesign

The primary objective is to move the PMT out of the RP vacuum, but the redesign also impacts many other aspects like signal feed-through and serviceability.

The main advantages of the OOV solution are:

- All HV elements are removed from the risky vacuum environment inside the pot, as discussed in subsection 4.6.9.
- No need for signal feed-through on the suboptimal flat flex cables,
  - improving signal quality and strength – the feed-through flex was impedance mismatched, getting rid of it means removing source of signal attenuation and reflections,
  - removing a problematic flex connection with few design duty cycles, where contacts were susceptible to oxidation and not well suited to carry the significant current needed for PAa powering,
  - reduced interference pick-up on a coaxial cable compared to the hard to shield flat flex.
- Easier access to the PMT and PAa first stage amplifiers, allowing their replacement without opening the pot and breaking the secondary vacuum in the process. This allows for PAa or entire PMT replacement even during a short LHC technical stop lasting only a few days.
- Room for PAa simplification, moving to in-line single channel ones integrated into the signal cable. Details are described later in section 4.9.
- Better cooling of the PMT and PAa channels, as they are now exposed to air and don't rely on heat conduction through the holder material only.
- Allows for a straightforward implementation of an artificial light source (pulser) for testing purposes, as discussed in section 4.12.
- Improved and much simplified ToF alignment procedure.

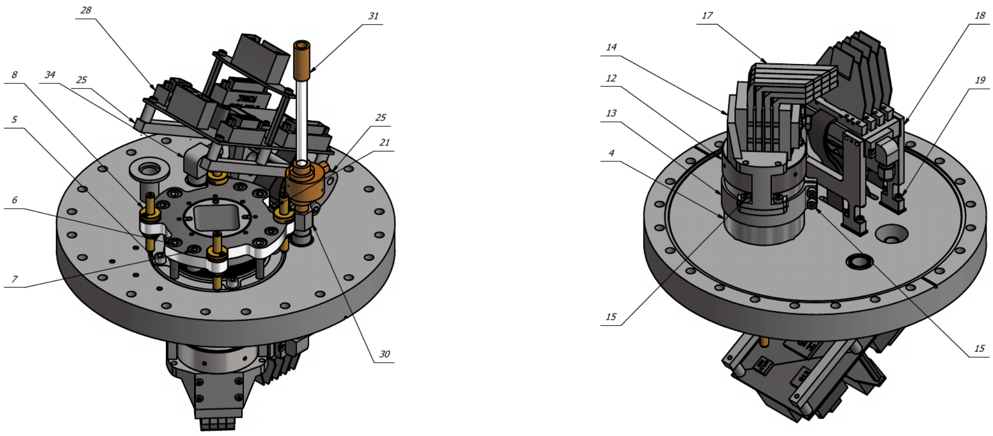

(a) (b)

Figure 4.47: The out of vacuum mechanical design, showing the pot outside (a) and inside (b) faces of the AFP flange.

4.7.2 Description of OOV mechanical implementation

The OOV redesign features a steel tube that protrudes through a new large circular hole in the AFP flange, as shown in Figure 4.47. The tube houses the PMT and ends with a glass window, above which the ToF bars are mounted. The window must be able to endure the pressure difference as it separates the secondary vacuum from the outside environment. It also features an anti-reflex coating optimized for the appropriate wavelengths to minimize reflection and maximize optical signal transmission from the bars to the PMT.

To maintain vacuum tightness while allowing for movement of the tube for alignment purposes, steel bellows are used. Alignment is performed with a set of precision fine thread screws at the outside face of the flange. A cross-section diagram and a photo of the OOV variant of AFP is in Figure 4.48.

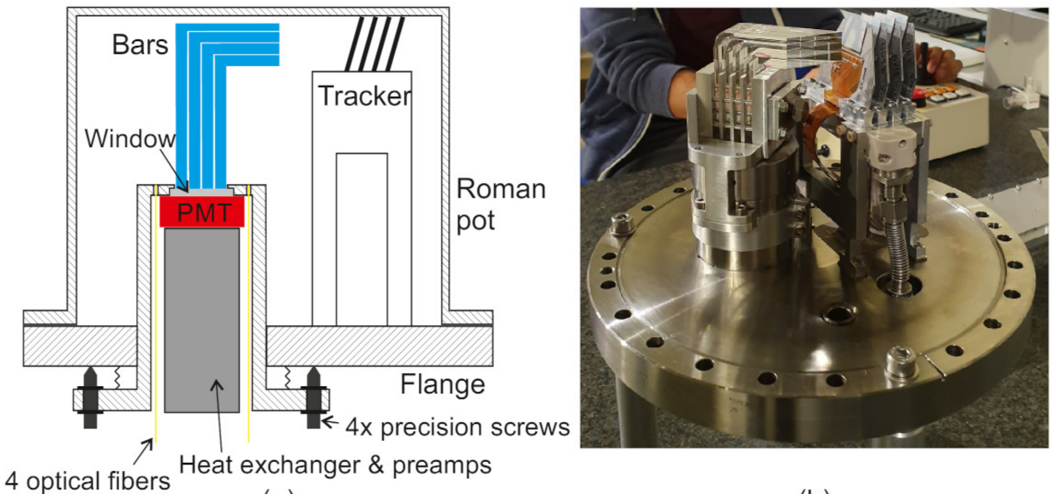

(a) (b)

Figure 4.48: A cross section of the OOV ToF mounting tube (a) and a photo of the AFP flange with all parts mounted using the OOV mechanical design (b). This figure has been previously published in [34].

In the OOV tube, the PMT is placed and pressed against the glass window with a special insert we call the heat exchanger. A heat conductive pad is installed at the back of the PMT, enabling better heat transfer to the heat exchanger. Similarly, the PAa single channel amplifiers are placed in special cutouts in the heat exchanger, facilitating heat rejection. Four optical fibres can then be used for delivering an external testing optical signal through the separation glass. A detail of the way the PMT is mounted is in Figure 4.49.

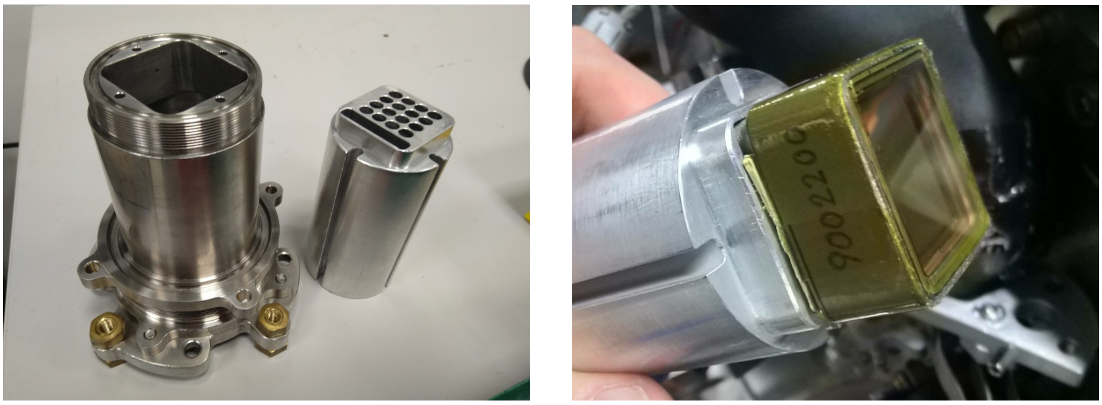

(a) **(b)**

Figure 4.49: The ToF mounting tube with the heat exchanger (a) and the PMT mounted on the heat exchanger (b). The top of the mounting tube does not have the separation glass installed here, showing the four channels enabling delivery of a testing optical signal via fibres. The heat exchanger is keeping the PMT in place and features cutouts for the PMT HV connection and the individual PAb channels on the signal cables as well as for the fibres running along its length.

4.7.3 Performance impacts of OOV ToF variant

The OOV ToF setup has major implications for both the optical and electrical signal paths, making the former more complicated while significantly improving the latter.

The presence of the glass separator window causes a $13 - 15\,\%$ signal amplitude drop (beam test results being the exact match of simulation), but compared to the previous ToF variant, there is not a significant change in the output signal amplitude – the slight optical loss is mostly compensated by the removal of the sub-optimal flex feedthrough cables. Efficiency is not much affected by the presence of the glass either, as is timing resolution.

The OOV has many advantages on the signal path from the PMT. The removal of the flex feedthroughs and the interconnection boards at each end of it means there is much less opportunity for interference to enter the system. While the effect of this on timing was not evaluated in a way that would allow a direct comparison, a cleaner and better shielded signal path is easily assumed to have a positive impact on timing.

The removal of interference pickup weak points and enabling of better shielding of the signal path was also one of the enabling factors to introducing the third amplification stage and lower gain PMT operation, necessary steps to operate the PMTs at the higher detection rates. This would carry a significant timing performance impact with the original ToF design due to the added noise, something that is in large part mitigated here.

4.8 PMT HV divider

As we decided to operate the PMTs at a rather low gain (~ 2000), a peculiarity arose. Due to the nature of classic resistive dividers, not only the MCP voltage (and therefore gain) changes with the supplied voltage, but the front and back stage (PC – MCP input, MCP output – anodes) voltages change proportionally as well. This means other characteristics than gain (efficiency, timing resolution) may be impacted.

An experimental HV divider incorporating zener diodes was prepared that allowed to set the front and back stage voltage independently using interchangeable modules. This divider with the individual modules is in Figure 4.50.

Figure 4.50: The experimental HV divider with the set of interchangeable modules laid out. The modules are inserted in the "PC" and "Anode" marked slots to determine the bias values at the front and back PMT stages. The MCP bias can be determined by subtracting these from the total bias.

4.8.1 Front stage – gain, efficiency and timing resolution

The first important observation was an impact of the front stage voltage on the overall gain, even while the MCP voltage was fixed. At a higher front stage bias, the first photoelectron hit in the MCP (with higher energy) probably generated more secondary electrons, increasing the gain. Another observation was an improved detection efficiency up to 20 % higher, measured by incidence of single photon detection (starting at 5 % incidence as typically used for TTS measurement, reaching 6 % at higher front stage voltages). The timing resolution was also noticeably improved, as much as by 10 %. The results are in Figure 4.51. These effects were present (with unchanged magnitude) even when the front stage voltage induced gain increase was properly compensated by decreasing the MCP voltage (to obtain a fixed overall gain). Rise time was not measurably impacted by the front stage voltage.

4.8.2 Back stage – gain, timing and rise time

As Figure 4.52 shows, the back stage voltage had a slight impact on the gain, but only very marginally influenced timing with the measurement uncertainty mostly obscuring

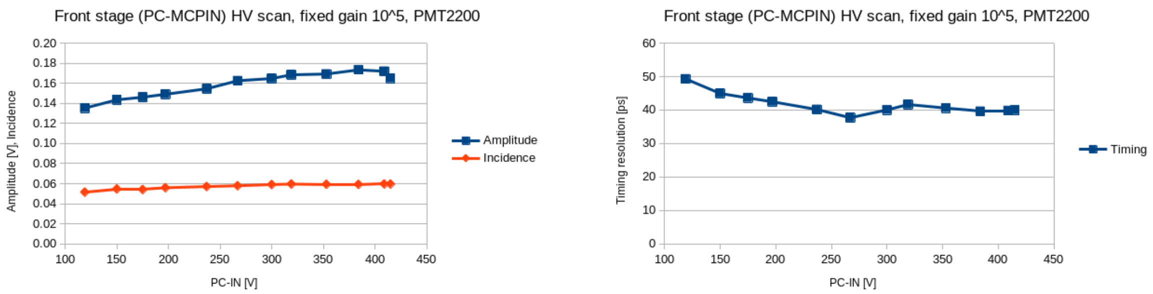

Figure 4.51: Impact of the front stage voltage on single photon events. The observed variables are the pulse amplitude (left), signal incidence (left) and timing resolution impact (right). The y axis in the plot on the left denotes the amplitude in Volts for the blue curve and the signal incidence factor (rate of single photon detection) for the red curve.

the effect. The rise time was reduced very slightly (1 %), but unlike with timing, even these minuscule rise time changes show very clean dependence on the back stage voltage.

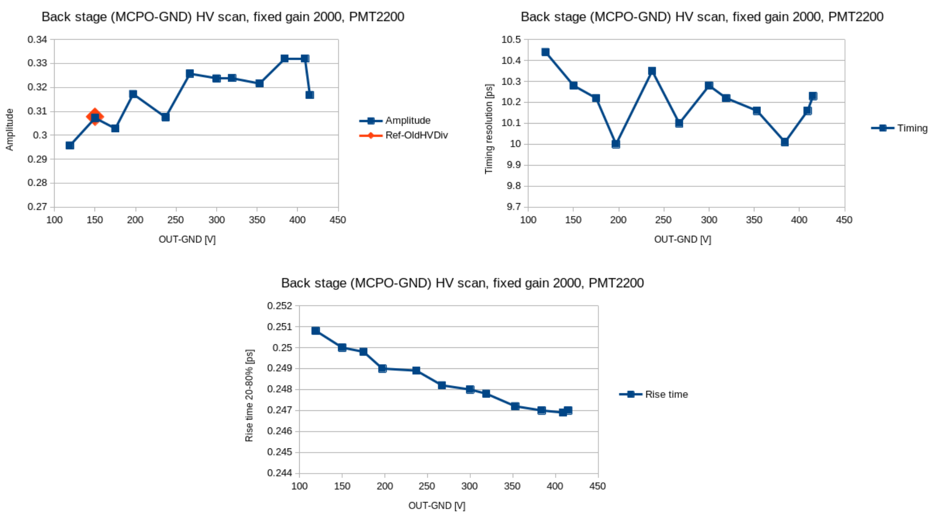

Figure 4.52: The influence of back stage voltage on signal amplitude, timing resolution and rise time.

4.8.3 Back stage – crosstalk (charge sharing)

The next aspect studied was the impact of the back stage voltage on crosstalk, especially the kind caused by charge sharing. A mask mimicking the ToF bar shape was used and the direct neighbours to the illuminated channel as well as a channel far away were monitored. The mask and layout of the channels measured is in Figure 4.53, the measurement style is the same as previously in subsection 4.6.7.

The results of the measurement are in Figure 4.54. A difference between the normal and the reduced anode gap PMTs is natural, as well as more crosstalk inside train as opposed to across trains (thinner/thicker gaps between the illuminated areas). What was surprising was that with the standard gap, the crosstalk was actually slightly increasing as the back stage voltage rose (the expectation was the opposite due to

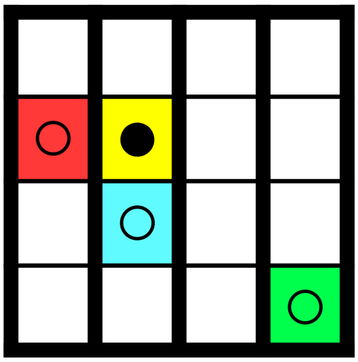

Figure 4.53: The layout of observed channels during crosstalk measurements. All the channels that are observed are marked with a circle, while the sole channel also illuminated with a filled circle. This is the same layout as in the crosstalk measurements in subsection 4.6.7.

better potential focusing of the electron shower from a pore), while with the reduced gap there was almost no change, only a very small decrease in case of the in-train crosstalk.

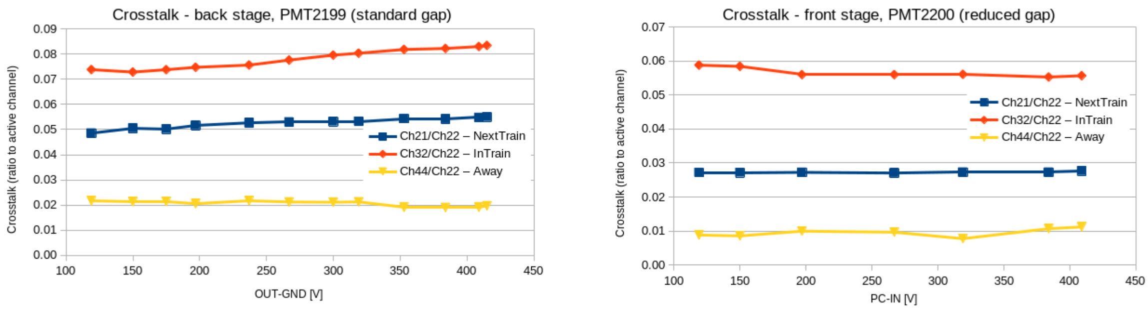

Figure 4.54: Results of crosstalk measurements with standard and reduced anode gap PMTs when the back stage bias is varied.

4.8.4 Rate capability impact

As could be expected, the rate capability is only impacted by the change in gain – if compensated for by a slight MCP bias decrease to keep the overall gain fixed, the rate capability remains the same, as can be seen in Figure 4.55. The blue curve almost entirely covers the yellow one, showing that there is no impact on rate capability in such a scenario.

4.8.5 Gain curve impact

The compound effect of the front and back stage bias increase on gain was studied more closely by taking full gain curve measurements seen in Figure 4.56. The modified divider behaves almost exactly the same as the old one when equivalent front and back stage voltages of 150 V are set, with increased gain when the front and back stage are set to 300 V (especially in the low HV range, where the insufficient front stage voltage impacts gain more).

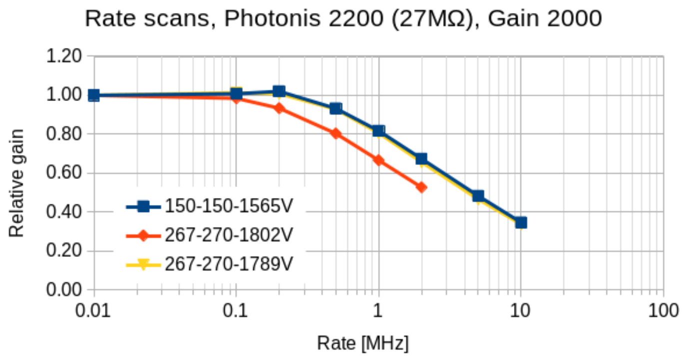

Figure 4.55: Rate scans comparison of the modified divider – old divider configuration (blue), increased front and back voltage (red) and increased front and back voltage with gain compensation (yellow).

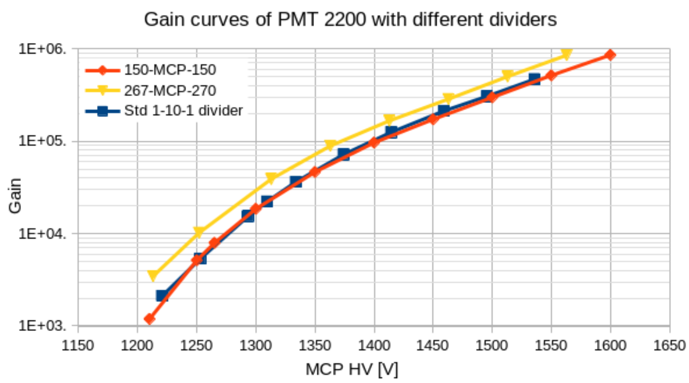

Figure 4.56: Gain curve measurements using the old divider (blue), the experimental divider with setting equivalent to old divider (red) and the experimental divider using elevated front and back stage voltage (yellow). To allow a good comparison, the MCP bias voltage is plotted on the x axis instead of the overall bias voltage.

4.8.6 Final HV divider implementation

The final HV divider to be used is the traditional resistive design (due to radiation hardness concerns of the zener diodes), but with a modified ratio of 1:3.4:1 to yield $\sim$ 300 V on both front and back stages under the expected operational HV. This is well within the maximum allowed gap voltage of 500 V as declared by the manufacturer.

4.9 Amplifiers

4.9.1 PAa

With the out-of-vacuum redesign and removal of the signal feedthrough, an opportunity arose for simplification of the first stage amplifier. Instead of the small board with four channels, the PAa was redesigned to be included inline on the individual coax cables leading directly to PAb input, as shown in Figure 4.57. The amplification element is unchanged, still using the GaAs MMIC amplifier PSA5043. The powering was adjusted, reducing the 5 V bias from the PAb input to 3.3 V. The individual amplifier channels have a metal housing each, offering both much improved shielding from interference and heat dissipation capability through the much increased surface area.

Figure 4.57: The new inline PAa. The MMCX connector plugs directly into its counterpart on the new PMT backend design, as described in section 4.6.

Experimental transimpedance PAa modules

An experimental transimpedance variant of PAa was tested, using the SiGe transistor BFR840. A transimpedance amplifier acts as a current to voltage converter, not relying on a load resistor [41]. It is created when an operational amplifier negative input is connected to its output with a feedback resistor while the positive input is grounded. The current impulse is then applied to the negative input. A feedback capacitor is included parallel to the resistor in order to improve the stability of the amplifier.

The value of the feedback resistor is of a paramount importance and needs to strike a delicate balance between gain and frequency response. The supply voltage to the operational amplifier also modifies the behaviour. For this reason, an extensive set of tests was performed to scan this parameter space and find optimal values. The results are in Figure 4.58 and Table 4.2, showing gain and timing performance. The values are relative to the standard PAa performance, which was performed as a reference measurement.

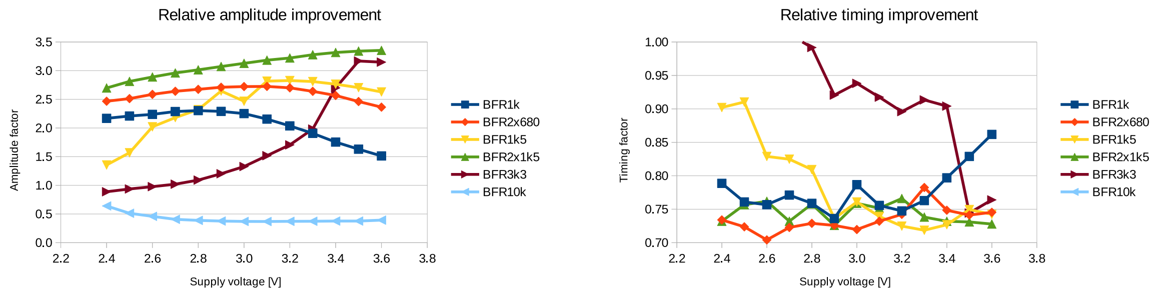

Figure 4.58: Results of the parameter space scan of the transimpedance amplifiers as plots of gain and timing performance. The gain and timing is relative to the traditional PAa.

Amplitude relative

Voltage \ R	BFR1k	BFR2x680	BFR1k5	BFR2x1k5	BFR3k3	BFR10k
2.4 V	2.17	2.47	1.35	2.70	0.89	0.64
2.5 V	2.21	2.51	1.57	2.81	0.94	0.51
2.6 V	2.24	2.59	2.02	2.89	0.98	0.46
2.7 V	2.29	2.64	2.18	2.96	1.02	0.41
2.8 V	2.30	2.67	2.32	3.01	1.09	0.39
2.9 V	2.29	2.71	2.65	3.07	1.20	0.38
3.0 V	2.25	2.72	2.47	3.13	1.33	0.37
3.1 V	2.16	2.72	2.82	3.18	1.52	0.37
3.2 V	2.04	2.70	2.83	3.22	1.71	0.37
3.3 V	1.91	2.64	2.81	3.28	1.98	0.37
3.4 V	1.75	2.57	2.76	3.32	2.70	0.38
3.5 V	1.63	2.46	2.70	3.34	3.17	0.38
3.6 V	1.51	2.36	2.63	3.35	3.15	0.39

Timing relative

Voltage \ R	BFR1k	BFR2x680	BFR1k5	BFR2x1k5	BFR3k3	BFR10k
2.4 V	0.79	0.73	0.90	0.73	1.14	2.31
2.5 V	0.76	0.72	0.91	0.76	1.07	2.83
2.6 V	0.76	0.70	0.83	0.76	1.07	2.20
2.7 V	0.77	0.72	0.82	0.73	1.01	2.19
2.8 V	0.76	0.73	0.81	0.76	0.99	2.13
2.9 V	0.74	0.73	0.74	0.73	0.92	2.18
3.0 V	0.79	0.72	0.76	0.76	0.94	2.25
3.1 V	0.76	0.73	0.74	0.75	0.92	2.24
3.2 V	0.75	0.74	0.72	0.77	0.90	2.20
3.3 V	0.76	0.78	0.72	0.74	0.91	2.19
3.4 V	0.80	0.75	0.73	0.73	0.90	2.13
3.5 V	0.83	0.74	0.75	0.73	0.74	2.14
3.6 V	0.86	0.75	0.74	0.73	0.76	2.08

Table 4.2: Results of the parameter space scan of the transimpedance amplifiers as tables of gain and timing performance. The gain and timing is relative to the traditional PAa. The colour coding in the header corresponds to the data series colouring in Figure 4.58.

The transimpedance PAa clearly performs the best in terms of gain with feedback resistor implemented as a series of two 1k5 resistors, reaching over 3× the gain of a traditional PAa and about 25 % better timing. The timing performance is then only slightly better in case of two 680 Ω resistors, for the price of a slightly lower gain. The supply voltage under extended operation is then better kept within the lower values for thermal management reasons. The data gathered allows to strike a balance between these requirements.

As the approach was highly experimental and not properly validated on a beam test, with the radiation hardness of the BFR840 being unknown to us, this PAa implementation might serve as a future upgrade but was not selected as the baseline for the AFP installation for Run 3. The traditional PAa amplifiers, albeit in the new form factor, were used instead.

4.9.2 PAbc

The second stage amplifier PAb was also significantly modified. The PAa power supply bias on the input was reduced to 3.3 V as mention above, but the most significant change was the integration of a third amplification stage, necessitated by reduced PMT gain as described in subsection 4.6.8. This is in principle another PAb GaAs amplifier ADL5611. As each amplification stage is inverting, an inverter circuit following the third stage also had to be included to keep the negative signal polarity expected by CFDs. We call these amplifiers PAbc, signifying the inclusion of the third (c) stage compared to the previously used PAb. The PAbc modules are shown in Figure 4.59.

The PAbc module also gained remote control capability for the attenuation levels.

Figure 4.59: A pair of PAbc NIM modules. Note the change to MMCX connectors at the input and the I^2C connection at the top.

Those were previously set manually, here a switch selects local and remote control. Similar to CFD thresholds, the attenuation levels are set by the HPTDC over I^2C communication line.

Another modification of the PAbc compared to PAb is the inclusion of an analogue filter with cutoff frequency of 1.4 GHz intended for noise rejection.

Amplifier saturation

Based on tests with way too high PMT gain, the amplifiers start exhibiting saturation effects with output pulses higher than 1.8 V. Stronger pulses than that still get through, but are increasingly distorted and flattened, resulting in a drift of the timing information as shown in Figure 4.60. In this case, PAc was saturating, but PAb in the original design behaves the same as it is the same amplifier.

The PMT gain in Figure 4.60 was set way too high, resulting in significant saturation effects of the PAc, influencing the stronger pulses and reducing their ultimate amplitude. For this reason, the timing drifts to earlier timestamps as the CFD timing is obtained when the edge crosses a set fraction of the peak height, as explained in subsection 3.5.2. The opposite drift at low amplitudes is caused by crosstalk within the PMT, this was explored in subsection 4.6.7 and is normally cut off by setting an appropriate CFD threshold.

For this reason, it is important not to set the PMT gain too high. This would normally be done based on gain curve measurements and beam test HV tuning. Fortunately, an upgrade of the CFD modules allows us to get some limited information of the pulse amplitudes, as will be discussed in the next section. This allows to keep the risk of both saturation and too low gain (reducing SNR) under control.

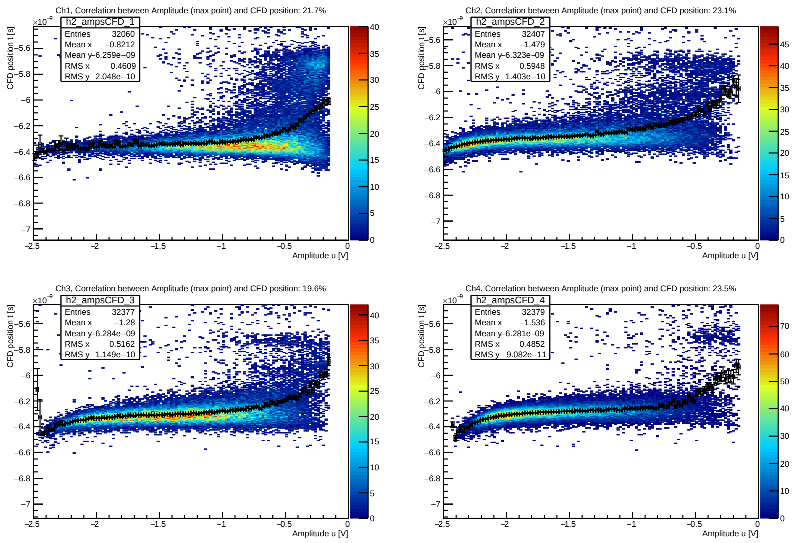

Figure 4.60: Correlation plots of signal amplitude and the timing measurement obtained by recording the raw signal. The four plots represent the four bars in train 4. The saturation effect shows up as a timing drift at high amplitudes.

4.10 CFD

The CFD modules were significantly updated. The physical distinguishing factor is the absence of the physical wire loop present on the underside of the daughter boards. The electronic circuit was optimized to deliver a slightly better timing, implementing compensation for the slight non-linearities in the PMT pulse behaviour. Nevertheless, it is the novel behaviour of the output signal that is the most interesting part.

4.10.1 Pulse length

A new important capability was implemented in the updated CFD modules – variable pulse length based on input signal amplitude. This will allow the TDC to record the approximate amplitude of the raw signal for a given event, simplifying tuning and troubleshooting at the LHC where we cannot hook up an oscilloscope for debugging during a run.

While some approximate predictions of how the pulse length should behave were available from the designer, it is important to accurately measure how the pulse length depends on the input pulse amplitude, but also the CFD threshold. This was performed by running the signal through a splitter and recording one branch directly while feeding the other to the CFD and recording its output. To maximize the number of channels recorded during one measurement, two oscilloscopes were used in a tandem setup, offering 4+4 channels. Therefore four CFD channels were tested at once. A correlation plot of the results with the appropriate fits is in Figure 4.61.

As expected, there are some small variations among the individual CFD boards. Fortunately, the dependence on the amplitude is nicely linear, the same applies to the threshold value. Using the fits of the four randomly selected CFD channels and performing the same measurement at multiple various threshold values, we determine the Equation 4.4 as the function for calculating back the amplitude of the input signal from the pulse length ToT and the CFD threshold $\mathrm{Thr}_{\mathrm{CFD}}$.

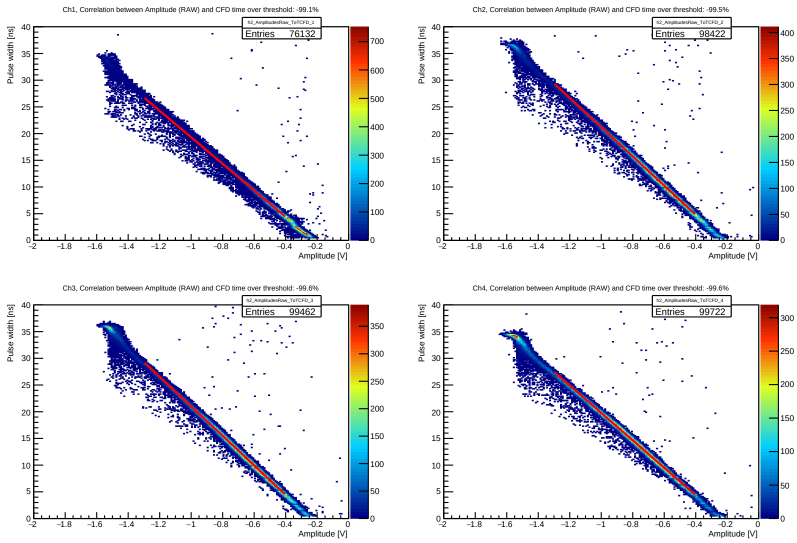

Figure 4.61: Correlation plots of pulse amplitude and the CFD pulse length for four individual channels. The fits are used as one of the inputs to determine the transfer function in Equation 4.4.

$$\text{Amplitude}\,[\text{V}] = 0.0522 + 0.877\text{Thr}_{\text{CFD}}\,[\text{V}] + 0.0379\text{ToT}\,[\text{ns}] \tag{4.4}$$

Validation plots of the function in Equation 4.4 being used to determine the pulse amplitudes, in the form of an amplitude histogram comparison and the event-by-event difference histograms, are in Figure 4.62. The uncertainty is $15 - 20\,\text{mV}$ (event-by-event precision) with up to $20\,\text{mV}$ offset (accuracy) of the peaks, a great result for amplitude tuning based on the CFD pulse lengths.

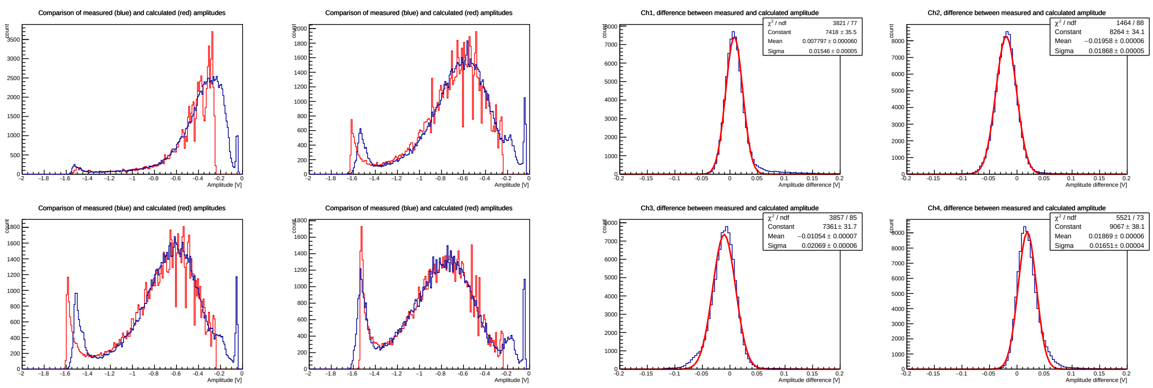

(a) **(b)**

Figure 4.62: Comparison of original and reconstructed amplitude histograms (a), with the original in blue and reconstructed in red. Histograms of the reconstruction error for all events are in (b).

4.10.2 CFD fraction optimization

The CFD fraction has a major impact on the timing resolution obtained. While the setting of 50 % is a sensible default where no further information is available, a better fraction could exist depending on the pulse shape (the best results are typically obtained when triggering in the steepest part of the pulse edge). The hardware CFDs are hard set for 42 % based on prior tuning during their development, but the software CFD could be easily modified to any fraction value.

An optimization scan of the CFD fraction was therefore performed. This was done by repeatedly running the analysis package with the software CFD implementation (included in Appendix A) over test data, varying the CFD fractions in each run and observing the resulting timing resolution in the CFD timing histograms. The full range of 1 % – 99 % fractions with 1 % increments was evaluated. The data used for this were obtained at the October 2016 beam test of the ToF prototype.

The plot of the results in Figure 4.63 shows that neither too low or too high fractions are good for timing, suffering from low slope and noise pickup as expected. The fit of the data near the best resolution area yields 42 % as the most optimal CFD fraction value. This confirms via software CFD that the 42 % fraction chosen during the hardware CFD development is the best fraction in terms of timing resolution[1]. No changes were therefore proposed in this regard.

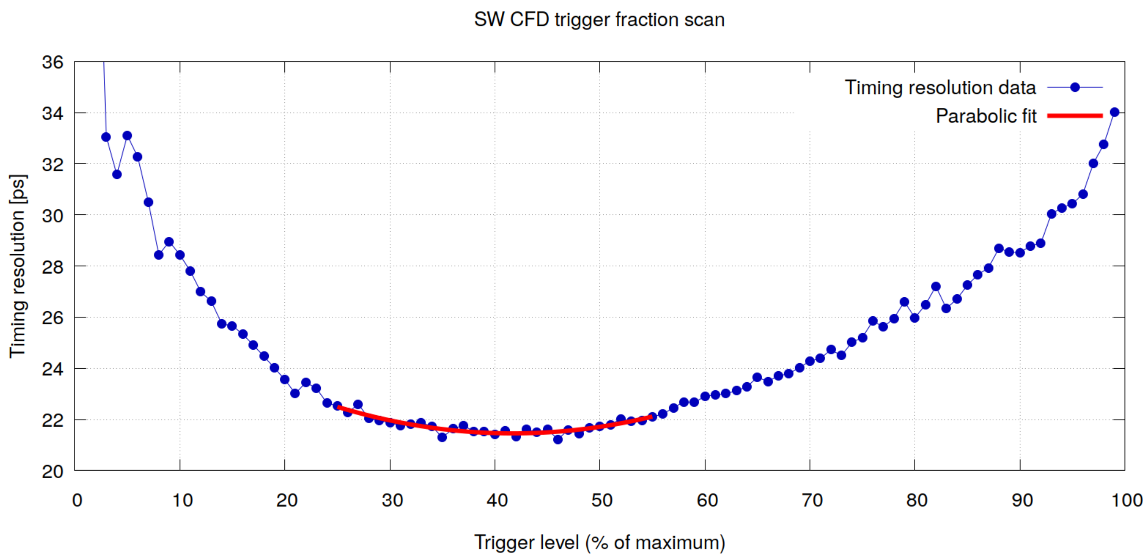

Figure 4.63: Software CFD fraction tuning. A set of ToF beam test data was analysed many times using variable CFD fraction and the obtained timing resolution was plotted. The minimum of the local parabolic fit, therefore the most optimal CFD fraction in terms of timing resolution, is at 42 %.

[1]Not surprising at all, since “42” is known to be the Answer to the Ultimate Question of Life, the Universe, and Everything [42]. Lucky for us, this optimization routine took about 1 hour to complete, not 7.5 million years.

4.11 Digital Trigger Module

The digital trigger module (DTM) [43] is a new module that acts as a bridge between the CFD and HPTDC. A previous version, the Analogue Trigger Module, was developed prior to DTM but was not deemed suitable for use with AFP-ToF due to its shortcomings. The DTM resolves the issues encountered in the analogue version. The purpose of the module is to set a qualification criteria on the input signal before transmitting them on the output and generating a trigger impulse sent over the air-core cable to ATLAS Central Trigger Processor (CTP). The DTM front panel is in Figure 4.64.

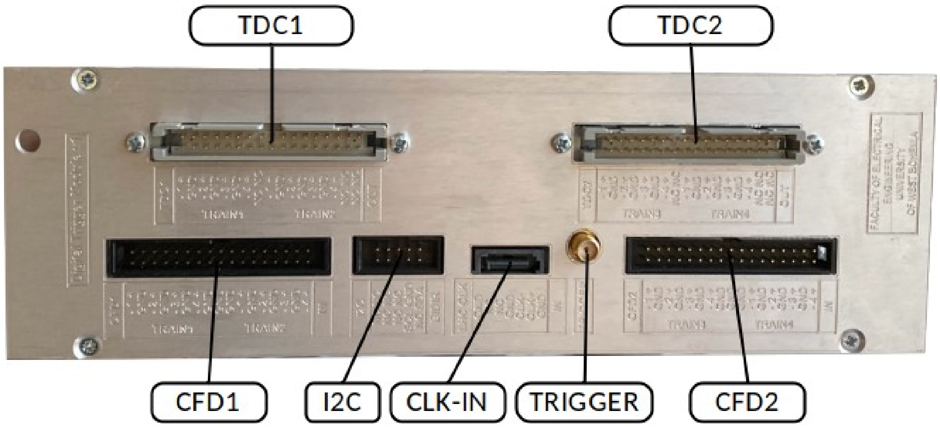

Figure 4.64: DTM front panel with the connectors marked. Image credit: [43].

The trigger condition is the minimum number of the four bars in each ToF train that have to fire simultaneously (within the same LHC bunch crossing window). If the condition is not satisfied, the trigger pulse is not generated. As an additional feature, the individual channel signals of each given train are not passed through when the trigger condition is not satisfied – this helps the HPTDC with its limited bandwidth not to be congested by signals that are not of interest. Each train is processed independently in this regard.

The DTM is one of the options of trigger source the AFP system can use. The other two are HPTDC trigger (deprecated) and SiT trigger. The DTM trigger is preferred under ordinary conditions whenever ToF is operational. A block scheme of the AFP-ToF system with the trigger module in place is in Figure 4.65.

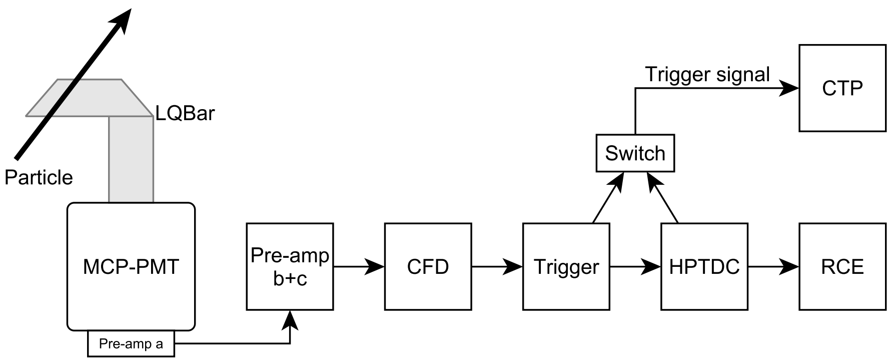

Figure 4.65: A block scheme of ToF with the DTM included.

The DTM can encode a data frame in the trigger output, this can be used to signal which trains of the detector have triggered. The data frame consists of a start bit and then four subsequent bits each marking a trigger in one of the four ToF trains. An appropriate trigger decoder must decode this data frame at the other end of the air-core cable before forwarding the information further. If the decoder is not present or encoding is not desired, this functionality can be disabled in the DTM via I^2C configuration sent by the HPTDC and a simple trigger pulse is sent instead. I^2C is also used to set the trigger condition.

The more detailed information contained in the data frame can be used to construct a more elaborate trigger menu, for example having special trigger items for cases where the same trains trigger on each side, meaning detection of protons with a roughly similar energy loss. These special cases could then have for example a lower pre-scale.

The DTM uses an FPGA to control the trigger logic and facilitate the I^2C communication. The FPGA used is IGLOO2 by Microsemi. More details about the DTM can be found in [43].

4.12 Laser Diode Pulser

A module with four diode lasers of an appropriate wavelength (405 nm) was implemented for testing purposes. The light from those is distributed through optical fibres and directed through special channels around the PMT and onto the separation glass window of the OOV tubus, where they partially distribute throughout the glass window and partially illuminate the inside of the pot. The light pulses are then seen by all the PMT channels, albeit with variable intensity.

The pulser is intended for simple testing of signal path of all the channels, but cannot be currently used for more detailed analysis like PMT gain change monitoring. This is due to the unknown rate of radiation-induced deterioration of the fibres used for the pulser light and of the laser diodes themselves.

4.13 Time to digital converter

4.13.1 HPTDC

The HPTDC boards installed in 2017 suffered from numerous SEU (single event upset) and resets in the FPGA unit. A SEU is typically caused by a charged particle flipping a bit in an electronic device, causing a failure in the programming instructions. While robust solutions for this problem exist,[2] they are way too expensive.

Shielding options of the ToF crate at the LHC were explored without any significant success.

A sufficient alternative solution was eventually found for our case. The originally used Cyclone IV FPGA by Altera was replaced by IGLOO2 by Microsemi (the same FPGA the DTM uses). While the replacement FPGA cannot be classified as rad-hard by any means, it is significantly more radiation tolerant than the Cyclone IV. Such

[2] A typical example of a radiation hardened computation hardware are the RAD series computers typically used in satellites and spacecraft. They feature node sizes of hundreds of nm, making the bits more difficult to flip. Another notable hardening feature is redundancy, for example with three cores performing the computation, checking each other through a majority vote mechanism on the result.

difference is typically caused by node size and other architectural differences of the silicon hardware.

As a result, the new HPTDC board implementation suffers much fewer SEU or other radiation induced issues and is also capable of recovery from the less severe states. The current radiation tolerance approach is deemed to be a good solution.

The HPTDC implemented a new capability of a coarse readout of the CFD pulse length. As there are not enough available HPTDC inputs to make a full timing resolution readout, the precision is severely limited by the FPGA clock speed of 400 MHz. This makes the amplitude resolution about 100 mV, which is still good enough for basic tuning and monitoring purposes. The values read out can be stored in the data stream in place of the coarse time information used during timing in of the system.

The rate capability of the HPTDC module was increased by sidestepping the problem. It was improved by the introduction of DTM, which lets through only the events where the trigger condition (number of bars in train that have a signal) was satisfied. This solution is good enough for LHC run 3 conditions.

4.13.2 PicoTDC

The PicoTDC is a recently developed TDC chip with much improved capabilities. Once integrated onto an FPGA-controlled board, it is meant as a drop-in replacement of the ageing HPTDC platform. It features a much improved timing resolution, readout rate and reduced dead time. Summary of the parameter comparison to HPTDC is in Table 4.3.

parameter	HPTDC	PicoTDC
bin size	24.4 ps	3.05 ps
channels per chip	4	64
L1 buffer	256 hits	512 hits
trigger buffer	16 events	512 events
readout buffer	256 word fifo	4×512 word buffer
readout rate	1.28 Gbps	10.24 Gbps
trigger matching at	80 MHz	320 MHz
dead time	5 ns	0.8 ns
ToT[a] binning	100 ps/2.5 ns	full resolution
power consumption	$\sim$ 1.3 W	$\sim$ 1.3 W

Table 4.3: Comparison of HPTDC and PicoTDC parameters.

[a]Time over Threshold, used for determining CFD pulse length which carries information about the original raw pulse amplitude. Relation between ToT and the input pulse amplitude was determined and a conversion formula derived from the results in section 4.10.

As of the time of this writing, PicoTDC for AFP was not yet fully prepared. Therefore, integration tests with the full ToF signal processing chain could not be performed. Based on the theoretical parameters however, we can expect the overall timing resolution to be near the values observed by oscilloscope readout of the raw PMT signal and CFD processed signal.

If these expectations are fulfilled, this would mean the TDC would no longer be a major contributor of timing uncertainty in the ToF signal processing chain. The resulting timing resolution would then be dominated by the impact of the raw signal source: the limited photon yield of the ToF bars and the MCP-PMT timing resolution.

Chapter 5

Performance of the AFP-ToF system

While the previous chapters offered a detailed description of the AFP-ToF system and all of its components, they focused on dedicated tests designed to separate the influence of the individual parts and their modifications. This approach is critical for development of any system as observing only the overall performance of the whole system does not usually provide enough insight on the impact of hardware changes and parameter tuning.

In this chapter, the performance of the ToF system is examined in a more complete manner, drawing on beam test results and the data recorded at the LHC during the 2017 run.

5.1 Performance at beam tests

Beam tests present a perfect opportunity to test the system as a whole. With a suitable beam, the performance should be very close to that when installed on the LHC, at least until high rate or low lifetime issues make their influence.

5.1.1 Raw signal timing resolution

Raw signal timing is one of the results of interest, judging the ToF performance without including the HPTDC contribution. The analysis of raw (or CFD) signal gathered by a suitable oscilloscope is much faster and more flexible, providing with crucial information of timing impact of individual modifications without the additional smearing by the HPTDC. As an added benefit, signal shape can be observed when the hardware CFD is not processing the signal.

While the most important parameter is the combined train timing resolution, the results for individual bars are of interest as well, observing how the bar position in the train impacts the performance. Such results of the 2017 setup are in Figure 5.1. The bars A and D have a worse timing, which can be attributed to the non-uniformity of the PMT channel performance as explored in subsection 4.6.5.

These results were obtained with the SiPM trigger selecting the area near the bar edge, helping to gather more Cherenkov light through the edge reflection mechanism previously explained in Figure 3.6. An "x-scan" was also performed, observing how the timing depends on the distance from the bar edge. This is shown in Figure 5.2. The typical diffraction event will usually hit AFP about halfway across the active are in the x axis, making the result near 10 mm of 19 ps the most relevant for the ToF system at LHC.

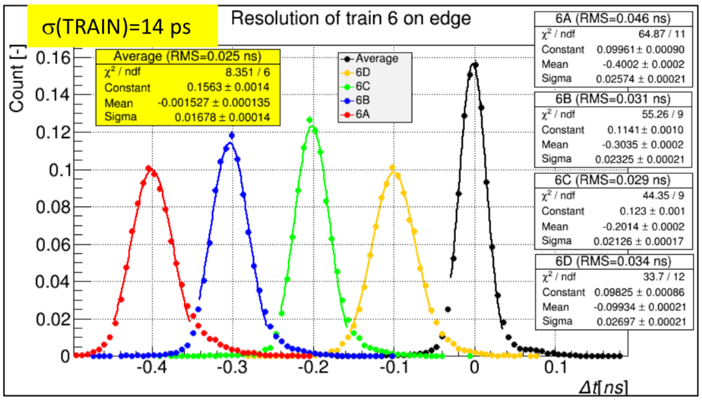

Figure 5.1: Timing performance of individual bars and the train combination of the original AFP-ToF design. This measurement was performed using hits near the bar edge. The reference trigger contribution of 9 ps has to be subtracted from the fit values, resulting in the 14 ps resolution of the train combination. This plot has been previously published in [44].

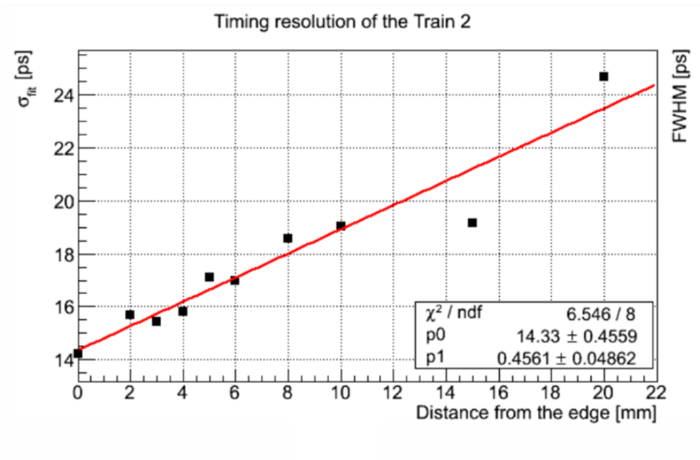

Figure 5.2: Timing resolution dependence on the distance of the particle hits from the bar edge. These plot points have the trigger contribution already subtracted. This plot has been previously published in [44].

With the new generation of XPM85112-S-R2D2 MCP-PMTs, the glueless ToF bars and the out of vacuum solution implementation, the timing resolution of the system was expected to change. The OOV changes are not expected to impact the timing significantly in either direction. The new ToF bars are then the major upgrade. Based on previous tests (direct comparison to old glued bars), these provide much more light and also significantly improve the timing performance by $15-20\,\%$. The MCP-PMTs however have a significantly worse single photon timing resolution (TTS), about ~ 40 ps as compared to ~ 30 ps in the first generation we used. This means the timing was expected to deteriorate and this was confirmed by the timing measurement result in Figure 5.3.

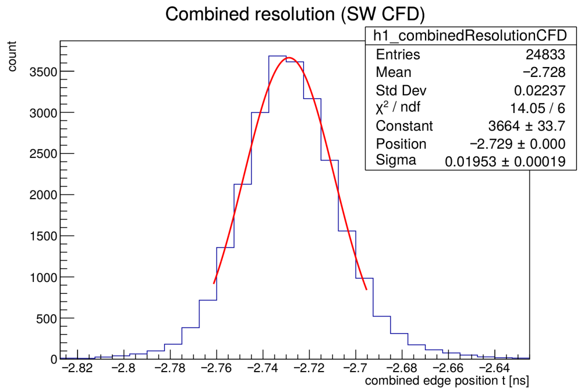

Figure 5.3: Timing resolution of the AFP-ToF system in 2021, featuring the OOV, the glueless bars and the new XPM85112-S-R2D2 PMTs. After subtracting the trigger contribution, the timing resolution becomes 16.1 ps. The trigger contribution here was 11 ps, showing the SiPM reference detectors are slowly ageing compared to the older beam tests.

When using the old glued bars instead for comparison, the timing performance gets worse, from 16.1 ps to 18.7 ps. This nicely matches the expectation set by the worse PMT TTS, as extrapolating from the result with the older PMT in Figure 5.1 gives us $14\,\text{ps} \times (30/40) = 18.7\,\text{ps}$.

Now we can use the same calculation in reverse to get a theoretical prediction of how the timing performance would look like with the new ToF bars when used with PMTs that have TTS of 30 ps (although we cannot use the first generation as it would not survive long, offering even shorter operational lifespan than in 2017). By adjusting the 16.1 ps result by the 30/40 ratio we get 12 ps.

This shows the compound effect of the improvements during the ToF development, especially the glueless bars. The only part that is letting us down in terms of timing is the XPM85112-S-R2D2 MCP-PMT, but it is currently necessary to use these especially due to their supreme lifetime. The performance prediction of 12 ps could not be verified by a measurement as we no longer have any PMT of the original generation (XPM85112/A1Q) in a good working condition. The improvement using the XPM85112-S-R2D2 however clearly shows the potential to achieve this is real.

One of the major changes in the operational parameters of the ToF system was the reduced PMT gain. A set of test beam measurements was performed to determine the timing resolution impact of the switch to a gain of ~ 2000. The results are in Figure 5.4. The measurements were performed with the trigger being 9 mm from the edge, making this a realistic scenario for the LHC. After subtracting the trigger contribution, a timing resolution of 24 ps was achieved at the gain 2000.

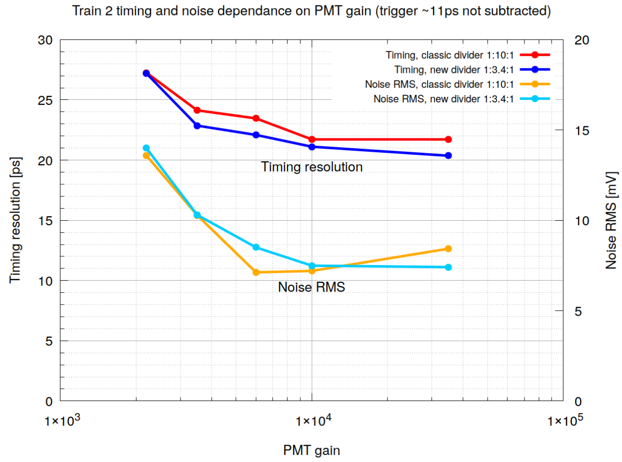

Figure 5.4: Timing resolution (left axis) and noise RMS (right axis) during the gain scan of the PMT. The PMT gain changes were compensated for by the PAbc attenuation settings (targeting unchanged output pulse amplitude), resulting in the noise level decreasing. The noise influence is the major reason for the timing deterioration at low PMT gain.

The Figure 5.4 also includes a test of the modified ratio HV divider and clearly shows a timing resolution advantage at the same gain. This was a final confirmation that the modified divider is advantageous and was therefore selected as the baseline solution for ToF installation at the LHC.

5.1.2 Full chain timing resolution

The timing performance of the full chain in Figure 5.5 is the final parameter of interest at the beam tests, allowing to extract the HPTDC contribution.

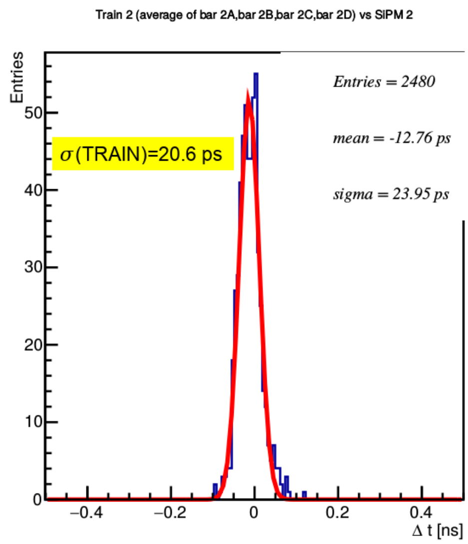

Figure 5.5: Timing resolution of a ToF train when the full readout chain is used. After subtracting the trigger contribution, the resulting resolution is 20.6 ps. This measurement was made at the bar edge, making it an optimistic scenario. This is a result obtained with the original ToF design.

When this result from 2017 is compared to the Figure 5.1 (raw train resolution), the contribution of the HPTDC is determined to be $15 - 16$ ps. The HPTDC timing resolution has not changed since 2017. In real operation of the new ToF system, a timing performance in the range of $20 - 30$ ps is therefore expected. If the promises of the PicoTDC described in section 4.13 become a reality, the timing performance of the full readout chain would become very close to the raw signal measurements.

5.1.3 Efficiency of the ToF system

The efficiency of the ToF system can be adjusted by tuning the CFD thresholds. This allows to strike a balance between the efficiency and fake triggers caused by interference and crosstalk.

The efficiency was evaluated at a beam test triggering at a 9 mm distance from the bar edge, simulating the real position where most events would hit at the LHC. A 200 mV threshold yielded single bar efficiency of $\sim 90\%$, while a reduction to 100 mV threshold improved it to $\sim 94\%$. A threshold in the range of $100 - 200$ mV is expected to be used at the LHC.

Of course single bars are not what is normally used when acquiring data. Another parameter with major impact on efficiency is the DTM trigger condition. Under standard operation, the 2/4 or 3/4 conditions are typically used, reducing the overall efficiency by requiring coincidence of multiple bars in a train. This reduces the train efficiency to $75 - 90\,\%$ depending on the combination of threshold and trigger condition in use.

5.2 ToF performance at the LHC

5.2.1 Performance study of 2017 LHC data

As AFP-ToF was installed for the 2017 LHC run, the resulting data were available for analysis of timing resolution of the ToF system when used in its standard operational environment. This proved challenging, as the PMTs used were not of the long lifetime type (as discussed in subsection 4.6.2). This meant their performance quickly deteriorated and efficiency was very low, well under 5 %. Nevertheless, with hard work of our data analysis expert Karel Černý, a lot of useful information could still be extracted, including the timing resolution [45]. The resolution of the individual bars can be seen in Figure 5.6.

The timing resolution results show individual bars in the range of $20 - 50$ ps, with the typical pattern of the first (A) bars being the worst and the third (C) bars performing the best. This wide spread indicates that for the best possible timing information extraction, the individual bar contributions should be combined with a weighing mechanism in place instead of the simple average typically used during the development process. This way, the worse performing bars would not ruin the timing when combined with the information from the better performing ones.

When the individual bar timing information is appropriately combined into train timing, we obtain 20 ± 4 ps as the timing resolution on the A side and 26 ± 5 ps on the C side AFP-ToF system.

At the LHC, the ToF timing is a tool for matching event vertices in ATLAS. For this reason, the final performance should be evaluated as the vertex matching spatial resolution, pairing the double tag ToF events to the ATLAS reconstructed vertices.

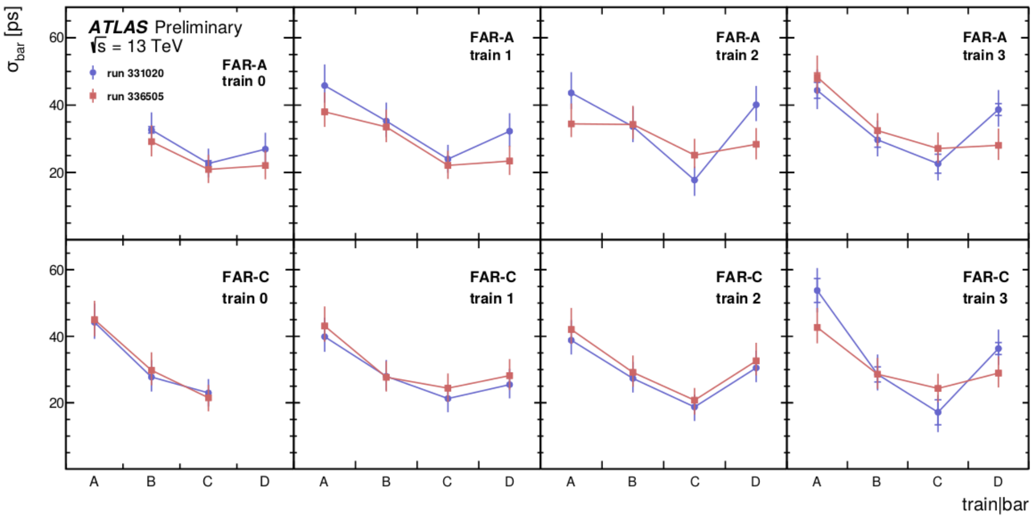

Figure 5.6: Timing resolution of individual ToF bars during the 2017 LHC run. This plot has been previously published in [45].

The results in Figure 5.7 show a resolution of 6.2 ± 1.0 mm, matching the expected range of 5.5 ± 2.7 mm that was based on the timing performance values.

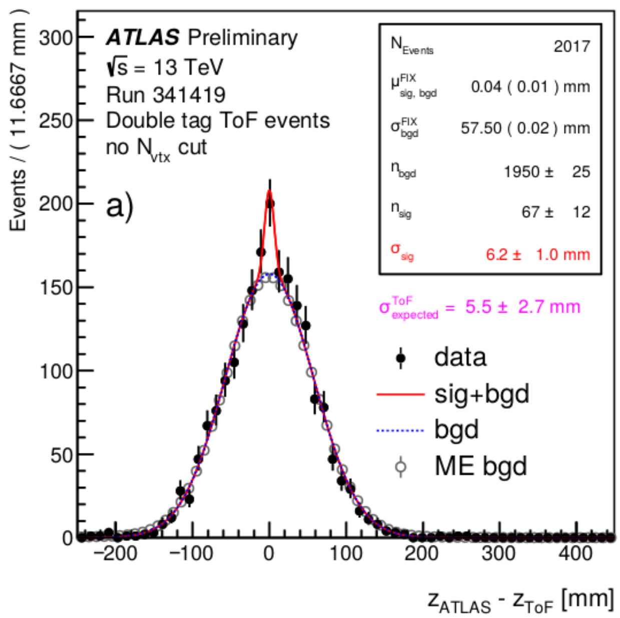

Figure 5.7: Vertex matching resolution of the AFP-ToF system in the 2017 LHC run. This plot has been previously published in [45].

5.2.2 Performance predictions for Run 3

While the LHC Run 3 commenced already, we do not yet have a comprehensive analysis of the updated ToF system performance available. Following are therefore predictions of the performance based on beam tests and the 2017 LHC run experience.

With well tuned ToF parameters (as mentioned later in section 7.6), we expect the train resolution to be in the $20 - 30\,\text{ps}$ range. ToF train trigger efficiency is expected to be $75 - 90\,\%$.

The predicted timing resolution range is only slightly worse compared to the 2017 LHC results. This is caused mostly by the worse PMT TTS, which also meant a slightly worse timing resolution was achieved on the beam tests (see subsection 5.1.1). The somewhat worse timing prevails despite many other updates that go counter that and would improve timing on their own. If we get a hold of better performing PMTs in the future, the ToF system is sure to surpass the past best performance values, both at beam tests and at the LHC. Implementation of the long awaited PicoTDC would also improve the timing considerably, but we have yet to see the actual performance it can achieve at a beam test to make a specific prediction.

The predicted efficiency mentioned above is much better compared to the 2017 LHC results. There the poor efficiency of only a few percent was caused by the short lifetime of the PMTs [45]. This critical parameter, determining how long the PMTs can operate at the LHC without deteriorating, is orders of magnitude better with the currently used tubes compared to the previously used MCP-PMT generation and should not be a concern at Run 3 at all.

Chapter 6

Detector package preparation and installation

Before the actual installation, it is critical to test all the components in appropriate laboratory setups. For most pieces of the electronic signal chain, suitable pulse signal generators are sufficient to ensure proper operation of all the signal channels, confirmed via oscilloscope and/or a spectral analyser.

After the necessary preparation of each part type (cleaning of optical parts and the RP flange, shielding of first stage amplifiers), integration tests of the complete setup are performed at a Beam Test to ensure the system operates correctly as a whole. Only then the actual installation effort can begin without the risk of significant delay and difficult handling of issues in-situ.

6.1 Spares

The world of hardware can be very challenging, human error or a simple equipment failure can easily happen at the most critical times. For this reason, AFP implemented a general policy of having at least +50 % spares of all the needed devices and equipment pieces ready, meaning that $^3/_2$ of the actually necessary pieces were in stock. This has proved very useful more than once, even in cases where failing equipment could be repaired, but time pressure did not allow for that to happen in time. This proactive approach played an important role in the success of not only the AFP detector package preparation and installation efforts, but of the numerous beam test campaigns as well.

The ToF spares include an extra complete set of the optical ToF bars, at least one extra photomultiplier, $1-2$ extra pieces of each type of the signal processing modules, but also extra sets of all the signal cable types utilized. A similar approach is applied for SiT equipment as well and extra AFP flanges with all the mechanical parts and fasteners are also available.

Another complete AFP station can be assembled from the spare parts. This is usually used in a test stand in the AFP lab or at the beam tests at time periods when the four AFP detector packages (2 with SiT only, 2 with SiT + ToF) are installed at the LHC.

6.2 Cleaning of optical parts

The performance of the optical parts of the ToF detector (optical bars, PMT window) depends strongly on the cleanliness of their surface. The bars depend heavily on the total internal reflection of the produced Cherenkov photons and need to be kept exceptionally clean. All manipulation is performed using clean nitrile rubber gloves and the bars are cleaned right before the final assembly using solvents such as high grade isopropyl alcohol or methanol. The separation window is handled in the same manner. The PMT window is then also cleaned in a similar fashion, although a careful manipulation is possible without the use of gloves.

As the bars are in a secondary vacuum inside the Roman Pot, we don't use any optical contact between the bars and the PMT or separation window, there would be a high risk of evaporation and deposition on surfaces inside the pot, including the bars. Radiation hardness and deteriorating transmissivity of such optical contact material are also a serious concern; instead we opt for an antireflex coating on the separation window faces to improve signal transmission (reducing reflective losses). No such coating is used on the bars themselves as maximum internal reflection capability is required for proper signal transmission through them.

6.3 Assembly of AFP on the Roman Pot flange

6.3.1 Assembly of the SiT layers

During the installation process, the SiT layers are installed first on the heat exchanger, which is then mounted on the flange, connecting it to the cooling lines. The precise position is defined by the use of tight precision pins on both the exchanger – SiT and exchanger stand – flange interfaces, using shims to adjust the height as needed and screws to fix everything in place. The SiT layers can then be covered with special 3D printed covers for protection during further manipulation.

6.3.2 Assembly of the ToF bar matrix

The ToF bar assembly is prepared separately at first, fixing all the 16 bars into their holder. This holder is made up of a number of precisely machined individual aluminium plates. Three of these plates separate the ToF trains while two extra thick ones close the assembly from both sides and apply a pressure to keep the bars in place. The contact points of the bars with the plates are minimized and covered with thin kapton tape strips to protect the surface of the bars. Small shims are then defining the gaps between the bars within a train. The ToF bar assembly can be seen in Figure 6.1.

In case of pre-OOV ToF, the ToF mount with the PMT had to be prepared. After the OOV upgrade, only the ToF mounting tube with the separation glass has to be in place to continue and the PMT can be installed later from the outside.

When the ToF mount is prepared, the bar assembly can be mounted on top of it. The bar assembly is then slightly loosened and the bars are carefully lowered into contact with the PMT face (pre-OOV) or the separation glass (OOV variant). This process is shown in Figure 6.2.

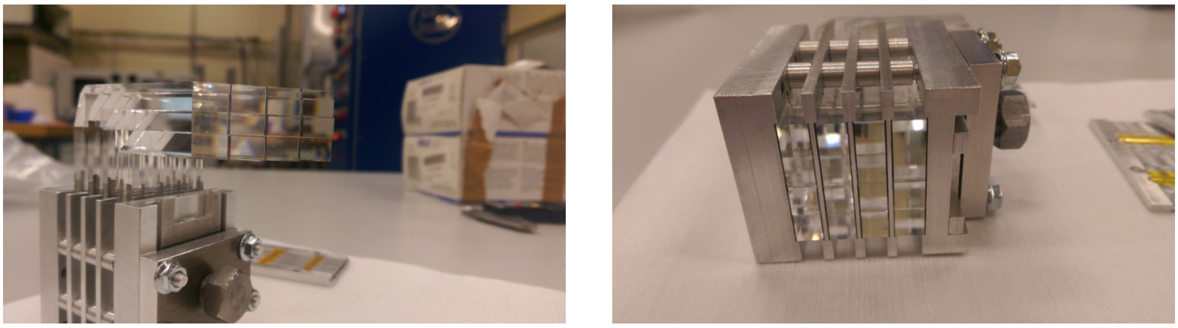

Figure 6.1: The ToF bar assembly. The separation plates with the kapton tape strips prepared can be seen in the background, showing the two contact points for each bar.

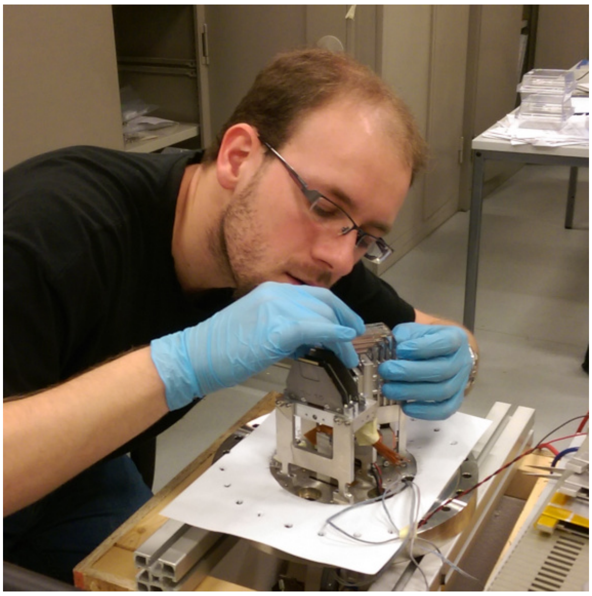

Figure 6.2: Careful installation of the ToF bars onto the AFP flange. This is the pre-OOV design, where risk of damaging of SiT planes during ToF manipulation and alignment was elevated, therefore extra care had to be taken, especially in the tedious alignment phase.

6.3.3 ToF signal path preparation

In the pre-OOV ToF variant, the PAa boards had to be connected at the back of the PMT and fixed onto the ToF heat exchanging element. All the 16 channels then needed to be connected using individual small coax cables to an interconnection board that transferred the signal onto the flex feedthrough cables. On the other side of the flange, another set of boards was placed to break out the flex connection to individual MMCX coax connectors. This was previously well covered in Figure 3.31 in subsection 3.5.6. Furthermore, the HV connection of the PMT power lines to the HV feedthrough had to be sealed, as described in subsection 4.6.9.

With the OOV variant, all of these PMT connection complications are no longer needed. The coax cables with PAa channels integrated plug directly onto the back of the PMT with their MMCX connectors. As the PMT is behind the separation glass, technically at the other side of the flange (even though it is then inserted into the ToF mounting tube), this is all that is needed and the cables then lead directly to the PAbc input.

6.3.4 Precise alignment of SiT and ToF

The AFP detector active area needs to be as close to the bottom of the Roman Pot as possible, but with an appropriate margin in order not to break it by contact with the pot after insertion. This requires a careful measurement of the pot depth and alignment of SiT and ToF on the flange, with the pot and flange mating surfaces acting as a reference.

Alignment of SiT and ToF is in many ways similar. The focus here will be on ToF, but the same general principles apply to SiT as well.

SiT alignment is performed first, targeting $\sim 130\,\mu$m distance from the pot bottom. The SiT height then serves as a reference for the ToF alignment, aiming for a position $-100^{+0}_{-20}\,\mu$m below the SiT edge. This tight interval is targeted in order not to lose too many events that would be detected by SiT but would fall beyond where the ToF bars are.

In case of pre-OOV, the ToF alignment was a very laborious process, using shims below the ToF mount and each iteration required numerous checks of the signal connection (like PAa being properly seated). After the OOV upgrade, the position is tuned simply by turning the precision screws on the outside of the flange. Once tuned in, the position is fixed with the coarse screws and a final check of a possible position drift caused by the fixation is performed.

As the ToF bar assembly is not completely flat, the individual bars have to be probed and appropriate corrections along one translation and three rotation axes are applied. The translation axis is simple up-down direction. The first rotation axis is rotation along the mentioned translation axis, ensuring the bar edges are parallel to the beam for optimal ToF performance. This can be performed separately first by rotation of the ToF mount. The other two rotation axes adjust the angle of the top surface, where the Roman Pot bottom is (Train 1). These are adjusted together with the height using the shims or adjustment screws. An illustration of the top plane alignment is in Figure 6.3, showing the target maximum height was hit very precisely while some of the bar parts are slightly lower due to their non-perfect mount, especially Bar C diverging from the plane kept by the rest. All of the bars hit the target height tolerance.

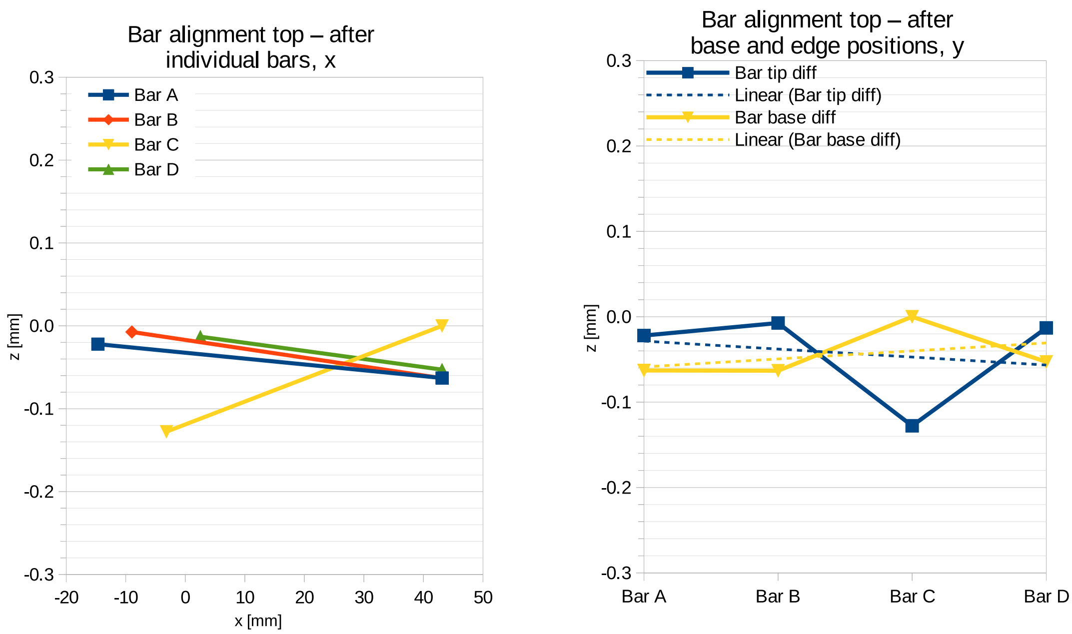

Figure 6.3: Visualization of ToF alignment results. Each bar is probed at two points. On the left, the bars are plotted individually, their angles providing the adjustment in one of the tilt axes. The different length of the bars at the tips (at edge) is visible while they are aligned at the base. On the right, the bar tips (edge) and base (ankle) probe points are grouped together, providing fits to compensate the other axis. The height is selected based on the highest point. The calculation of the adjustment for the shims or screws is calculated from these automatically using a spreadsheet or a Matlab routine. The $z = 0$ corresponds to the target maximum height of $-100^{+0}_{-20}\,\mu$m below the SiT, therefore all the bars nicely fall into this tolerance range.

Alignment with a jig and a depth gauge

At first, a simple approach to the height measurement was used. This was implemented using a measurement jig and a depth probe, as shown in Figure 6.4.

This alignment method was eventually discontinued for being prone to human error during the data point recording phase.

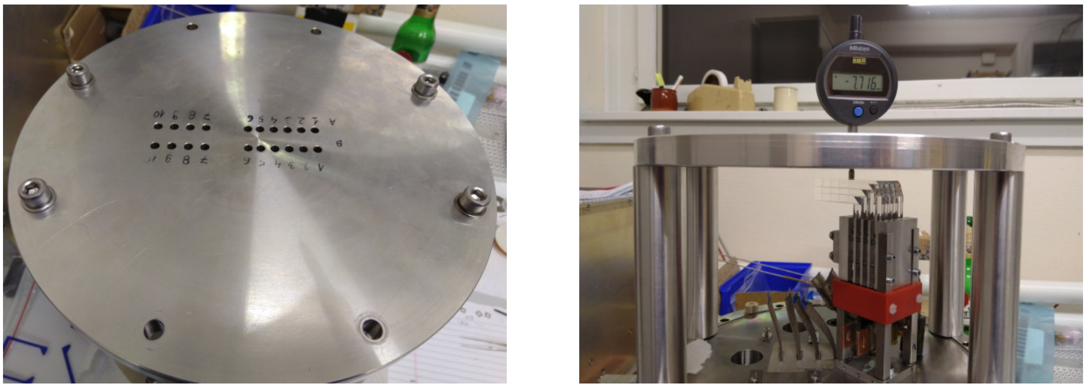

Figure 6.4: The jig used for SiT and ToF alignment using the depth gauge.

Alignment with 3D touch probe metrology

The alignment measurement process was upgraded using the Tesa micro-hite 3D industrial 3D metrology machine. While this brings a small risk of breaking the bars due to the slight pressure that has to be applied, it removes the human error factor as data is recorded automatically. The bar breaking risk was assessed in advance by testing a decommissioned bar. With the glueless bars, this risk was essentially eliminated as they no longet have the glued weak spot. The measurement process on the 3D metrology machine is in Figure 6.5.

6.4 Installation of the AFP detector packages at the LHC

In the previous sections, the preparation of the AFP detector packages on the Roman Pot flanges was described. These packages are then carefully transported to the LHC tunnel where they can be installed into the Roman Pots prepared at the LHC beamline. The packages ready for installation can be seen in Figure 6.6 and the insertion process in Figure 6.7.

The AFP package insertion process is guided by sliding the flange on three brass guide rods installed through the bolt holes. This ensures the detector parts would not collide with the pot due to improper angling. The vacuum seal is facilitated by a pair of knife edges and a copper ring with a vacuum grease, as previously shown in Figure 3.2. Once the flange is mounted using several bolts, the guide rods can be removed, making room for the rest of the 24 bolts. These are then tightened in the order noted in Figure 6.8. This process is repeated several times until the bolts cannot be tightened any more, ensuring proper vacuum seal of the knife edges and correct seating of the mating surfaces.

With the AFP flanges mounted, now is the time for the ToF PMT installation when the OOV flange design is used. The PMT can be replaced later without opening

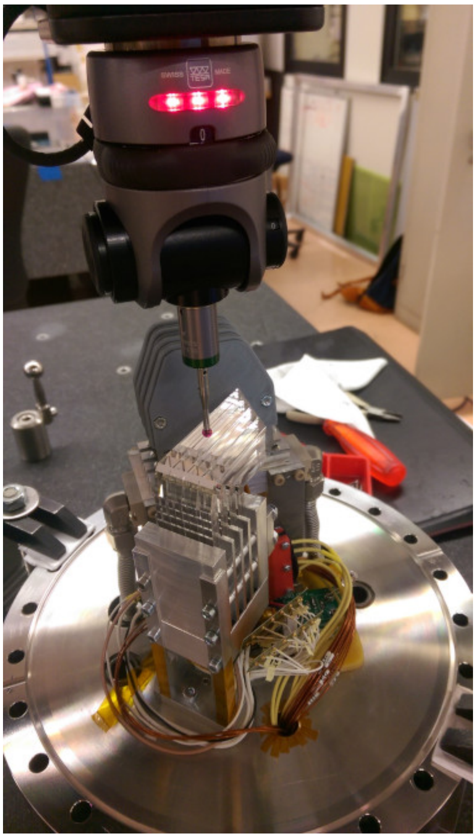

Figure 6.5: The Tesa micro-hite 3D machine probing the ToF bars height.

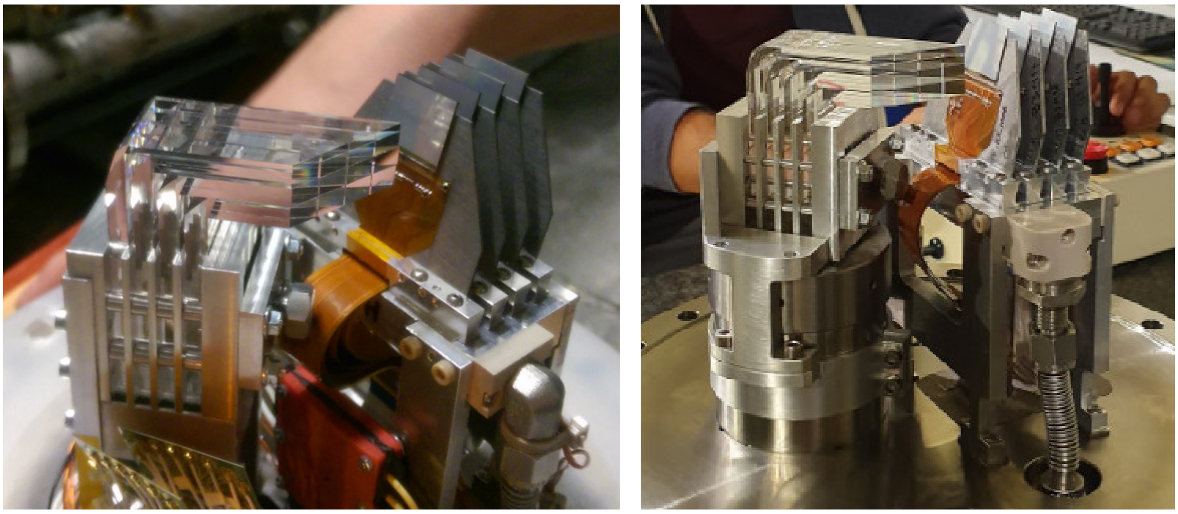

Figure 6.6: The AFP detectors (original and out of vacuum redesign) on a flange, ready to be installed into the Roman Pot container at the LHC. On the right part of each flange, four tracker planes are mounted with a tilt of 13°. On the left of each flange, the 4×4 matrix of the Cherenkov bars is placed with a photomultiplier tube positioned below to detect the Cherenkov light produced. The OOV variant is much cleaner, without the need to tuck away cables and connections. No ToF cabling is on the inside of the pot any more, running through the mounting tube instead.

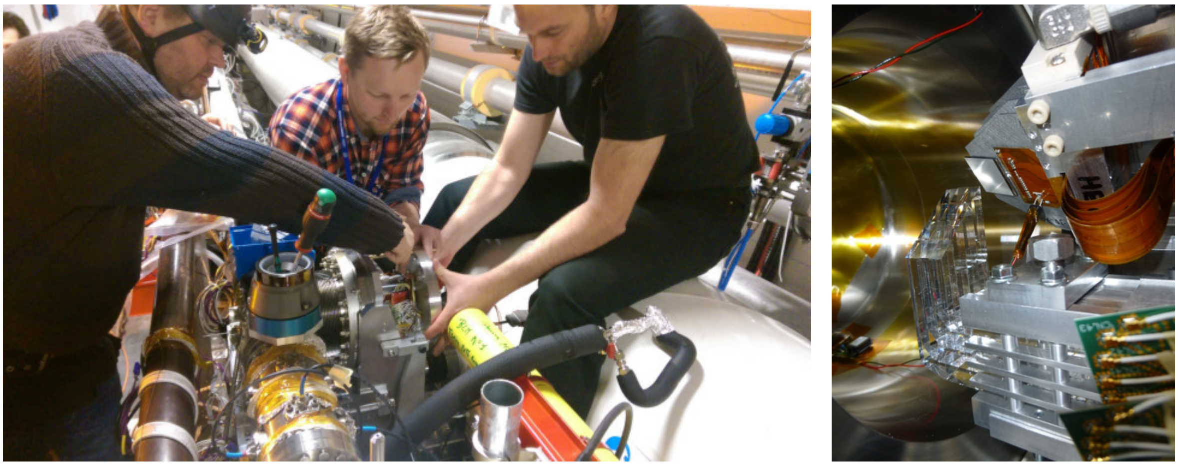

Figure 6.7: Insertion of the AFP detector package into the Roman Pot at the LHC.

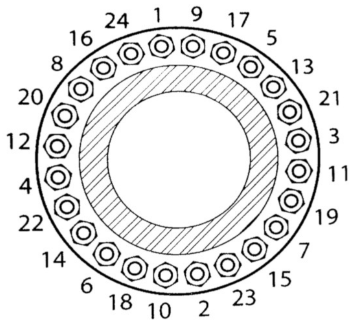

Figure 6.8: The tightening order of the bolts on the AFP flange.

the pot, a major advantage. All the PAa channels are connected to the PMT and the coax cables ran through the ToF heat exchanger. The PMT is then inserted into the mounting tube in the desired orientation. The heat exchanger is then secured using spring loaded clamps, ensuring the PMT sits tight onto the separation glass. The pulser fibres are then inserted in the channels alongside the heat exchanger, delivering light pulses for testing purposes when desired. After the PMT and the fibres are installed and secured, the LTB (Local Trigger Board) can be mounted on the flange back side and the SiT flex cables can be connected to it. Subsequently the PMT HV divider and HV supply are connected.

Finally, the ToF modules are inserted into the prepared ToF crate and all the connections between the modules are done using the appropriate cables. The ToF crate is in Figure 6.9. The TDC and DTM trigger outputs are also connected to the switch boxes leading to the air-core cable and the TDCs are connected to the LTB via STP (shielded twisted pair) cables with RJ45 connectors, facilitating the control and readout connection.

6.5 Testing procedures during ToF installation

The ToF system is complex and consists of many individual parts. During the installation, the system has to be rigorously tested for any malfunctioning channels, even though integration tests were already performed at a beam test. This way, any faulty equipment can be replaced right away.

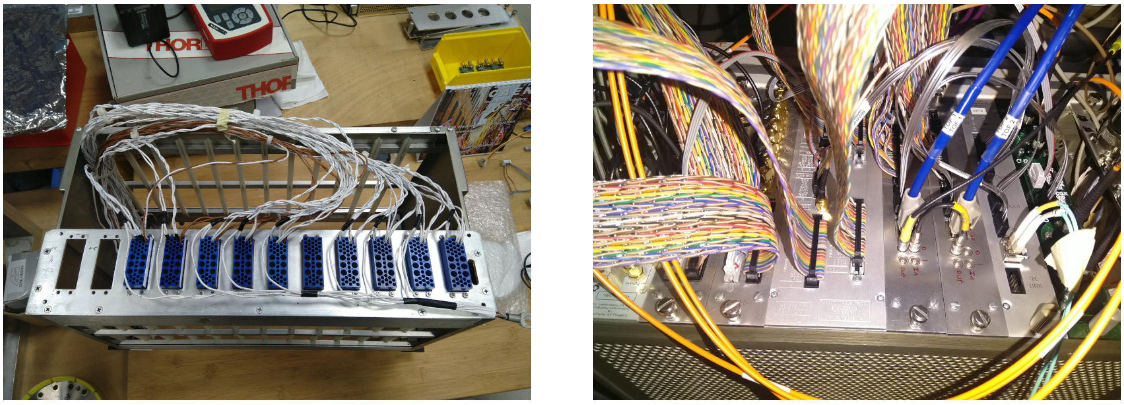

Figure 6.9: The ToF crate, empty with the individual powering connections prepared on the back and populated with the ToF modules.

The first step is to power up the modules, observing whether their power draw is within specification. This is also another final check of the ToF crate wiring.

Then comes the time to test the signal from the PMT. This is done right after the PAa cables are connected to the PAb(c) channels. Initially, the PMT was used at a gain where it would produce numerous dark pulses and these would be observed at the PAb(c) output. Later the pulser was implemented, providing a test light signal that can be used for this purpose. All 16 channels are tested with the oscilloscope observing four at a time.

When the PMT and amplifier channels are validated, the CFDs are connected and the pulses are observed in a similar way. Next, the DTM is tested, checking both the signal pass-through and the trigger output. Finally the TDCs are tested, not with a scope, but using their standard readout.

Chapter 7

AFP-ToF commissioning and operation

Commissioning is the process of bringing the detector hardware alive, testing its behaviour, tuning the necessary parameters and ensuring it operates in a manner compatible with the larger systems it is a part of, the ATLAS detector and the LHC accelerator.

7.1 ATLAS DCS

The Data Control System (DCS) is a control and monitoring system that enables remote control, monitoring, state logging and automatic actions in case some operational parameters exceed defined bounds. The AFP detector finite state machine (FSM) is implemented as a part of the wider ATLAS DCS. The main screen of the AFP system in DCS is in Figure 7.1.

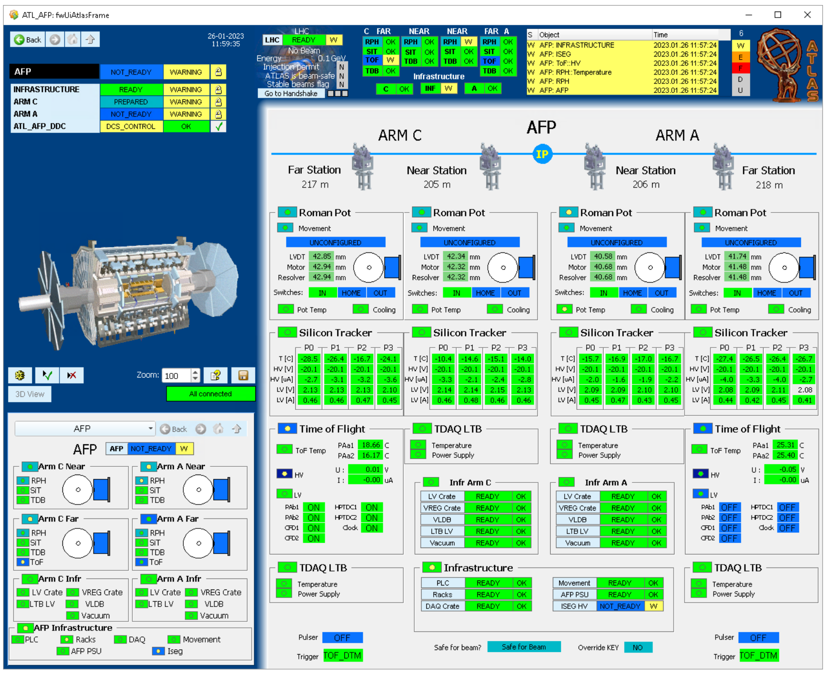

Figure 7.1: Data Control System for AFP. This interface is accessible online, limiting the need to have experts on-site.

7.2 Roman Pot movement – Beam Based Alignment and Loss Maps

Before AFP is allowed to routinely insert the pots close to the beam, the pot position relative to the beam needs to be well defined using a carefully designed process called the Beam Based Alignment (BBA) and the safety of the determined nominal data taking position stress tested using the Loss Maps procedure. Dedicated LHC fills are used for this purpose and AFP enters combined readout with ATLAS.

During BBA, the beam is trimmed by collimator jaws to a known size. Collimators are devices that physically extend to the edges of the beam and ensure anything beyond a certain distance is physically blocked. The individual AFP Roman Pots then slowly move towards the beam until a sharp increase of rates in the Beam Loss Monitors (BLM) is observed. The pot is then slightly retracted (by $2\,\sigma$) and the procedure is repeated with the other pots one by one. When all pots are finished, some useful calibration data can be taken as the pots are inserted much closer to the beam than they are throughout standard running.

Then the Loss Maps need to be performed. This procedure ensures the nominal data taking position ($20\,\sigma$ from the beam) is safe. The beam orbit is intentionally distorted and BLM rates are again observed. This time, no sharp rate increase should be detected as that would signify the beam has touched the pot, something that should never happen.

The above BBA and Loss Maps procedures need to be repeated for all the LHC optics at which the detector will be used, as that changes the beam shape.

7.3 LHC intensity ramp-up

The intensity of the beam (number of bunches) is gradually increased over many fills to ensure the safety of high intensity operations. The AFP pots are inserted to their nominal position at each step to make sure no adverse effects arise. These insertions usually present a good opportunity for detector timing-in and other necessary steps.

7.4 SiT commissioning

SiT commissioning is a process of preparing the SiT modules for standard operation, including operations like annealing and calibration of thresholds. The readout timing with respect to the reference clock also needs to be well tuned, ensuring all the modules are read out within the correct bunch crossing window of 25 ns. For this reason, a beam with isolated bunches (where some bunch crossings do not have neighbours nearby) is required. The SiT commissioning is well covered in [46].

7.5 ToF commissioning

The first step in ToF commissioning is to ensure all ToF channels are working properly and equipment properly responds to configuration commands. This is of course checked continuously throughout the commissioning period. May it be the case that issues are found, a quick intervention can still be made to replace some modules. This will not be generally possible later when the beam intensity becomes high and LHC enters standard running phase. One set of the monitoring histograms used during commissioning is in Figure 7.2.

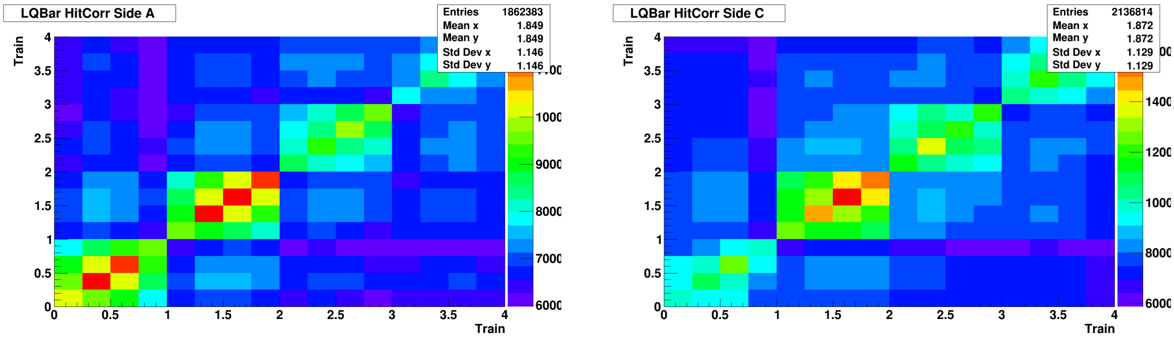

Figure 7.2: ToF bar signal correlation plot during commissioning. The high correlation of hits within a train (series of four bars) is clearly visible.

The ToF TDC is a separate system from the SiT from the readout point of view, so its readout latencies need to be timed in separately. This is done using a configuration file for the TDC and the readout coarse and fine time histograms are used for monitoring. The tunable variables are described in Figure 7.3. Just as with SiT timing in, isolated bunches are used for this and the TDC readout is limited to some area around the isolated bunch crossing selected for this purpose. A properly timed-in ToF produces a signal from the isolated bunch within a single bunch crossing, matching the previous timing in of SiT.

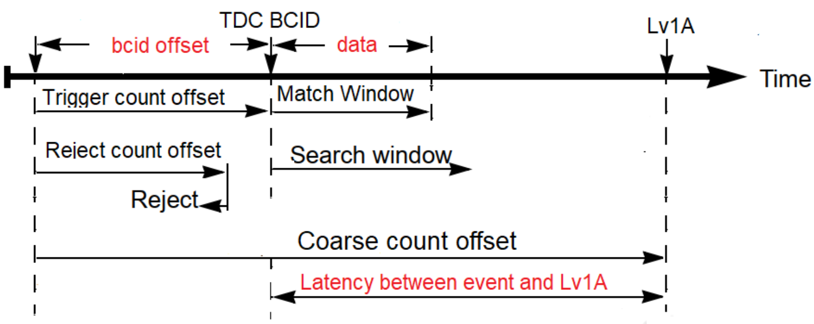

Figure 7.3: The HPTDC latency setup overview, showing the individual parameters. The Trigger count offset and Coarse count offset are the two variables that ate typically tuned during timing-in.

7.6 ToF operational parameters

Based on the beam test results of the ToF components and the adjustments made during the the commissioning period, the recommended AFP-ToF operational parameters for the LHC Run 3 are as follows:

- PMT high voltage 2030 V (ARM A), 2010 V (ARM C),
- PMT high voltage current limit 800 μA,
- CFD thresholds 150 mV,
- DTM trigger condition 3/4.

7.7 ToF at heavy ion runs

It has to be noted that in the case of heavy ion LHC runs (typically Pb-Pb or p-Pb), fragments of the original ions can reach AFP. This would present an opportunity for fragment identification based on the quadratic dependence of Cherenkov light intensity on the fragment charge (Equation 2.2), a role for which AFP-ToF was not designed. While some information might still be extracted by ToF, the dynamic range is insufficient and great care would have to be taken when selecting the gain of the PMTs due to the greatly increased amount of light. A dedicated detector that would serve this purpose at ATLAS has not been developed.

Possible generation of heavy showers by interaction with the ToF radiator bars (presenting a lot of material into the fragment path) is also a point of concern in these scenarios. A careful risk analysis has to be carried out before the ToF-equipped AFP stations could participate in any heavy ion run on the LHC. For the time being, it was decided not to participate in heavy ion runs when ToF is installed. The near AFP stations could still participate independently if desired as ToF is installed only at the far AFP stations on each arm.

Chapter 8

Summary

This work covers the characterization and development of AFP-ToF, a time-of-flight system for the AFP forward detectors. These are a part of the ATLAS experiment at the Large Hadron Collider.

Since 2016, the detector went through numerous upgrades, modifying essentially the entire system. The primary goal of these upgrades was to ensure reliable operation in the LHC Run 3 conditions. Where possible, the timing jitter contributions of the individual components were improved. One final piece, the PicoTDC, was not prepared by the responsible group in time and we eagerly await its arrival in the coming months. This should make a significant impact on the timing resolution of the system – the current HPTDC is one of the major contributors, with the Cherenkov bar radiators and the MCP-PMT being the other two major ones.

As a part of the development cycle, many tests with a laser setup and beam tests at an accelerator were performed. These were (together with prior simulations) critical in determining the optimal operational parameters and the performance of the entire system as well as the impact of individual modifications.

During the development, a new MCP-PMT type had to be adopted. This was due to the lifetime limitations of the previous generation. The first long life PMT type was tested and rejected for its numerous flaws. These were confirmed by other groups and communicated to the manufacturer. A solution to these flaws came in the next generation devices with adjusted MCP pore treatment. The XPM85112-S-R2D2 MCP-PMTs by Photonis passed the demanding tests and were accepted as a baseline solution for AFP-ToF going forward. The only downside of these was somewhat worse timing resolution ($\sim 40\,\mathrm{ps}$ single photon vs previous $\sim 30\,\mathrm{ps}$), an unfortunate outcome, but a necessary tradeoff for the lifetime they offer.

One of the most challenging parameter targets was the rate capability of the system to reach 20 MHz. This is the expected maximum rate during the LHC Run 3. The most critical component was the MCP-PMT, where the pores have a limit on how fast they can recharge after a multiplication cascade passes through them. A solution for this issue was found in a non-standard operation regime at low gain values. This approach necessitated the addition of a third amplification stage and meticulous mitigation of any outside interference with the signal. One other modification that prevented some undesired effects at the low gain was modification of the HV divider ratio.

The original ToF design was used throughout the year 2017 at the LHC. The older generation of MCP-PMT devices used could not survive the demanding operation for long and the efficiency quickly deteriorated. The timing resolution could still be extracted from the data, showing a $20 - 50\,\mathrm{ps}$ timing resolution of the individual bars resulting in a combined resolution of 20 ± 4 ps on the A side and 26 ± 5 ps on the C side. This timing resolution then yields a 6.2 ± 1.0 mm spatial resolution of vertex matching in the ATLAS interaction point. Many other lessons were learned from this period as well, feeding into the continued development.

The heavily modified AFP-ToF was again installed in September 2021 in preparation for the now ongoing LHC Run 3. The projected timing performance of the system is $20 - 30$ ps (train combination), with a potential for improvement when the new PicoTDC time to digital converter is ready. The train efficiency of $75 - 90\,\%$ is expected, a major improvement over the previous 2017 period, owing to the much improved lifetime of the Photonis miniPLANACON XPM85112-S-R2D2 MCP-PMTs.

Acknowledgement

The author gratefully acknowledges the support from Research Infrastructure for experiments at CERN LM2018104 of Ministry of Education, Youth and Sports of the Czech Republic (MSMT); Research Infrastructure for experiments at CERN LM2023040 (MSMT); and Palacky University IGA_PrF_2022_004.

Bibliography

[1] T. Komárek. Simulation of optical part of high-energy particle time-of-flight detector and comparison with data. Master's thesis, Palacký University in Olomouc, Faculty of Science, Olomouc, 2016.

[2] ATLAS Collaboration. Measurement of the total cross section from elastic scattering in pp collisions at s=7 TeV with the ATLAS detector. *Nuclear Physics B*, 889:486–548, 2014.

[3] ATLAS Collaboration. Measurement of exclusive pion pair production in proton–proton collisions at $\sqrt{s} = 7\,\mathrm{TeV}$with the ATLAS detector. *The European Physical Journal C*, 83(7):627, Jul 2023.

[4] Christian Bierlich, Smita Chakraborty, Nishita Desai, Leif Gellersen, Ilkka Helenius, Philip Ilten, Leif Lönnblad, Stephen Mrenna, Stefan Prestel, Christian T. Preuss, Torbjörn Sjöstrand, Peter Skands, Marius Utheim, and Rob Verheyen. A comprehensive guide to the physics and usage of pythia 8.3, 2022.

[5] L Adamczyk, E Banaś, A Brandt, M Bruschi, S Grinstein, J Lange, M Rijssenbeek, P Sicho, R Staszewski, T Sykora, M Trzebiński, J Chwastowski, and K Korcyl. Technical Design Report for the ATLAS Forward Proton Detector. Technical Report CERN-LHCC-2015-009. ATLAS-TDR-024, May 2015.

[6] T. Komárek. Visualization of particle tracks in an accelerator magnetic field, 2013.

[7] Gilbert N. Lewis and Richard C. Tolman. The principle of relativity, and non-newtonian mechanics. *Proceedings of the American Academy of Arts and Sciences*, 44(25):711–724, 1909.

[8] Claude Bovet, Réne Maleyran, L Piemontese, Alfredo Placci, and Massimo Placidi. *The CEDAR counters for particle identification in the SPS secondary beams: a description and an operation manual.* CERN Yellow Reports: Monographs. CERN, Geneva, 1982.

[9] Pierre Auger Observatory Collaboration. Search for photons above 1019 ev with the surface detector of the pierre auger observatory. *Journal of Cosmology and Astroparticle Physics*, 2023(05):021, may 2023.

[10] *Science with the Cherenkov Telescope Array.* WORLD SCIENTIFIC, 2019.

[11] S. Datta Majumdar and R. Pal. Cherenkov radiation in anisotropic media. *Proceedings of the Royal Society of London. Series A, Mathematical and Physical Sciences*, 316(1527):525–537, 1970.

[12] Michael Doring, K. Bernlohr, G. Hermann, W. Hofmann, and H. Lampeitl. Measurement of the Cherenkov light spectrum and of the polarization with the HEGRA IACT system. 7 2001.

[13] L. Nozka, A. Brandt, M. Rijssenbeek, T. Sykora, T. Hoffman, J. Griffiths, J. Steffens, P. Hamal, L. Chytka, and M. Hrabovsky. Design of Cherenkov bars for the optical part of the time-of-flight detector in Geant4. *Opt. Express*, 22(23):28984–28996, Nov 2014.

[14] L. Nozka, L. Adamczyk, G. Avoni, A. Brandt, P. Buglewicz, E. Cavallaro, G. Chiodini, L. Chytka, K. Ciesla, P.M. Davis, M. Dyndal, S. Grinstein, P. Hamal, M. Hrabovsky, K. Janas, K. Jirakova, M. Kocian, T. Komarek, K. Korcyl, J. Lange, D. Mandat, V. Michalek, I. Lopez Paz, D. Northacker, M. Rijssenbeek, L. Seabra, P. Schovanek, R. Staszewski, P. Swierska, and T. Sykora. Construction of the optical part of a time-of-flight detector prototype for the AFP detector. *Opt. Express*, 24(24):27951–27960, Nov 2016.

[15] UQG (Optics) Ltd. *Data Sheet Suprasil.*

[16] OHARA GmbH. *VAD-process Synthetic Fused Silica SK-1300.*

[17] K. Jiráková. Fast simulation of Cherenkov photons transmission through the optical part of the AFP detector. Master's thesis, Palacký University in Olomouc, Faculty of Science, Olomouc, 2017.

[18] M G Albrow, Heejong Kim, S Los, M Mazzillo, E Ramberg, A Ronzhin, V Samoylenko, H Wenzel, and A Zatserklyaniy. Quartz Cherenkov counters for fast timing: QUARTIC. *Journal of Instrumentation*, 7(10):P10027–P10027, Oct 2012.

[19] Libor Nozka, Andrew Brandt, Karel Cerny, Miroslav Hrabovsky, Tomas Komarek, Filip Krizek, Dusan Mandat, Marko Milovanovic, Michael Rijssenbeek, Petr Schovanek, Tomas Sykora, Vladimir Urbasek, and Jaromir Zatloukal. Performance studies of new optics for the time-of-flight detector of the AFP project. *Opt. Express*, 28(13):19783–19796, Jun 2020.

[20] P Antonioli, A Kluge, and W Riegler. Upgrade of the ALICE Readout & Trigger System. Technical Report CERN-LHCC-2013-019. ALICE-TDR-015, Sep 2013. Presently we require a LHCC-TDR reference number. At a later stage we will fill the required information.

[21] S. Hirose. Performance of the MCP-PMT for the Belle II TOP counter in a magnetic field. *Nuclear Instruments and Methods in Physics Research Section A: Accelerators, Spectrometers, Detectors and Associated Equipment*, 766:163 – 166, 2014. RICH2013 Proceedings of the Eighth International Workshop on Ring Imaging Cherenkov Detectors Shonan, Kanagawa, Japan, December 2-6, 2013.

[22] Andrew G. Brandt. Development of a 10 picosecond time-of-flight Counter. Technical report, The University of Texas at Arlington, March 2010.

[23] K. Inami, N. Kishimoto, Y. Enari, M. Nagamine, and T. Ohshima. A 5 ps TOF-counter with an MCP–PMT. *Nuclear Instruments and Methods in Physics Research Section A: Accelerators, Spectrometers, Detectors and Associated Equipment*, 560(2):303 – 308, 2006.

[24] PHOTONIS USA Pennsylvania, Inc. *miniPLANACON XPM85112 datasheet.*

[25] Louis Costrell, Frank R. Lenkszus, Stanley J. Rudnick, Eric Davey, John Gould, Seymour Rankowitz, William P. Sims, R. Roy Whitney, Robert W. Dobinson, Henk Verweij, Norman Latner, Vincent C. Negro, Edward J. Barsotti, Thomas E. Droege, Cordon Kerns, Kathleen J. Turner, Robert W. Downing, Frederick A. Kirsten, A. E. Larsh, Stewart C. Loken, Dick A. Mack, Lee J. Wagner, Robert C. Lucena, Dennis W. O'Brien, Allan Gjovig, Frank Naivar, Ronald O. Nelson, D. Hywell White, Carl Akerlof, Donald E. Stilwell, James H. Trainor, Bruno Gobbi, John A. Biggerstaff, Nat W. Hill, Gerald K. Schulze, David B. Gustavson, Dale Horelick, Paul F. Kunz, Leo Paffrath, Helmut V. Walz, W. Kenneth Dawson, John Cresswell, Satish Dhawan, and Charles E. L. Gingell. Standard NIM Instrumentation System.

[26] J Christiansen. HPTDC High Performance Time to Digital Converter. Technical report, CERN, Geneva, 2004. Version 2.2 for HPTDC version 1.3.

[27] R. Herbst, R. Claus, M. Freytag, G. Haller, M. Huffer, S. Maldonado, K. Nishimura, C. O'Grady, J. Panetta, A. Perazzo, B. Reese, L. Ruckman, J. G. Thayer, and M. Weaver. Design of the SLAC RCE Platform: A general purpose ATCA based data acquisition system. In *2014 IEEE Nuclear Science Symposium and Medical Imaging Conference (NSS/MIC)*, pages 1–4, 2014.

[28] Adam Krumbein. The Importance of RF Connector Selection in Antenna Design. White Paper, Southwest Antennas, Inc, 2019.

[29] Ladislav Chytka, Miroslav Hrabovský, Tomáš Komárek, Václav Michálek, Libor Nožka, Tomáš Sýkora, and Vladimír Urbášek. Time resolution of the SiPM-NUV3S. *Nuclear Instruments and Methods in Physics Research Section A: Accelerators, Spectrometers, Detectors and Associated Equipment*, 935:51–55, 2019.

[30] G. Papotti et al. SPS fixed target spill quality improvements in the longitudinal plane. In *Proc. IPAC'23*.

[31] Frank Tecker. Injection and Extraction. Technical report, 2021.

[32] R. Diener, J. Dreyling-Eschweiler, H. Ehrlichmann, I.M. Gregor, U. Kötz, U. Krämer, N. Meyners, N. Potylitsina-Kube, A. Schütz, P. Schütze, and M. Stanitzki. The DESY II test beam facility. *Nuclear Instruments and Methods in Physics Research Section A: Accelerators, Spectrometers, Detectors and Associated Equipment*, 922:265–286, April 2019.

[33] ETSI TC-SMG. GSM 05.01 – Version 5.2.0 – Digital cellular telecommunications system (Phase 2+); Physical layer on the radio path; General description (GSM 05.01). Technical Specification, European Telecommunications Standards Institute, 1997.

[34] Libor Nozka, Giulio Avoni, Elzbieta Banas, Andrew Brandt, Karel Cerny, Paul M. Davis, Serge Duarte Pinto, Vjaceslav Georgiev, Miroslav Hrabovsky, Tomas Komarek, Krzysztof Korcyl, Ivan Lopez-Paz, Marko Milovanovic, Goran Mladenovic, Dmitry A. Orlov, Michael Rijssenbeek, Petr Schovanek, Tomas Sykora, Maciej Trzebinski, Vladimir Urbasek, and Jan Zich. Upgraded cherenkov time-of-flight detector for the AFP project. *Opt. Express*, 31(3):3998–4014, Jan 2023.

[35] A. Lehmann, M. Böhm, W. Eyrich, D. Miehling, M. Pfaffinger, S. Stelter, F. Uhlig, A. Ali, A. Belias, R. Dzhygadlo, A. Gerhardt, K. Götzen, G. Kalicy, M. Krebs, D. Lehmann, F. Nerling, M. Patsyuk, K. Peters, G. Schepers, L. Schmitt, C. Schwarz, J. Schwiening, M. Traxler, M. Düren, E. Etzelmüller, K. Föhl, A. Hayrapetyan, K. Kreutzfeld, O. Merle, J. Rieke, M. Schmidt, T. Wasem, P. Achenbach, M. Cardinali, M. Hoek, W. Lauth, S. Schlimme, C. Sfienti, and M. Thiel. Lifetime of MCP-PMTs and other performance features. *Journal of Instrumentation*, 13(02):C02010–C02010, Feb 2018.

[36] T. Komárek, V. Urbášek, A. Brandt, V.A. Chirayath, L. Chytka, M. Hrabovský, L. Nožka, M. Rijssenbeek, and T. Sýkora. Timing resolution and rate capability of Photonis miniPlanacon XPM85212/A1-S MCP-PMT. *Nuclear Instruments and Methods in Physics Research Section A: Accelerators, Spectrometers, Detectors and Associated Equipment*, 985:164705, 2021.

[37] T. Komárek, V. Urbášek, A. Brandt, K. Černý, V.A. Chirayath, J. DeFazio, V. Georgiev, S. Hail, M. Hrabovský, Z. Kubík, L. Nožka, D. Orlov, S. Duarte Pinto, M. Rijssenbeek, T. Sýkora, F. Yang, and J. Zich. Characterization of the miniPlanacon XPM85112-S-R2D2 MCP-PMT with custom modified backend electronics. *Nuclear Instruments and Methods in Physics Research Section A: Accelerators, Spectrometers, Detectors and Associated Equipment*, 1041:167330, 2022.

[38] A. Lehmann, M. Böhm, A. Britting, W. Eyrich, M. Pfaffinger, F. Uhlig, A. Belias, R. Dzhygadlo, A. Gerhardt, K. Götzen, G. Kalicy, M. Krebs, D. Lehmann, F. Nerling, M. Patsyuk, K. Peters, G. Schepers, L. Schmitt, C. Schwarz, J. Schwiening, M. Traxler, M. Zühlsdorf, M. Düren, E. Etzelmüller, K. Föhl, A. Hayrapetyan, B. Kröck, O. Merle, J. Rieke, M. Schmidt, T. Wasem, E. Cowie, T. Keri, P. Achenbach, M. Cardinali, M. Hoek, W. Lauth, S. Schlimme, C. Sfienti, and M. Thiel. Recent developments with microchannel-plate PMTs. *Nuclear Instruments and Methods in Physics Research Section A: Accelerators, Spectrometers, Detectors and Associated Equipment*, 876:42 – 47, 2017. The 9th international workshop on Ring Imaging Cherenkov Detectors (RICH2016).

[39] Joseph Ladislas Wiza. Microchannel plate detectors. *Nuclear Instruments and Methods*, 162(1):587 – 601, 1979.

[40] Yu. Melikyan, T. Sýkora, T. Komárek, L. Nožka, D. Serebryakov, and V. Urbášek. Load capacity and recovery behaviour of ALD-coated MCP-PMTs. *Nuclear Instruments and Methods in Physics Research Section A: Accelerators, Spectrometers, Detectors and Associated Equipment*, 949:162854, 2020.

[41] P.E. Gray and C.L. Searle. *Electronic Principles: Physics, Models and Circuits*. Wiley, 1969.

[42] D. Adams. *The Hitchhiker's Guide to the Galaxy*. 1979.

[43] Jan ZICH. *Rychlé výběrové obvody pro časový detektor částic*. Disertační práce, Západočeská univerzita v Plzni, Fakulta elektrotechnická Plzeň, 2021. SUPERVISOR: Doc. Dr. Ing. Vjačeslav Georgiev.

[44] L. Chytka, G. Avoni, A. Brandt, E. Cavallaro, P. M. Davis, F. Förster, M. Hrabovsky, Y. Huang, K. Jirakova, M. Kocian, T. Komarek, K. Korcyl, J. Lange, V. Michalek, L. Nozka, I. Lopez Paz, M. Rijssenbeek, P. Schovanek, T. Sykora, and V. Urbasek. Timing resolution studies of the optical part of the AFP time-of-flight detector. *Opt. Express*, 26(7):8028–8039, Apr 2018.

[45] Performance of the ATLAS Forward Proton Time-of-Flight Detector in 2017. Technical report, CERN, Geneva, 2021. All figures including auxiliary figures are available at https://atlas.web.cern.ch/Atlas/GROUPS/PHYSICS/PUBNOTES/ATL-FWD-PUB-2021-002.

[46] Ivan Lopez Paz. The one-armed ATLAS Forward Proton detector, 2018. Presented 22 May 2018.

List of used symbols and acronyms

AFP	ATLAS Forward Proton
ToF	Time of Flight
ATLAS	A Toroidal LHC ApparatuS
LHC	Large Hadron Collider
PMT	Photomultiplier
CFD	Constant Fraction Discriminator
CERN	European Organisation for Nuclear Research
x, y, z	Spatial coordinates
η	Pseudorapidity
IP1	Interaction Point 1
RP	Roman Pot
TDR	Technical Design Report
SiT	Silicon Tracker
z_{ToF}	Vertex position calculated from ToF timing information
c	Speed of light
t_{A}, t_{C}	ToF timing information from A and C side
A side, C side	Anti-clockwise and Clockwise LHC direction sides around ATLAS
n	Refractive index
v_{p}	Speed of a particle
θ	Cherenkov cone angle
E	Energy
q	Particle charge
e	Elementary charge
μ	Medium permeability
ω	Frequency
LQbar	The ToF bars design
MCP	Microchannel Plate
TTS	Transit Time Spread
HV	High Voltage
λ	Wavelength
DE	Detection Efficiency
QE	Quantum Efficiency
CE	Collection Efficiency
FWHM	Full Width at Half Maximum
PA(a,b,c)	Pre-Amplifier (a,b,c)
(HP)TDC	(High Performance) Time to Digital Converter
NIM	Nuclear Instrumentation Module
PCB	Printed Circuit Board
CFD	Constant Fraction Discriminator

LVPECL	Low Voltage Positive Emitter Couple Logic
RCE	Reconfigurable Cluster Elements
SMA	SubMiniature version A connector
MMCX	Micro Miniature Coaxial
CTP	Central Trigger Processor
DAQ	Data Acquisition
SiPM	Silicon Photomultiplier
SPS	Super Proton Synchrotron
MIP	Minimum Ionizing Particle
RF	Radio Frequency
DESY	Deutsches Elektronen-Synchrotron
ALD	Atomic Layer Deposition
I	Electric current
I_{sc}	Strip current through MCP
U_{MCP}	Bias voltage over MCP
R_{MCP}	Internal resistance of MCP
I_{m}	Current drawn from MCP by multiplication
f	Pulse frequency
g	Gain
P_{e}	Photoelectron
N_{pe}	Number of photoelectrons
OOV	Out Of Vacuum (ToF mechanical implementation)
PC	Photocathode
DTM	Digital Trigger Module
PicoTDC	Pico Time to Digital Converter.
FPGA	Field Programmable Gate Array
SEU	Single Event Upset
DCS	Data Control System
BBA	Beam Base Alignment
BLM	Beam Loss Monitor

Appendix A

Implementation of a software CFD

A software CFD implementation prepared by the dissertation author during his PhD studies as a part of the data analysis software played a central role in the analysis of all the raw (oscilloscope) ToF data. The source code of the software CFD function is included below.

```
#include <iostream>
#include <vector>

#define INVALIDATE_SECOND_PEAKS true //whether to run check for preceding peaks in front of the highest

//time units should be in seconds, voltage, threshold and trigFrac in volts
//threshold is minimal amplitude, trigFrac trigger fraction level (sign determines positive/negative peak)
//returns succes bool and stores trigger time in the *trig
bool cfd_sw(std::vector<double> &tVec, std::vector<double> &vVec, double *trig, double threshold=0.1,
            double trigFrac=-0.42)
{
    //initial checks
    if(tVec.size() != vVec.size())
    {
        std::cerr << "cfd_sw: Error: supplied vectors not of the same size.\n";
        return false;
    }

    if(tVec.size() == 0)
    {
        std::cerr << "cfd_sw: Error: supplied vectors are of zero size.\n";
        return false;
    }

    if(trigFrac == 0)
    {
        std::cerr << "cfd_sw: Error: supplied trigger fraction cannot be zero.\n";
        return false;
    }

    int slope = trigFrac>0 ? 1 : -1;
    double trigFracAbs = trigFrac>0 ? trigFrac : -trigFrac;

    //find highest peak
    double maxV;
    int maxSample;
    maxV = vVec[0];
    maxSample = -1;
    for(unsigned int iSample=0; iSample<tVec.size(); ++iSample)
    {
        if(slope*maxV < slope*vVec[iSample])
        {
            maxV = vVec[iSample];
            maxSample = iSample;
        }
    }
```

```
    if(maxSample == -1 || slope*maxV < slope*threshold)
    {
        //no peak found
        return false;
    }

    //backwards search from peak to trigger point
    for(int iSample=maxSample-1; iSample>=0; --iSample)
    {
        if(slope*vVec[iSample] < trigFrac*maxV)
        {
            if(INVALIDATE_SECOND_PEAKS)
            {
                //find previous peak; if present, return false
                for(int iSample2=0; iSample2<iSample; ++iSample2)
                {
                    if(slope*vVec[iSample2] > trigFrac*maxV) return false;
                }
            }
            *trig = tVec[iSample] + (trigFracAbs*maxV-vVec[iSample])/(vVec[iSample+1]-vVec[iSample])
                    * (tVec[iSample+1]-tVec[iSample]);
            return true;
        }
    }

    //reached end without trigger
    return false;
}
```

Appendix B

Additional figures and plots

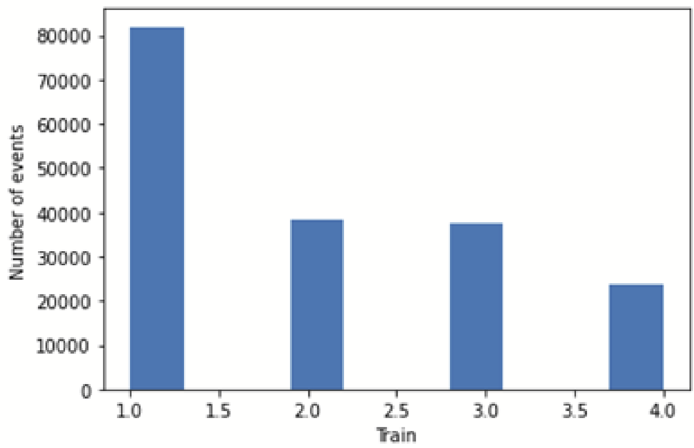

Figure B.1: An example of hit counts in the ToF trains. This is the reason why the trains closest to the beam are manufactured thinner. The limiting factors in how thin they could be made are set by their fragility and the need to cover the entire SiT area.

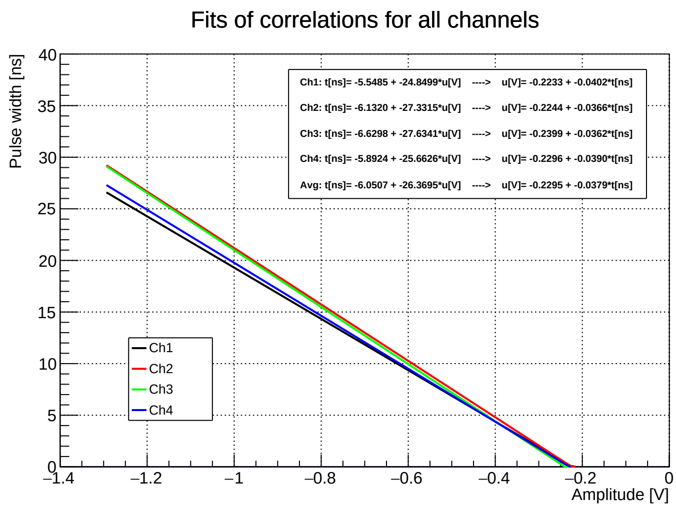

Figure B.2: Fits of correlation plots of pulse amplitude and the CFD pulse length for four individual channels shown in Figure 4.61. The fits are used as one of the inputs to determine the transfer function in Equation 4.4.

Figure B.3: The fine copper mesh used for the shielding experiments plotted in Figure 4.15.

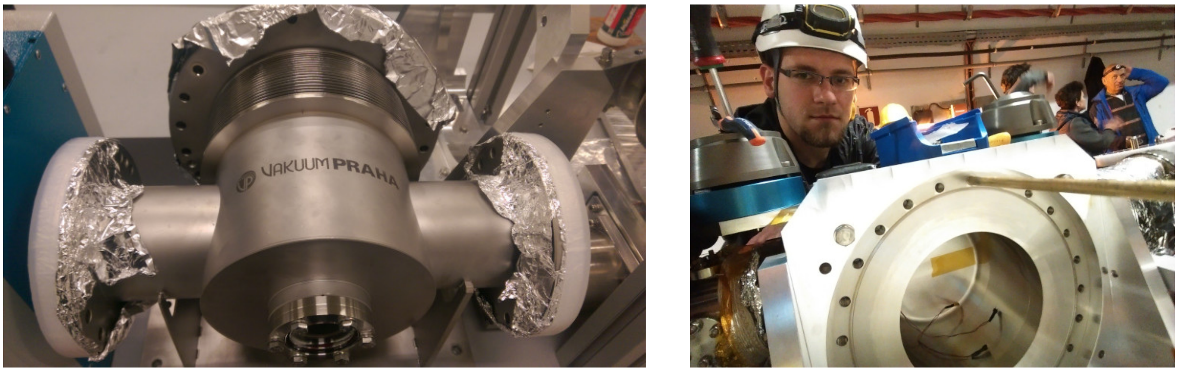

Figure B.4: An extra AFP Roman Pot used in the AFP lab and a look inside the AFP RP as installed at the LHC. One of the insertion guide rods is visible at the top of the Roman Pot in the photo on the right.

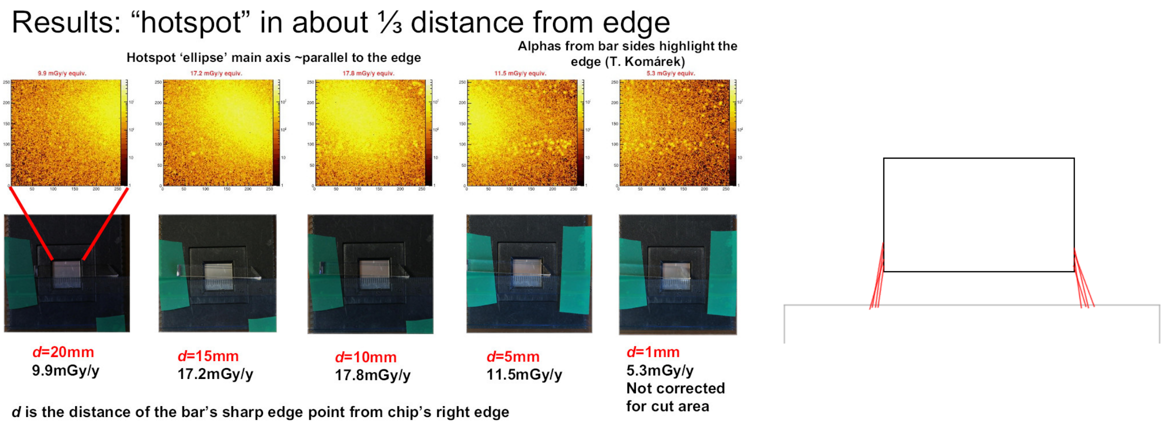

Figure B.5: Radiation emitted by the ToF bars exposed to the conditions inside the AFP Roman Pot for one year, as detected using the particle camera MX-10 featuring a Timepix silicon detector. A clear hot-spot is located where the diffraction pattern lies, even following its orientation. Note the excess of alpha particle hits along the bar edges, a phenomenon that can be explained by the diagram on the right; alphas are highly ionizing and easily stopped, so they are emitted from the surface only. The vertical bar walls offer increased surface area near the detector, resulting in more alpha particles reaching it.